

Serebrennikova Alexandra

# **Biocompatible supercapacitors based on laser induced graphene for wearable applications**

## **MASTER'S THESIS**

to achieve the university degree of  
Diplom-Ingenieurin

Master's degree programme:  
Advanced Materials Science

submitted to

**Graz University of Technology**

### **Supervisor**

Dr. Dott. Francesco Greco

Institute of Solid State Physics



## **AFFIDAVIT**

I declare that I have authored this thesis independently, that I have not used other than the declared sources/resources, and that I have explicitly indicated all material which has been quoted either literally or by content from the sources used. The text document uploaded to TUGRAZonline is identical to the present master's thesis.

---

Date, Signature



# Acknowledgments

I wish to thank my supervisor Dr. Francesco Greco for giving me a chance to work in the LAMPSE group as well as for his help, expert advice and a spark of humor during the period of this research.

I would also like to thank Alexander Dallinger and all other colleagues from the Institute of Solid State Physics at TU Graz, whose competence and support were of a great help for me.

My deepest gratitude goes to my parents, Leonid Serebrennikov and Olga Zhirkova, who instilled in me a love of science, knowledge and courage to try things. I cannot thank enough my grandfather Vladimir Serebrennikov for his help during these studies.

Finally I would like to express a great appreciation and gratitude to Gerolf Heinrichs for his hand, participation and genuine interest in my endeavors. Thank you for all the engrossing discussions and adventures we have had over these years.



# Abstract

In this work a recently found electro-conductive material called laser induced graphene (LIG) [1] obtained by pyrolysis from a polyimide (PI) film was tested as an electrode material for biocompatible flexible supercapacitors (SCs). The fabrication process consisted of pulsed IR-laser scribing on a Kapton<sup>TM</sup> PI foil causing graphene formation under ambient atmosphere conditions. By varying the laser settings (speed, power, pulse resolution) two different morphologies of LIG, porous (LIGP) and fibrous (LIGF), could be obtained. Described technique opens a path to form conductive patterns on flexible PI substrates which is of a high interest in wearable applications. Moreover, after scribing on the stiff PI films the patterns can be transferred to another carrier which allows to achieve better stretchability of the final device. In this thesis medical grade polyurethane (PU) viscoelastic films covered with acrylic adhesive were used for that purpose. Another method of LIG transfer included covering the pre-scribed LIG patterns by the liquid polydimethylsiloxane (PDMS) mixture via spin-coating. Afterwards the PDMS was cured at an elevated temperature until a polymeric PDMS-LIG soft matrix would be formed and could be peeled off from the original PI substrate.

In order to assess whether the described material combinations are suitable to be used as electrode material in supercapacitor devices the microstructure of LIGs on three described carriers was investigated via Scanning Electron Microscopy (SEM) and Light Microscopy (LM). Surface area and porosity are two important properties influencing capacitance of a material, therefore these morphological properties of the LIGP and LIGF materials were characterized via the volumetric gas adsorption measurements performed with classical powder BET analysis of LIG powders as well as via the Gemini<sup>TM</sup> volumetric method performed on polymeric stripes (PI, PDMS) covered with LIG. The latter allowed to assess the pore volume available on the surface of a flat electrode, which is of a high relevance for flat SCs devices where the top layers of the capacitive material can be better accessed by the ionic charges. Mechanical properties, namely the stress to strain curves as well as the resistance *vs.* strain dependencies, were investigated for PDMS and PU covered with LIGs substrates.

Three modifications of supercapacitor devices were designed, fabricated and tested via electrochemical measurements, *i.e.* cyclic voltammetry and constant current charge/ discharge analysis. The first SC type was in a form of Swagelok<sup>TM</sup> cell. Three different substrates, namely PI, PU and PDMS were used as LIG carriers for this device type. The second type of SCs utilized two plane electrodes ( $\approx 40\text{--}100\ \mu\text{m}$  thick) assembled in a flat cell; the third SCs' type was in a form of a roll, where two flat electrodes spaced by a glass fiber separator were rolled together and put into a medical grade cross-linked polyolefine heat shrink tube. Stretchable and biocompatible PU and PDMS were used as LIG carriers. All devices were tested with 1M  $\text{NaNO}_3$  water solution as an electrolyte, flat modification of the cells was also tested with 2M KOH. All devices were prepared with the two modifications of LIGs in order to explore the differences in their capacitive behaviour. It was found that in all cases the LIGP had higher capacitance values as compared to the LIGF. The highest power was achieved in Swagelok<sup>TM</sup> cells with PI substrate serving as the

LIG carrier. In comparison to LIGP, LIGF embedded into PDMS had one order of magnitude lower values of power in Swagelok<sup>TM</sup> cells. LIGP transferred to adhesive PU have shown interestingly promising performance, however for some cells the inner sheet resistance was too high which negatively affected the capacitive properties of respective devices.

The flat cells as well as the rolled cells based on PDMS and PU LIG composites did not show satisfying capacitive behaviour. This fact could be attributed to the high internal sheet resistance for the devices since the electrodes were not pressed to each other and therefore the internal gap between the electrodes was probably too large to allow proper Helmholtz layer to be formed. For the PDMS based LIG electrodes morphological investigations showed that the pore volume accessible for ionic charges is reduced by the polymeric matrix of PDMS itself which could hinder the ability of the ionic charges to penetrate the LIG and to be stored on its surface. In the case of PU substrates we assume the areal load (surface mass density of the transferred material) of LIG material transferred from the PI is not sufficient enough to achieve high surface area of the electrode. Further improvements of the flat cells design are therefore suggested.

The work allowed to obtain a better insight over the electrical and mechanical properties of potentially promising LIG composites applicable for further bio-friendly electronic applications, including wearable (skin-worn) SCs.

# Contents

<b>1</b>	<b>Introduction</b>	<b>1</b>
1.1	Objective . . . . .	1
<b>2</b>	<b>Theoretical Aspects</b>	<b>3</b>
2.1	Materials Section . . . . .	3
2.1.1	Laser Induced Graphene . . . . .	3
2.1.2	Elastic and Viscoelastic Biomaterials . . . . .	7
2.2	Materials Characterization Techniques . . . . .	11
2.2.1	Surface Area and Porosity Characterization . . . . .	11
2.2.2	Quantitative Morphological Characterization of Carbon Thin Films . . . . .	14
2.2.3	Mechanical properties: Strain-stress Analysis . . . . .	16
2.2.4	Electrical Properties . . . . .	17
2.3	Miniature electronic devices of interest . . . . .	18
2.3.1	Strain Sensors . . . . .	18
2.3.2	Supercapacitors . . . . .	19
2.3.3	Elastic Conductive Composites . . . . .	22
<b>3</b>	<b>Experimental</b>	<b>27</b>
3.1	Laser Induced Graphene . . . . .	27
3.1.1	Direct Laser Scribing Carbonization . . . . .	27
3.1.2	Conductive Elastic Biocomposites Based on LIG . . . . .	30
3.2	LIG Materials Characterization . . . . .	32
3.2.1	Imaging Techniques . . . . .	32
3.2.2	Areal mass loading of LIGs . . . . .	32
3.2.3	Thickness Measurements . . . . .	33
3.2.4	Electromechanical Characterization of Composites . . . . .	33
3.2.5	Sheet resistance of LIG Porous and LIG Fibers . . . . .	36
3.2.6	Gas Adsorption Measurements (BET) . . . . .	37
3.2.7	Atomic Force Microscopy (AFM) of LIGs . . . . .	40
3.3	Flexible Supercapacitors based on LIG . . . . .	41

3.3.1	LIG Based Electrodes. Design and Production . . . . .	41
3.3.2	Swagelok <sup>TM</sup> Setup . . . . .	42
3.3.3	Thin stretchable supercapacitor cells . . . . .	44
3.3.4	Rolled flexible supercapacitor cells . . . . .	46
3.3.5	Electrochemical Characterization . . . . .	47
<b>4</b>	<b>Results and Discussion</b>	<b>53</b>
4.1	LIG Materials Characterization . . . . .	53
4.1.1	Morphology of LIG . . . . .	53
4.1.2	Morphology of Conductive Elastic Biocomposites Based on LIG	54
4.1.3	Areal mass loading of LIGs . . . . .	57
4.1.4	Thickness Measurements . . . . .	57
4.1.5	Sheet Resistance of LIG and LIG-PDMS composites . . . . .	58
4.1.6	Electromechanical Characterization of Composites . . . . .	59
4.2	Surface Area and Porosity Characterization . . . . .	64
4.2.1	Gas Adsorption Measurements (BET) for Powder LIGs . . . . .	64
4.2.2	Morphology of LIG via Gemini <sup>TM</sup> Technique and AFM . . . . .	68
4.3	LIG Based Supercapacitors . . . . .	72
4.4	Electrochemical Characterization of Swagelok Supercapacitor Cells . . . . .	72
4.5	Electrochemical Characterization of Flat and Rolled SCs . . . . .	92
4.6	Discussion on Biocompatibility . . . . .	93
<b>5</b>	<b>Summary</b>	<b>95</b>
	<b>Bibliography</b>	<b>97</b>

# List of Figures

2.1	Pyrolytic synthesis of laser-induced graphene (LIG). (i) Structure of polyimide film; (ii) Structural change of polyimide after laser irradiation	3
2.2	(a), Schematic of the synthesis process of LIG from PI. (b), SEM image of LIG patterned into an owl shape; scale bar, 1 mm. The bright contrast corresponds to LIG surrounded by the darker-colored insulating PI substrates. (c), SEM image of the LIG film circled in (b); scale bar, 10 $\mu\text{m}$ . Inset is the corresponding higher magnification SEM image; scale bar, 1 $\mu\text{m}$ . (d), Cross-sectional SEM image of the LIG film on the PI substrate; scale bar, 20 $\mu\text{m}$ . Inset is the SEM image showing the porous morphology of LIG; scale bar, 1 $\mu\text{m}$ . (e), Representative Raman spectrum of a LIG film and the starting PI film. (f), XRD of powdered LIG scraped from the PI film. Picture taken from [1]. . . . .	4
2.3	FTIR spectra of LIG obtained at laser power of 3.6 W and PI films. FTIR spectra of PI showing distinct peaks at 1090-1776 $\text{cm}^{-1}$ , corresponding to the well-defined stretching and bending modes of the C-O, C-N and C=C bonds. After the laser scribing, a broad absorption from 1000 $\text{cm}^{-1}$ to 1700 $\text{cm}^{-1}$ shows that the laser scribing leads to a large variation in the local environment. Picture taken from [1]. . .	5
2.4	Graphene: image of graphene in TEM by Berkeley's TEAM05 [2]. . .	6
2.5	BET specific surface area of LIG-3.6 W from [1] . . . . .	7
2.6	Structural formula of Polydimethylsiloxane (PDMS) [3] . . . . .	7
2.7	TGA curves of PDMS (in $\text{N}_2$ atmosphere, at T rate of 10°/min). Experimental data: solid thick line; simulated: solid thin line [4] . . .	8
2.8	Relative permeability of various penetrants compared to water vapor in PDMS [5] . . . . .	9
2.9	(a) PDMS elastic modulus as a function of the curing cross-linker amount; (b) PDMS network elastic modulus <i>vs.</i> PDMS Base/Curing agent weight ratio $n$ [6]. . . . .	10
2.10	General structure of linear polyurethanes. The urethane groups are marked in blue. $R^1$ stands for the "rest" of the diol used for the synthesis (HO - $R^1$ - OH), $R^2$ stands for the "rest" of the diisocyanate (OCN - $R^1$ - NCO) [7]. . . . .	11
2.11	Different types of physisorption isotherms as observed for different adsorbents. Type I: microporous; Type II: non-porous or macroporous; Type III: non-porous or macroporous with weak interaction; Type IV: mesoporous; Type V: mesoporous with weak interaction; Type VI: layer-by-layer adsorption [8] . . . . .	12

2.12	(Left) Representative schematic profile and morphological parameters of a nanoscaled-C thin film. (Right) 3D AFM view of a sharp step produced in an exemplary sample obtained on a Si substrate; in the inset, a representative topographic AFM map is shown (z scale ranges from -500 to 800 nm). Image taken from [9]	15
2.13	The difference between true stress–strain curve and engineering stress–strain curve [10].	16
2.14	Schematic diagram of a four-point probe circuit [11].	18
2.15	Basic scheme of a common type of strain gauges [12].	19
2.16	Ragone plots for representative energy storage devices of batteries, fuel cells and supercapacitors [13].	20
2.17	Schematic diagram for (A) classical electrostatic capacitor, (B) electric double-layer supercapacitor, (C) pseudocapacitor, and (D) hybrid-capacitor [14].	21
2.18	Process of fabricating a LIG strain sensor embedded in PDMS. Image taken from [15].	22
2.19	Photographs of the strain sensor under (a) twisting and (b) bending; (c) SEM image of carbonized pattern embedded on PDMS [15].	23
2.20	3D scheme of a) the LIG/PDMS supercapacitor assembly, in the inset a digital photograph of the assembled device is reported. Electrical characterization: b) CV at different scan-rates, c) capacitance trend <i>vs.</i> scan rate and d) capacitance retention. The insets in (c) and (d) show the charge discharge profiles at different current and the cycling behavior at $70 \mu A/cm^2$ , respectively. Image taken from [16].	24
2.21	(a) Stress-strain curves up to the break point for the bare PDMS and the PDMS-PI composite. (b) Comparison of the Young’s modulus of the bare PDMS, the PDMS-PI composite, and the Kapton. The reported values were obtained by averaging five different measurements for each type of sample. Image taken from [17].	24
2.22	Two-electrode electrochemical characterization of the SC in 1 M $Na_2SO_4$ . (a) CV performed at several scan rates. (b) CDG performed at several current densities. (c) Cell capacitance and (d) Ragone plot derived from CDG tests. image taken from [17].	25
3.1	LIG formation by laser beam treatment	27

3.2	Map of LIG obtained on Kapton <sup>TM</sup> 50 $\mu\text{m}$ film showing variations upon the laser power within the range between 20% - 40% and speed between 10% - 100%. For laser fluence values $H < (20 \pm 2)J \times \text{cm}^{-2}$ (blue area) no homogeneous LIG formation was found. Flat-LIG was obtained in the range $(20 \pm 2) < H < (45 \pm 5)J \times \text{cm}^{-2}$ and LIG-fibres for $(45 \pm 5) < H < (80 \pm 8)J \times \text{cm}^{-2}$ (green area). The red area, referred to the destroyed polymer sheet, lied in the range $H > (80 \pm 8)J \text{ cm}^{-2}$ [18] . . . . .	28
3.3	Preparation of LIG-PDMS Composite . . . . .	30
3.4	Preparation of LIG-MPU Composite. (i) Laser scribing on polyimide film for LIG creation; (ii-iv) schematics of LIG lamination transfer onto MPU . . . . .	32
3.5	Electromechanical test setup consisting of load cell (A), electrical contacts (B), sample (C) and movable stage (D) [19] . . . . .	34
3.6	Schematics of samples for electromechanical measurements: LIG $\perp$ (LIG scribed lines normal to tensile strain direction) and LIG $\parallel$ (LIG scribed lines parallel to tensile strain direction) . . . . .	35
3.7	The Gemini technique principle for surface area and pore volume determination. Image taken from [20] . . . . .	39
3.8	Light microscope pictures of VIA contact holes and schematics of a LIG based supercapacitor . . . . .	43
3.9	Swagelok <sup>TM</sup> cell setup for cyclic voltammetry experiments . . . . .	44
3.10	LIG-PDMS flexible thin supercapacitor device with composite wiring	45
3.11	LIG-PDMS flexible thin supercapacitor device of a round shape . . .	45
3.12	LIG-MPU flexible thin supercapacitor device of a round shape with Amphenol FCI Clincher Connector . . . . .	46
3.13	LIG-PDMS rolled supercapacitor device with one terminal covered with Al contact . . . . .	46
3.14	Experimental data recorded during a CV test . . . . .	47
3.15	Experimental data recorded during Galvanostatic charge-discharge cycling with potential limitation . . . . .	51
4.1	SEM images of LIG scribed on polyimide . . . . .	53
4.2	SEM image of LIGF layer embedded into PDMS and peeled off from the original PI substrate. The metal tip seen in the picture was used to discharge the surface . . . . .	55

4.3	Schematics of the LIG-MPU samples and SEM images of LIG on PI (top panel) and LIG-MPU (bottom panel): (a) LIGP and (b) LIGF on PI; (c, d) morphology and (e) cross-section of LIGP-MPU; (f, g) morphology and (h) cross-section of LIGF-MPU. All SEM images are top view (sample tilt angle $\Theta = 0^\circ$ ), except for e, h which are tilted views ( $\Theta = 50^\circ$ ) [21] . . . . .	56
4.4	Thickness evaluation of LIGF-PDMS-8:1 composite . . . . .	58
4.5	Tensile test of LIGP  -PDMS . . . . .	60
4.6	Dependencies of resistance and Young's Modulus of LIG-PDMS samples on humidity . . . . .	61
4.7	Tensile test of LIGP  -MPU . . . . .	62
4.8	LIGP-MPU: Normalized resistance, relative humidity, stress at constant strain of 30% . . . . .	63
4.9	LIGF-MPU: Normalized resistance, relative humidity, stress at constant strain of 30% . . . . .	63
4.10	LIGP adsorption/desorption Isotherm . . . . .	64
4.11	Linear BET plot for $p/p^0$ 0.01 to 0.1 for LIGP . . . . .	65
4.12	LIGF adsorption/desorption Isotherm . . . . .	65
4.13	Linear BET plot for $p/p^0$ 0.1 to 0.3 for LIGF . . . . .	66
4.14	Differential pore size distributions for LIGP and LIGF . . . . .	66
4.15	Cumulative Pore volume (a) and Surface area (b) vs. Pore width for LIGP and LIGF(2) . . . . .	67
4.16	Gemini Nitrogen adsorption isotherms of LIGP samples (left) and LIGF samples (right). . . . .	69
4.17	AFM topographical images of LIGF and LIGP on Kapton and on PDMS. . . . .	69
4.18	Morphology at different scales of LIGF and LIGP on Kapton and PDMS . . . . .	70
4.19	Nitrogen adsorption isotherms of LIGF and LIGP on Kapton Film. . . . .	71
4.20	CV diagrams of S0P cells performed at 0 - 0.2 V potential window at different scan rates . . . . .	72
4.21	GCPL diagrams of S0P cells for $V_{max}=0.2$ V at various current densities . . . . .	73
4.22	GCPL diagrams of S0P cells for $V_{max}=0.2$ V at 130 mA/g and 3130 mA/g demonstrating the rise of iR drop with an increase of applied current . . . . .	73

4.23	CV diagrams of S0P cells for larger $\Delta V$ windows at constant scan rate of 5 mV/s . . . . .	74
4.24	CV diagrams of S0P cells for $\Delta V = 0.6$ V at a constant scan rate of 5 mV/s . . . . .	75
4.25	CC diagrams of S0P cells . . . . .	75
4.26	Constant rate CV and constant current GCPL middle range measurements . . . . .	76
4.27	S0P specific gravimetric capacitance of Cell 1 and Cell 2 evaluated at CV voltage window of 0 - 0.2 V for increasing scan rates $dV/dt$ . . . .	77
4.28	Specific Capacitance of LIGP-Kapton electrode evaluated with CV and GCPL data . . . . .	78
4.29	Type S0F, Cell 2. CV and GCPL data in the low voltage range 0 - 0.2 V . . . . .	79
4.30	CC diagrams of Type S0F Cell 2 for $V_{max}=0.2$ V at 250 mA/g and 2000 mA/g demonstrating the rise of the iR drop with an increase of applied current . . . . .	79
4.31	Type S0F, Cell 2. CV and GCPL data in the wider voltage range 0 - 0.5 V . . . . .	80
4.32	Type S0F Electrode - increasing trend in specific capacitance values evaluated from GCPL for increasing charge-discharge current densities at fixed $V_{max} = 0.2$ V . . . . .	81
4.33	Type S0F Electrode - specific capacitance values evaluated from CV data at voltage window of 0 - 0.2 V for increasing scan rates $dV/dt$ (top) and from GCPL data for increasing charge-discharge current densities at fixed $V_{max} = 0.2$ V (bottom) . . . . .	82
4.34	Type S1F Electrodes, Cell 2. CV and GCPL data in the low voltage range 0 - 0.2 V . . . . .	83
4.35	Type S1F Electrodes, Cell 2. Distorted CC curves . . . . .	84
4.36	Type S1F Electrodes, Cell 2. CV and GCPL data in the voltage range 0 - 0.5 V . . . . .	84
4.37	LIGF-PDMS Electrode - specific capacitance values evaluated from CV data at voltage window of 0 - 0.2 V for increasing scan rates $dV/dt$ (top) and from GCPL data for increasing charge-discharge current densities at fixed $V_{max} = 0.2$ V (bottom) . . . . .	85
4.38	CV diagrams of S2P and S2F electrodes in Swagelok cells at various potential windows at a constant scan rate of 2 mV/s . . . . .	86
4.39	CC diagrams of S2P electrodes in a Swagelok cell . . . . .	87

4.40	CC diagrams of S2F electrodes in a Swagelok cell . . . . .	87
4.41	Specific Capacitance of S2P electrode evaluated with CV and GCPL data . . . . .	88
4.42	Specific Capacitance of S2P and S2F electrodes evaluated with GCPL data . . . . .	89
4.43	Comparison of $C_g$ values of LIGF and LIGP based cells . . . . .	91
4.44	Comparison of $C_g$ and $C_A$ trends (obtained from CV data) for cells with varying mass $m$ of an active material when electrode surface area $s$ stays constant . . . . .	91
4.45	Comparison of $C_g$ values and trends obtained from CV and from GCPL data . . . . .	92

# List of Tables

2.1	Caption for LOF . . . . .	9
3.1	Polymeric LIG-sources and LIG Types used in this work. . . . .	29
3.2	Caption for LOF . . . . .	31
3.3	Settings of Electromechanical Stretching Tests . . . . .	35
3.4	List of Samples for Electromechanical Tests . . . . .	36
3.5	Powder BET Measurements Characteristics . . . . .	37
3.6	The List of Samples Prepared for Gemini BET analysis . . . . .	38
3.7	The List of Samples Prepared for AFM analysis . . . . .	40
3.8	The List of LIG Based SC ionic cells based on $NaNO_3$ 1M electrolyte . . . . .	42
3.9	CV and GCPL experiment settings for Swagelok Cells . . . . .	49
4.1	Mass per Surface Area of LIGs on Various Substrates . . . . .	57
4.2	Thickness of LIG-PDMS composites . . . . .	58
4.3	Sheet resistance of LIGF in PDMS depending on the probe and the lasering direction alignment [22] . . . . .	59
4.4	Young's Modulus for LIG-PDMS samples at various %RH . . . . .	60
4.5	Powder BET Measurements Results . . . . .	64
4.6	Morphological properties of LIG samples . . . . .	68
4.7	Summary for Capacitance Values for Swagelok LIG ( $NaNO_3$ , 1M) Cells . . . . .	90



# Abbreviations

AFM	Atomic Force Microscopy
BET analysis	Brunauer–Emmett–Teller analysis
BJH method	Barrett–Joyner–Halenda method
CDG	Galvanostatic Charge and Discharge method
CV	Cyclic Voltammetry
DLWC	Direct Laser Writing Carbonization
EDL	Electric Double Layer
FM	Fixomull
GCPL	Galvanostatic Cycling with Potential Limitation
GF/F	Glass Microfibre Filter
IUPAC	International Union of Pure and Applied Chemistry (IUPAC)
LAMPSe	Laboratory of Applied Materials for Printed and Soft electronics
LIG	Laser Induced Graphene
LIGF	Laser Induced Graphene Fibers
LIGP	Laser Induced Graphene Porous
MPU	Medical Polyurethane
NLDFT	Non-local Density Functional Theory
PDMS	Polydimethylsiloxane

PEEK	Polyether ether ketone
PI	Polyimide
PU	Polyurethane
PVP	Polyvinylpyrrolidone
RH	Relative Humidity [%]
SC	Supercapacitor
STP	Standard conditions for temperature and pressure
TPSA	Total Pore Surface Area
TPV	Total Pore Volume

# 1. Introduction

## 1.1 Objective

The market of smart wearable devices has been significantly growing in the last decade, however its full potential is still limited by the speed of battery development. Therefore, it is particularly important to develop smaller, lighter, and thinner storage devices which would be applicable in miniature electronics. These devices should meet specific criteria, such as having a small size and high efficiency, being flexible, lightweight, and biocompatible. Among the various energy storage arrangements, supercapacitors (SCs) are considered as one of the most promising candidates in wearable electronics. Compared to the batteries, SCs have simpler structure, faster charge–discharge time, higher power density ( $\approx 10$  kW/kg), and longer cycle life ( $>100\,000$  cycles) [23]. Owing to their uncomplicated architecture, their miniaturization has been extensively studied. Among other potentially suitable materials, graphene is considered to be one of the most suitable materials for the role of the electrode/charge carrier in SCs. Graphene is prominent for its excellent conductivity and high surface area: two important components needed for developing efficient SC cells. However, until now the bridge between this material and the industrial applications was hindered by the lack of mass scale production and patterning techniques, compatible with soft and flexible polymer substrates, as required in the foreseen applications.

The objective of this thesis was to investigate a recently found form of graphene called laser induced graphene (LIG) for the role of an electrode material in thin and stretchable SCs. LIG is obtained from commercially available polyimide (PI) films in a photothermal pyrolysis process by laser scanning with an IR laser source. This one step simple process in air is particularly promising for scaling up in industry; it enables the simultaneous formation of LIG and its patterning with custom design.

The work consisted of four main steps which included:

- obtaining LIG from polyimide precursor
- finding the strategies to transfer LIG onto polymeric thin films to form conductive stretchable composites/laminates
- morphological characterization of LIG on various carriers: defining specific surface area and porosity
- electromechanical characterization of the LIG composites/laminates under varying humidity
- designing and fabrication of SC cells and their electrochemical test by the means of cyclic voltammetry and galvanostatic charge-discharge cycling

This work flow defines the structure of the present thesis. At first the reader will be introduced to some theoretical aspects regarding the chosen materials and their

mechanical and morphological characterization. Afterwards a brief overview over the latest achievements in the field of LIG-based devices will be presented. Experimental part will give an in-depth explanation about the steps taken on the way to complete the assigned tasks, which will be followed by the Results and Discussion section rounded by a short Summary section in the end.

## 2. Theoretical Aspects

This chapter gives a compact review of the theoretical aspects and methods used in the presented study. For in-depth explanations references are provided.

### 2.1 Materials Section

#### 2.1.1 Laser Induced Graphene

The effect of direct laser carbonization of the polymeric materials was first reported by Srinivasan *et al.* [24] in 1994, who found that ultraviolet laser irradiation of polyimide PMDA-ODA (Kapton<sup>TM</sup>) yields a patternable, porous, electrically conducting carbon network. Later in 2014 Tour's group has found similar effect for the polyimide (PI) Kapton<sup>TM</sup> surfaces treated by CO<sub>2</sub> laser sources emitting in IR spectrum [1]. The proposed chemical process is schematically shown in Figure 2.1.

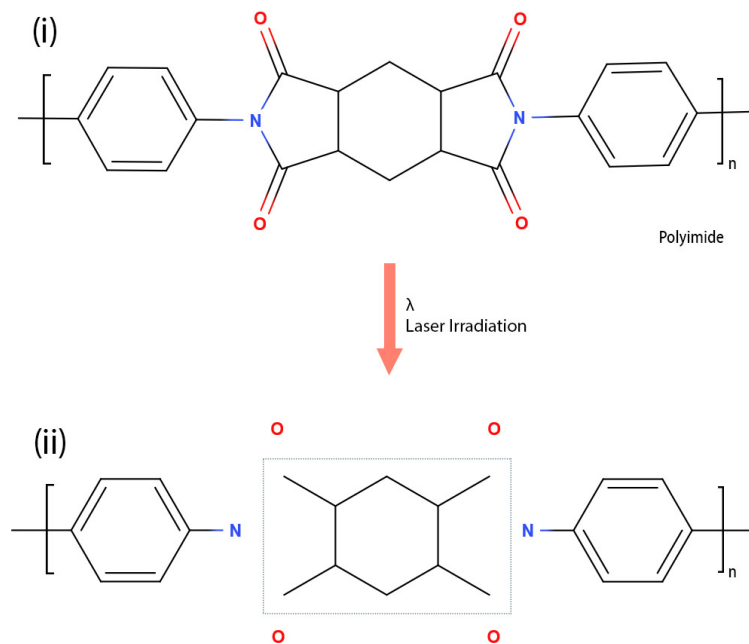


**Figure 2.1:** Pyrolytic synthesis of laser-induced graphene (LIG). (i) Structure of polyimide film; (ii) Structural change of polyimide after laser irradiation

Figure 2.2 sums up the procedure leading to LIG formation by irradiating a commercial PI film with a CO<sub>2</sub> infrared laser under ambient conditions.

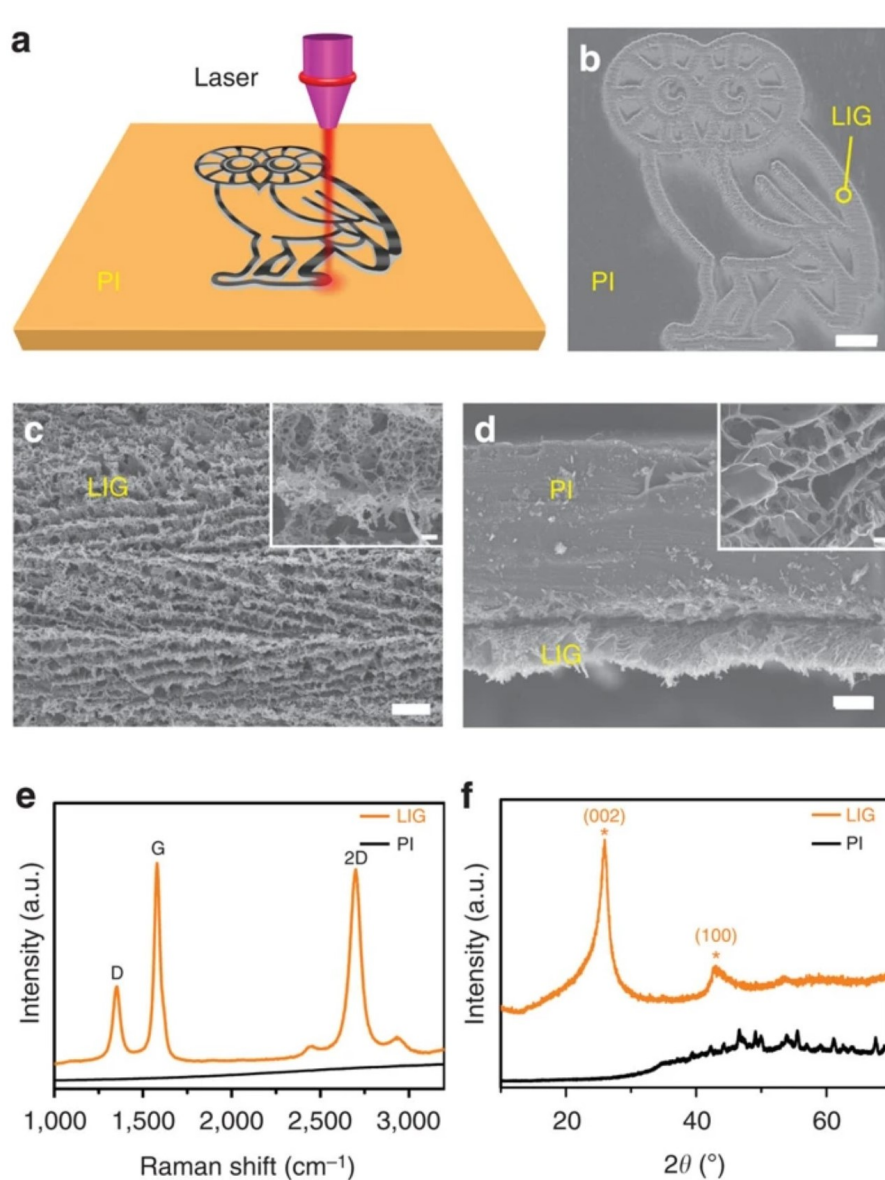


**Figure 2.2:** (a), Schematic of the synthesis process of LIG from PI. (b), SEM image of LIG patterned into an owl shape; scale bar, 1 mm. The bright contrast corresponds to LIG surrounded by the darker-colored insulating PI substrates. (c), SEM image of the LIG film circled in (b); scale bar, 10  $\mu\text{m}$ . Inset is the corresponding higher magnification SEM image; scale bar, 1  $\mu\text{m}$ . (d), Cross-sectional SEM image of the LIG film on the PI substrate; scale bar, 20  $\mu\text{m}$ . Inset is the SEM image showing the porous morphology of LIG; scale bar, 1  $\mu\text{m}$ . (e), Representative Raman spectrum of a LIG film and the starting PI film. (f), XRD of powdered LIG scraped from the PI film. Picture taken from [1].

Changes in chemical structure of initial polyimide substrate have shown formation of the graphitic structures on the final product of laser pyrolysis which was demonstrated by characteristic Raman spectrum showing D and G lines for the final product as in Figure 2.2(e). Figure 2.3 shows characteristic change of FTIR

spectra of PI as compared to the obtained LIG.

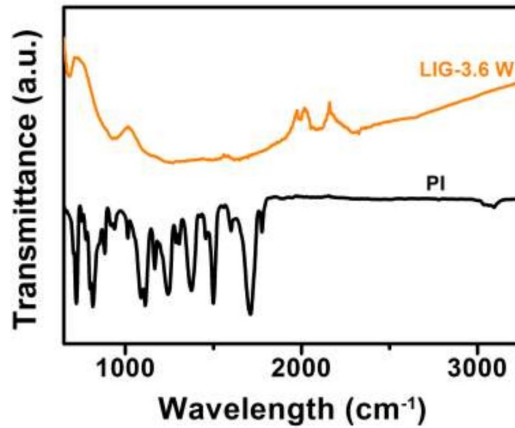


**Figure 2.3:** FTIR spectra of LIG obtained at laser power of 3.6 W and PI films. FTIR spectra of PI showing distinct peaks at  $1090\text{-}1776\text{ cm}^{-1}$ , corresponding to the well-defined stretching and bending modes of the C-O, C-N and C=C bonds. After the laser scribing, a broad absorption from  $1000\text{ cm}^{-1}$  to  $1700\text{ cm}^{-1}$  shows that the laser scribing leads to a large variation in the local environment. Picture taken from [1].

### Formation and Morphology of LIG

Short laser pulses enable a rapid heating of a precursor which causes laser induced pyrolysis taking place at temperatures over  $900^{\circ}\text{C}$ . The material prepared by the laser treatment of the polyimide films was shown to consist of graphene and is nowadays referenced as laser induced graphene, *i.e.* LIG [1].

On the atomic level LIG has a graphene structure of flat hexagonal carbon rings organized in honeycomb crystal lattice as can be seen in Figure 2.4 [2]. Single graphene sheets are further stacked into 3D structures in graphite [25].

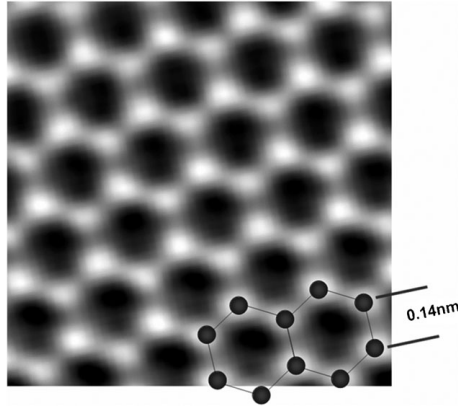


**Figure 2.4:** Graphene: image of graphene in TEM by Berkeley’s TEAM05 [2].

For the microstructure of LIG it was found that laser settings can drastically affect the final morphology. Tour *et al.* investigations of LIG formation concluded that the minimum threshold for polyimide precursors to be transformed into conductive carbonaceous material lays at the laser fluence  $H \approx 5 J \cdot cm^{-2}$ . The resulting LIG material has porous microstructure, predominantly consisting of flat flocculent particles, hence its notation as flat or porous LIG. Further increase in laser power, *i.e.*  $H$  up to  $> 40 J \cdot cm^{-2}$ , leads to LIG-fibers which shows fibrous morphology constituted by ultrathin carbonaceous fibers [26].

### Electrical Properties of LIG

Among other physical properties of LIG, one of the main interest in this thesis is its electrical resistance  $R$ . Typically for compact organized materials (*i.e.* without voids in bulk) the main two factors defining their electron conductivity are attributed to the lattice structure and crystalline defects present in bulk [27]. However it was shown that for graphene and graphite fragments organized into porous 3D structures, the conductive behavior is drastically affected by mechanical particle arrangement mechanisms as they play a major role in defining particle contact area in the bulk [28]. In general it was found that LIG materials have high electrical conductivity (5-25 S/cm) [29].

One of the latest studies conducted at the Laboratory of Applied Materials for Printed and Soft (LAMPSe) in TU Graz has shown that the electrical properties of LIG are directly dependent on its morphology, namely that the flat LIG has lower electrical conductivity than the LIG-fiber, as according to the results of Bachelor Thesis of David Grafinger [22].

### LIG Porosity and Surface Area

To date the literature provides a few studies regarding the LIG porosity and its surface area. Most of the papers refer to the results of Lin *et al.* 2014 [1]. In this study the LIG was obtained from Kapton PI precursor (Cat. No. 2271K3, thickness: 0.005 inch) at laser power of 3.6 W. By means of Brunauer–Emmett–Teller analysis

(BET, described in Section 2) the specific surface area of the LIG was determined to be  $\sim 342\text{m}^2/\text{g}$ . It was shown that this LIG was a mesoporous material with the pore sizes distributed at 2.36 nm, 3.68 nm, 5.37 nm and 8.94 nm. In Figure 2.5 the differential pore volume distribution graph can be seen.

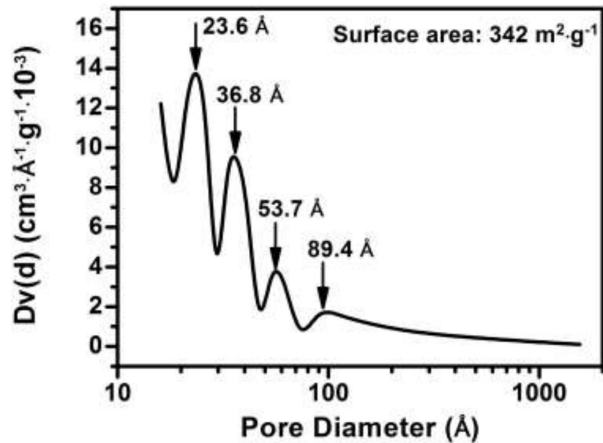


**Figure 2.5:** BET specific surface area of LIG-3.6 W from [1]

## 2.1.2 Elastic and Viscoelastic Biomaterials

By IUPAC recommendations from 2012 the term biomaterial is defined as *a material exploited in contact with living tissues, organisms, or microorganisms* [30].

Within a big variety of biomaterials, two were used in this work and therefore their short introduction is presented in this subchapter.

**Polydimethylsiloxane (PDMS)** is a biocompatible [31] structurally isotropic polymeric material with an empirical formula  $\text{CH}_3[\text{Si}(\text{CH}_3)_2\text{O}]_n\text{Si}(\text{CH}_3)_3$ , where n is the number of monomers repetitions.

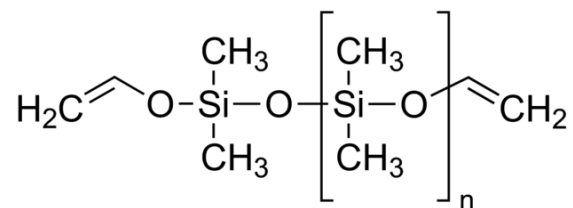


**Figure 2.6:** Structural formula of Polydimethylsiloxane (PDMS) [3]

A typical value of n is between 90 and 140 which leads to a molecular weight ranging from 6800 to 30000 g/mol. Depending on the length of the chain, the non-cross-linked PDMS may exhibit almost liquid (low n) or semi-solid (high n) properties. The siloxane bonds Si-C result in a flexible polymer chain with a high level of

viscoelasticity. Further cross-linking of the chains into 3D network may be performed via addition or condensation mechanisms which lead to a hydrophobic elastomer [32]. The final material is dielectric which is chemically inert, thermally stable, permeable to gases [33], transparent at optical frequencies (240 - 1100 nm) and exhibits isotropic and homogeneous mechanical properties [6].

As compared to other polymers, thermal degradation process of cross-linked PDMS begins at relatively high temperatures around 350°C as can be seen from thermogravimetric analysis (TGA) in Figure 2.7 [4].

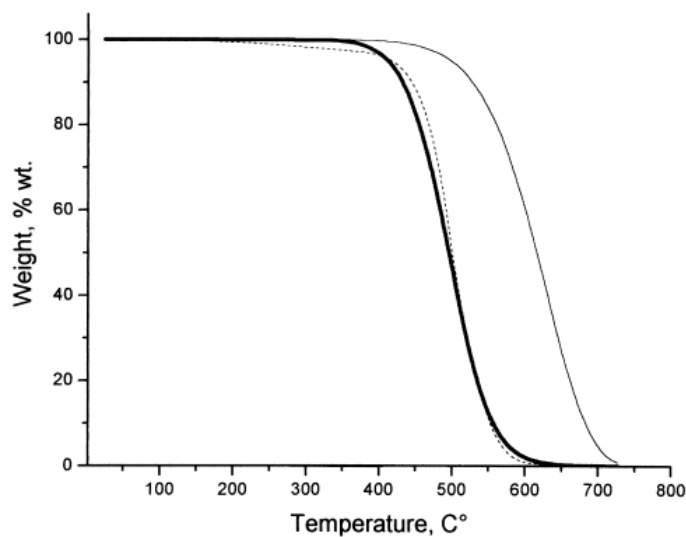


**Figure 2.7:** TGA curves of PDMS (in N<sub>2</sub> atmosphere, at T rate of 10°/min). Experimental data: solid thick line; simulated: solid thin line [4]

As mentioned before PDMS shows high gas permeability for most of the common gas species including water vapor [33] as shown in Figure 2.8 from [5].

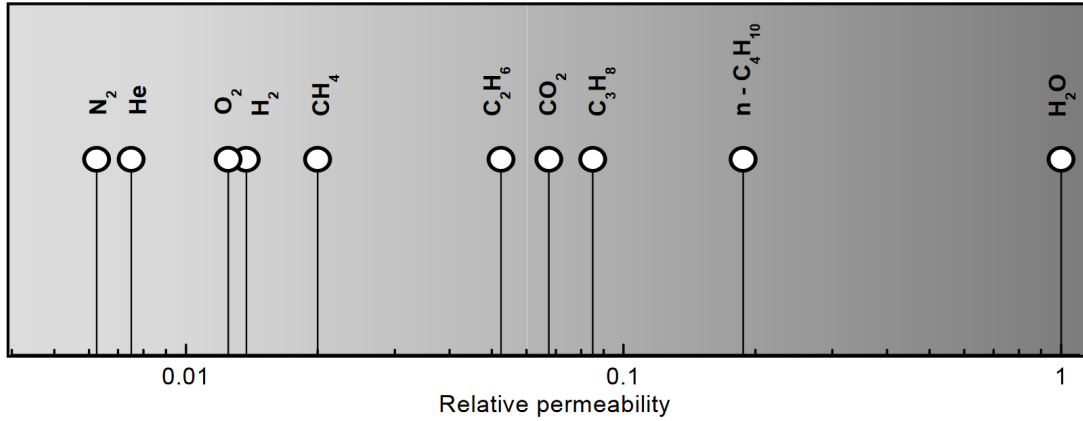


**Figure 2.8:** Relative permeability of various penetrants compared to water vapor in PDMS [5]

In absolute numbers water vapor permeation through PDMS reaches remarkably high value of 40000 *Barrer* ( $1.34 \cdot 10^{-11} \frac{\text{mol} \cdot \text{m}}{\text{m}^2 \cdot \text{s} \cdot \text{Pa}}$ ). That fact is dictated by a small size of penetrant  $H_2O$  molecules possessing low values of solubility and diffusivity even in a highly hydrophobic PDMS polymeric matrix [5]. The permeation properties of selected gas species are listed in Table 2.1.

**Table 2.1:** Permeability Coefficients [*Barrer*]<sup>1</sup> for the PDMS [33], [5]

$N_2$	$H_2$	$O_2$	$CH_4$	$CO_2$	$H_2O$
$400 \pm 10$	$890 \pm 30$	$800 \pm 20$	$1200 \pm 40$	$3800 \pm 70$	$40000 \pm 800$

$$^1 1 \text{ Barrer} = 3.35 \times 10^{-16} \frac{\text{mol} \times \text{m}}{\text{m}^2 \times \text{s} \times \text{Pa}}$$

PDMS mechanical strength and Young's Modulus  $E$  are dependant on cross-linking density [6]. Zhixin Wang *et al.* investigated this dependence for PDMS networks prepared from two component mixtures from Sylgard<sup>TM</sup> 184 silicone elastomer base and Sylgard<sup>TM</sup> 184 silicone elastomer curing agent manufactured by Dow Corning (Mid-land, MI). The amount of curing agent used lays in direct correlation with the degree of cross-linking in the final elastomer. Greater cross-linking density leads to the higher stiffness of PDMS as can be seen from Figure 2.9.

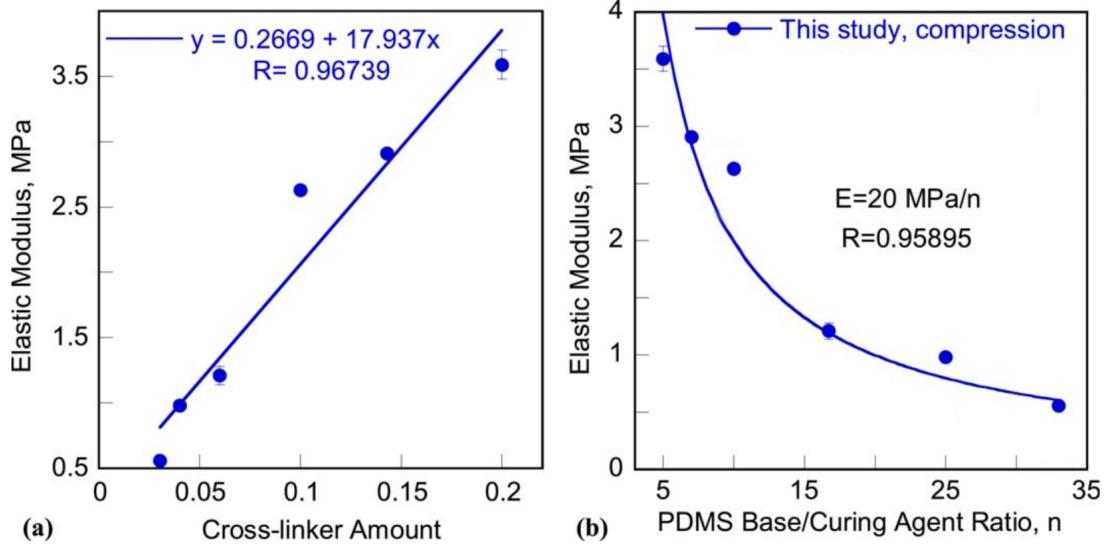


**Figure 2.9:** (a) PDMS elastic modulus as a function of the curing cross-linker amount; (b) PDMS network elastic modulus *vs.* PDMS Base/Curing agent weight ratio  $n$  [6].

Elastic Modulus  $E$  varies in the range of 0.5 - 3.5 MPa and can be in general approximated by an expression:

$$E = \frac{20}{n} \text{ mPa} \quad (2.1)$$

Where  $n$  is the weight ratio of PDMS base to curing agent.

Described properties make PDMS highly attractive for the fabrication of composite microstructures with implementation in biomedical systems [34], wearable applications and the internet of things. In these applications PDMS can play a role of a mechanically and chemically stable substrate or a sealed capsule carrying an electrical device.

### Polyurethane Medical Films

Polyurethanes (PUs) are known to be extremely biocompatible materials [35]. Chemical structure of repeating unit of PU derives from three complex monomers: an isocyanate with two or more functional ends, a polyol, and a chain extender, variations of which lead to a number of different PU materials that can be synthesized [36]. Both thermosetting and thermoplastic polyurethanes are nowadays available.

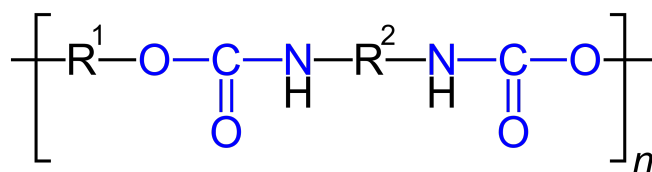


**Figure 2.10:** General structure of linear polyurethanes. The urethane groups are marked in blue.  $R^1$  stands for the “rest” of the diol used for the synthesis ( $\text{HO} - R^1 - \text{OH}$ ),  $R^2$  stands for the “rest” of the diisocyanate ( $\text{OCN} - R^1 - \text{NCO}$ ) [7].

Polyurethanes can be produced in a form of thin  $\approx 20\text{-}40 \mu\text{m}$  highly viscoelastic transparent films [37], which due to their high water vapor permeability and biocompatibility properties are widely used in medical applications on skin (e.g. patches). As it will be seen in the following chapters these properties of PU can be utilised for packaging when preparing flexible electrical devices such as thin supercapacitor cells.

## 2.2 Materials Characterization Techniques

### 2.2.1 Surface Area and Porosity Characterization

Surface area and porosity are two important physical properties that have a direct impact on the physical and chemical properties of materials. For a material used for electrochemical applications differences in the surface area and bulk pore size distribution can greatly influence its characteristics, such as *e.g.* capacitance and power performance. These characteristics play the major role in electrochemical and other heterogeneous reactions taking place on the interfaces.

Before describing the gas adsorption analysis techniques the term porosity and the nomenclature associated with it shall be defined. The International Union of Pure and Applied Chemistry (IUPAC) defines porosity as “*A concept related to texture, referring to the pore space in a material.*” [38]. Additionally the pore size definitions are introduced for those of three types: *the micropore* width is defined as not to exceed about 2 nm, the *mesopore* width to be in the range 2–50 nm and the *macropore* width to be above about 50 nm [39].

Gas Adsorption Analysis is the technique which is commonly used for surface area and porosity determinations. It involves exposing solid materials to gases at a variety of conditions and evaluating either the weight or the volume uptake by the solid sample. The latter is further referred to as the “adsorbent”. These data allow to obtain information about the physical characteristics of the adsorbent, including: surface area  $A$ , skeletal density ( $\mu_s$ ) - density of the material that constitute the particle, porosity, total pore volume (TPV), and pore size distribution.

Before the determination of an adsorption isotherm all of the physisorbed contaminants have to be removed from the surface of the adsorbent. At the same time the irreversible chemical as well as physical changes of the surface or the bulk structure should be avoided. This may be achieved by degassing, i.e., exposure of the surface to a high vacuum or an atmosphere of an inert gas. For non-microporous materials flushing the adsorbent with an inert gas (which may be the adsorptive) at elevated temperature is another technique which is often adopted.

### BET Surface Area Calculation

Adsorption isotherms can be of different shapes and contain information about specific adsorption processes which take place on the investigated surfaces. The IUPAC classifies 6 types of the isotherms which are shown in Figure 2.11.

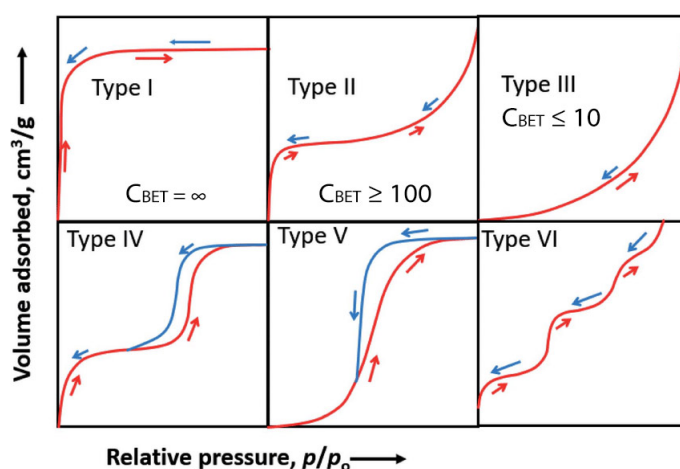


**Figure 2.11:** Different types of physisorption isotherms as observed for different adsorbents. Type I: microporous; Type II: non-porous or macroporous; Type III: non-porous or macroporous with weak interaction; Type IV: mesoporous; Type V: mesoporous with weak interaction; Type VI: layer-by-layer adsorption [8]

The Brunauer, Emmett and Teller (BET) technique invented in 1938 is the most common method for determining the surface area of powder and porous materials. Nitrogen gas is usually used as the probe as it shows almost no chemisorption; the adsorbent under investigation is exposed to liquid nitrogen at low temperature conditions (*i.e.* 77 K). The temperature of the solid sample is kept constant, or under isothermal conditions, while the pressure or concentration of the adsorbing gas is increased until it reaches a final pressure  $p^0$ . That allows to obtain information about gas adsorption as a function of pressure in a form of an isotherm graph, where the x-axis is the relative pressure of the gas and the y-axis is its volume adsorbed onto the sample. At first a BET plot is constructed for the relative pressure range  $0.05 \leq p/p^0 \leq 0.3$  for the mono-layer capacity  $n_m$ , which is the volume of gas adsorbed at standard temperature and pressure (STP: 273 K and 1 atm), to be derived. The specific surface area  $A_{BET}$  [ $g/m^2$ ] of the material is evaluated from the measured mono-layer adsorption capacity  $n_m$  and knowledge of the cross-sectional area of the molecule being used as a probe,  $\sigma$ . The cross-sectional area of  $N_2$  is

taken as  $\sigma = 16.2 \text{ \AA}^2/\text{molecule}$  [8]. At each stage a certain level of assumptions is introduced into the evaluation procedure and thus it requires careful consideration for each investigated system.

The BET equation is conveniently expressed in the linear form with  $p/p^0$  being partial pressure,  $n$  specific volume of the gas adsorbed,  $C$  an additional parameter limiting the number of layers on the surface [40], and  $C_{BET}$  - BET constant dependent on the isotherm shape:

$$\frac{p/p^0}{n(1-p/p^0)} = \frac{1}{n_m C} + \frac{C_{BET} - 1}{n_m C_{BET}} \frac{p}{p^0} \quad (2.2)$$

Thus, the BET plot of  $\frac{p/p^0}{n(1-p/p^0)}$  versus  $p/p^0$  should be a straight line with slope  $s = \frac{C_{BET}-1}{n_m C_{BET}}$  and intercept  $i = \frac{1}{n_m C}$ . By solving these two simultaneous equations, one obtains:

$$n_m = \frac{1}{s + i} \quad (2.3)$$

and

$$C_{BET} = \frac{s}{i} + 1 \quad (2.4)$$

The linear part of the isotherm is usually in the range  $p/p^0$  0.05 – 0.30 where the best linear fit is obtained by statistical analysis. Finally having  $n_m$ ,  $N_A$  - Avogadro Number and  $m$  - adsorbent mass, the BET-area from the mono-layer capacity can be calculated as:

$$A_{BET} = \frac{n_m \cdot N_A \cdot \sigma}{m} \quad (2.5)$$

According to the Equation 2.2 the values of  $C_{BET}$  and  $p/p^0$  for a given  $n_m$  is in a reciprocal dependency:

$$\left(\frac{p}{p^0}\right)_{n_m} = \frac{1}{\sqrt{C_{BET} + 1}} \quad (2.6)$$

Which shows that high  $C_{BET}$  values ( $> 350$ ) correspond to the low partial pressures and therefore to the high adsorption energy of the first layer and *vice versa* when the adsorption energy and  $C_{BET}$  values are low ( $< 20$ ) the partial pressures are high. This might lead to an ill defined inflection point [41] as can be seen from the exemplary isotherms in Figure 2.11. Type I and II of isotherms correspond to microporous solids and non-porous/macroporous, respectively; the isotherm of Type III occurs for materials with high level of interactions between adsorbate and adsorbent. Another problem might arise from relatively weak adsorbent-adsorbate interactions together with comparatively strong adsorbate-adsorbate interactions, which is the case of the adsorption of water vapor on carbon materials. For such systems, the BET mono-layer capacity is not reliable and does not provide a realistic

assessment of total surface area magnitude if the surface was not properly prepared, *i.e.* degassed and reduced in case of graphene oxide. However, it may provide a useful indication of the extent of the 'hydrophilic' area or the extent of the high-energy sites [42].

### Porosity Calculations

The Barrett, Joyner, Halenda method (BJH) is commonly used for assessing the pore size distribution of mesoporous solids (*i.e.* adsorbents having effective pore widths in the approximate range of 2-50 nm) and small macroporous materials (*i.e.* with size range of 50-70 nm) . The model is based on the capillary condensation assumption in the  $p/p^0$  region of  $0.3 \pm 1$  and utilizes the Kelvin model of pore filling. The modified Kelvin equation [41] relates the amount of adsorbate removed from the cylindrical pores of the material, as the relative pressure  $p/p^0$  is decreased from a high to low value, to the size of the pores 2.7.

$$\ln\left(\frac{p}{p^0}\right) = \frac{2\gamma V_m}{RT(r_p - t_c)} \quad (2.7)$$

Where:  $V_m$  - liquid molar volume,  $\gamma$  - surface tension of liquid nitrogen,  $r_p$  - pore radius and  $t_c$  - statistical thickness of the adsorbed multilayer film, which is formed prior to pore condensation. The function of  $t_c$  is given by an empirical function, one of which is called after Harkins and Jura and often used in BJH method. An in-depth description of this approach can be found in Chapter 7 in Rouquerol *et al.*[43].

For the micropores size distributions (*i.e.* pores sizes  $\leq 2$  nm) other theories are applied, among which the Non-local density functional theory (NLDFT) is one commonly used [44].

## 2.2.2 Quantitative Morphological Characterization of Carbon Thin Films

Although classical BET analysis is widely used and provides satisfactory results, it also has certain disadvantages, one of which is the demand for rather large amount of material for the typical experimental adsorption chambers. Another drawback of those chambers is the impossibility of studying the surface properties without distorting the original geometric configuration in which the material was obtained. This becomes especially important when working with films and other materials having a 2D shape.

Just recently Francesca Borghi *et al.* from University of Milan have invented a method for quantitative characterization of the interfacial morphology and bulk porosity of nanoporous cluster-assembled carbon thin films [9]. In their work the authors utilize atomic force microscopy (AFM) and volumetric nitrogen adsorption technique for investigating the specific surface area, roughness and porosity of nanoporous carbon films.

### Morphological characterization

The principle set-up of the AFM analysis of graphene films is explained in the following Figure 2.12.

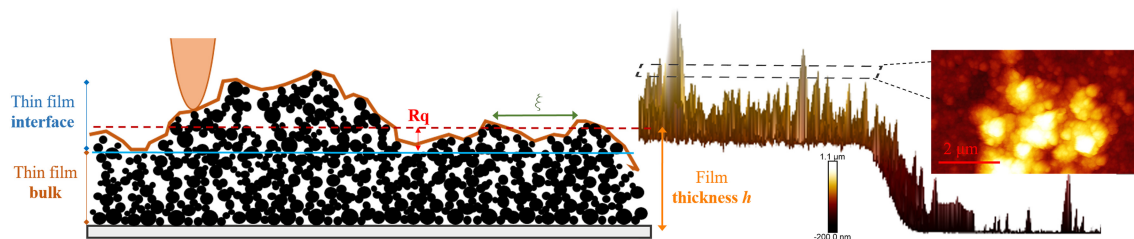


**Figure 2.12:** (Left) Representative schematic profile and morphological parameters of a nanoscaled-C thin film. (Right) 3D AFM view of a sharp step produced in an exemplary sample obtained on a Si substrate; in the inset, a representative topographic AFM map is shown (z scale ranges from -500 to 800 nm). Image taken from [9]

The images obtained by AFM were flattened by special mathematical technique, which allows to evaluate the morphological properties such as root-mean-square surface roughness  $R_q$  (calculated as standard deviation of surface heights); the interfacial specific area  $A_{spec}$  (calculated as the ratio of three-dimensional surface area scanned by AFM tip to the projected area); the correlation length  $\xi$  representing the estimation of the halved lateral dimension of the biggest morphological features on the top of the surface. The latter can be equally seen as the aperture of the largest surface pores (see Figure 2.12). One of the most important characteristics, namely the film thickness  $h$ , was calculated as the mean distance between the film surface and the substrate.

As mentioned earlier 2D shaped porous materials obtained on the surfaces can show different surface area values *in situ* as compared to the bulk properties when investigated in the powder form. This fact can in turn drastically affect the effective surface area available for *e.g.* heterogeneous reactions. The authors distinguish the top area by calling it thin film interface in order to highlight its possible morphological difference as compared to the thin film bulk which lays underneath. This approach becomes especially interesting when investigating the processes taking place on the top surface of the porous films as it allows to define the peculiarities of the interfacial area.

## Gas adsorption measurements

For the gas adsorption measurements the samples of the thin carbon films obtained on silicone stripes 5 x 70 mm were at first degassed in helium atmosphere. The temperature dependence of degassing processes was carefully investigated and the best suitable conditions were found. Afterwards, the authors used a miniature experimental Gemini<sup>TM</sup> set-up which allowed to measure the bulk porosity of the thin carbon film samples without scribing the material from the surface. The advantage of this method lays in the fact it does not require large amounts of materials and

the material itself can be put into a miniature gas tube chamber in the form it was prepared. Obtained isotherms allowed to calculate the surface area and pores size distribution characteristics by applying BET and BJH methods respectively. In the described case of measurements the obtained  $A_{BET}$  value represented the total surface area of both the thin film interface and bulk matrix, and was only limited by the diffusion and adsorption of nitrogen inside the carbon porous matrix on the surface of the substrate.

### 2.2.3 Mechanical properties: Strain-stress Analysis

For materials characterization their electrical and mechanical behavior needs to be quantified.

In regard to the **mechanical properties** typically a stress-strain curve, obtained in tensile, compression or shear experiments, is used. It shows the relation between a stress  $\sigma$  [Pa] applied on a test coupon and a relative deformation caused by it.

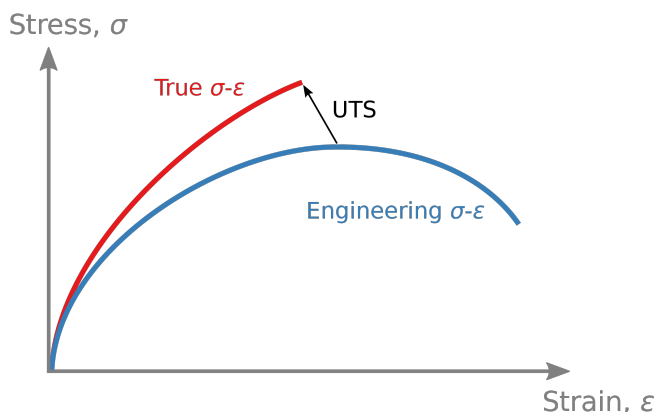


**Figure 2.13:** The difference between true stress-strain curve and engineering stress-strain curve [10].

In many cases the deformation is appointed to elongation of a specimen and in general is called strain  $\epsilon$  [a.u]:

$$\epsilon_t = \int \delta L/L \tag{2.8}$$

Index  $t$  denotes the true elongation calculated for each further  $\delta L$  in comparison to the developed elongation  $L$  at each moment of time during the experiment. In contrast engineering strain is calculated as:

$$\epsilon = L/L_0 \tag{2.9}$$

Where  $L_0$  is the length of the specimen in the beginning. Engineering stress is therefore defined as:

$$\sigma = F/A_0 \quad (2.10)$$

Where  $F$  is the force applied,  $A_0$  - specimen's cross section area at the beginning of the experiment. If the changes in the cross-section area are taken into account, then the stress curve is called *true stress*:

$$\sigma_t = F/A_t \quad (2.11)$$

Equation connecting the engineering strain  $\epsilon$  to the true strain  $\epsilon_t$  is given by the formula:

$$\epsilon_t = \ln(L/L_0) = \ln(1 + \epsilon) \quad (2.12)$$

The graph of stress to strain allows to estimate yield strength, ultimate tensile strength (UTC), toughness as well as Young's modulus. The latter is calculated as a slope of a linear part of the curve, where the behavior is considered to be elastic:

$$E = \sigma/\epsilon \quad (2.13)$$

When undergoing deformation soft materials often exhibit viscoelastic properties showing time-dependent strain. Whereas elasticity is accounted to the stretching of bonds in an ordered solid, viscosity in turn is a consequence of the molecules aligning along the force vector and of the diffusion of atoms in an amorphous material [45].

## 2.2.4 Electrical Properties

One of the important characteristics of a material is its electrical conductivity  $\sigma$  or its inverse value - electrical resistivity  $\rho$ . For thin films it is common to calculate these parameters by measuring sheet resistance  $R_s$  [ $\Omega/sq$ ] of a flat sample of a known thickness  $\theta$  by a four-probe method:

$$\sigma = \frac{1}{\rho} = \frac{1}{R_s \times \theta} \quad (2.14)$$

A four-probe method makes use of a four equally-spaced, co-linear probes which are brought in an electrical contact with the material. The main advantage of this method is the elimination of contact and wire resistance *i.e* inner resistance components of the measurement setup from the final result. A diagram of the measurement setup is shown in Figure 2.14 below.

During the measurement a DC current  $I$  is applied between the outer probes, whereas a voltage drop  $\Delta V$  is measured between the inner two probes.

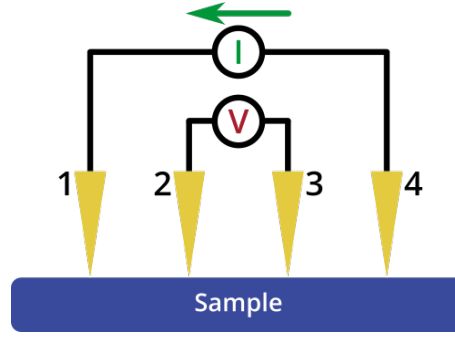


**Figure 2.14:** Schematic diagram of a four-point probe circuit [11].

Following equation is used to calculate  $R_s$ :

$$R_s = \frac{\pi}{\ln(2)} \frac{\Delta V}{I} \quad (2.15)$$

The geometric correction factor  $\frac{\pi}{\ln(2)}$  is required to take the shape of the sample, as well as the positioning of the probes into account. The most accurate results are obtained for probing the center of the sample [11]. Equation 2.15 only applies when the sample's size significantly larger, 40 and more times greater, than the spacing of the probes. The thickness  $\theta$  has to be less than 40% of the probe spacing. Smaller sample dimensions might limit the current paths between the probes which results in a overestimated values of  $R_s$ . In this case, an additional correction factor  $C_f$  accounting for the specified geometry of the sample is introduced [46], [47]:

$$R_s = \frac{\pi}{\ln(2)} \frac{\Delta V}{I} C_f \quad (2.16)$$

## 2.3 Miniature electronic devices of interest

In this work we tried to find the ways to implement LIG material into miniature electronic devices. Therefore here we at first give a short insight of the two types of such systems: strain sensors and supercapacitors.

### 2.3.1 Strain Sensors

Strain gauges are electrical conductor devices that are used to measure strain-resistance dependencies which can be further used for calculation stress. A typical schematics of a gauge is shown in Figure 2.15 [48].

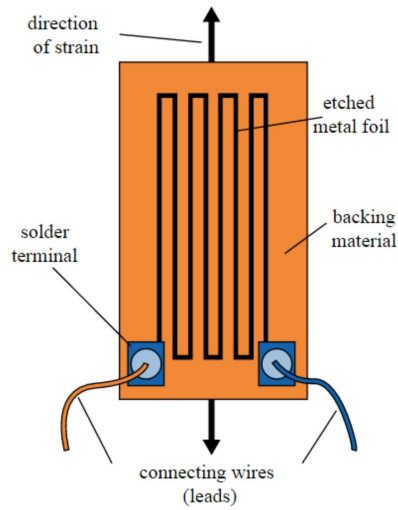


**Figure 2.15:** Basic scheme of a common type of strain gauges [12].

The working principle is based on a change in electrical resistance  $\Delta R$  of a device upon its deformation.  $\Delta R$ . The gauge factor (GF) or strain factor is defined as the ratio of relative change in electrical resistance  $\Delta R/R$  to the engineering strain  $\epsilon$ :

$$R_s = \frac{\Delta R/R}{\epsilon} \quad (2.17)$$

### 2.3.2 Supercapacitors

Batteries, electrochemical supercapacitors (ESs), also sometimes called ultra-capacitors, electrolytic capacitors and fuel cells belong to the group of the most important electrochemical energy storage/conversion devices. Figure 2.16 demonstrates the relationship between power density  $P/m$  and energy density  $E$ , two important properties characterizing a storage device performance. As it can be seen from the Ragone plot, on the ladder of the power density values supercapacitors take the middle position between electrolytic capacitors and batteries, trading off however with relatively low values of energy density.

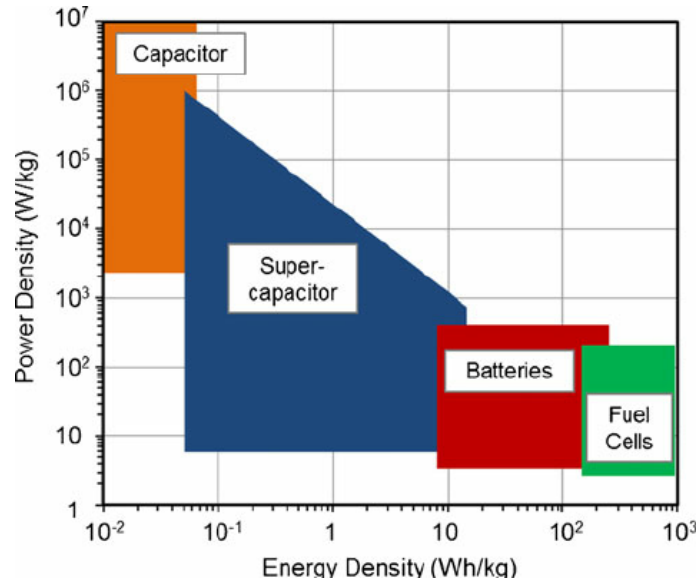


**Figure 2.16:** Ragone plots for representative energy storage devices of batteries, fuel cells and supercapacitors [13].

The ability of supercapacitor to deliver energy in a very short time makes them interesting in a wide variety of applications such as electric or hybrid electric vehicles, portable/wearable electronics, smart grids etc. However, low values of energy density  $E$  put a challenge for adapting ESs technologies for the industry. Therefore an extensive work is nowadays put into increasing the storage capability of the electrode materials used for ESs. Energy density is defined as:

$$E = \frac{1}{2}CV^2 \quad (2.18)$$

Where  $C$  - capacitance and  $V$  - voltage applied. As the equation 2.18 shows, either broadening a possible potential window of the electrolyte (electrolyte salt + solvent) at which the ESs devices can be used or increasing the intrinsic capacitance of the materials used to store the charge are the two ways of solving the problem.

The fundamental mechanisms of the charge storage in supercapacitors can be found in the book of Aiping Yu *et. al* [49]. Here we will give a short introduction of the three classes of ESs devices as demonstrated in Figure 2.17:

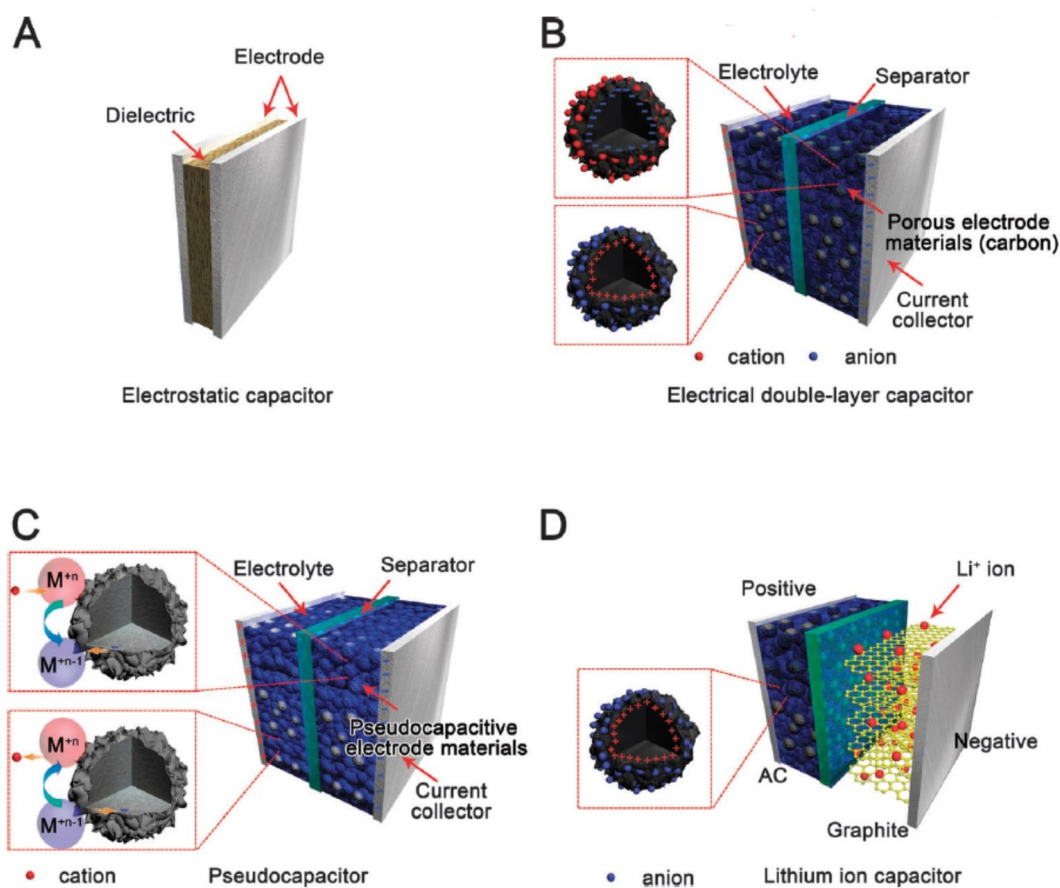


**Figure 2.17:** Schematic diagram for (A) classical electrostatic capacitor, (B) electric double-layer supercapacitor, (C) pseudocapacitor, and (D) hybrid-capacitor [14].

(1) Figure 2.17 (B) Electric double-layer capacitors (EDLCs): the capacitance is produced by the electrostatic charge separation at the interface between the electrode and the electrolyte. To maximize the charge storage capacity, the electrode materials are made from highly porous carbon materials.

(2) Figure 2.17 (C) Pseudocapacitors work due to the fast and reversible faradaic redox reactions allowing to store the charge.

(3) Figure 2.17 (E) Hybrid ESs use both the electrical double-layer (EDL) and faradaic redox mechanisms to store charge. Lately some LIG and carbon/PbO<sub>2</sub> electrodes were developed for this type [14].

The principals of supercapacitors' characterization and diagnosis techniques will be discussed in details in the Experimental Section 3.

### 2.3.3 Elastic Conductive Composites

One of the objectives of this thesis was to study the possibility of creating an electrically conductive elastic composite  $\approx 100 \mu\text{m}$  film based on LIG. The expected material was meant to be used for electrodes in flexible ionic supercapacitors and therefore additional goal was to find an optimal composition for storing high amounts of ionic charges. In this regard, we present a short review of the LIG composite materials known to date which could be suitable for our goals.

So far a few groups reported creation of composites based on elastomeric substrate embedding LIG [21], [15], [17], [16].

**Jeong *et al.* [15] group** created a strain sensor by placing a PI film on the pre-fabricated PDMS film of  $400 \mu\text{m}$  and irradiating the sandwich with an UV 355 nm pulsed laser. In this manner the desired graphitic pattern was implanted directly into the PDMS substrate. The remaining polyimide film was removed, leaving LIG pattern on the PDMS. The structure was then covered with another layer of PDMS to protect the pattern. Schematics of the procedure are presented in Figure 2.18.

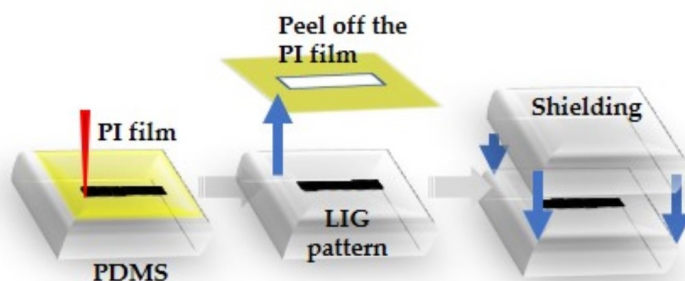


**Figure 2.18:** Process of fabricating a LIG strain sensor embedded in PDMS. Image taken from [15].

This method allowed the fabrication of sensitive and flexible piezoresistive type strain sensors in two simple steps. The sensor was found to have a response time of  $\approx 70$  ms, good linearity to tensile strain, high gauge factor, responsiveness to bending, and a low degree of creep in the bending/release cycle. Some pictures of the strain sensor are provided in Figure 2.19.

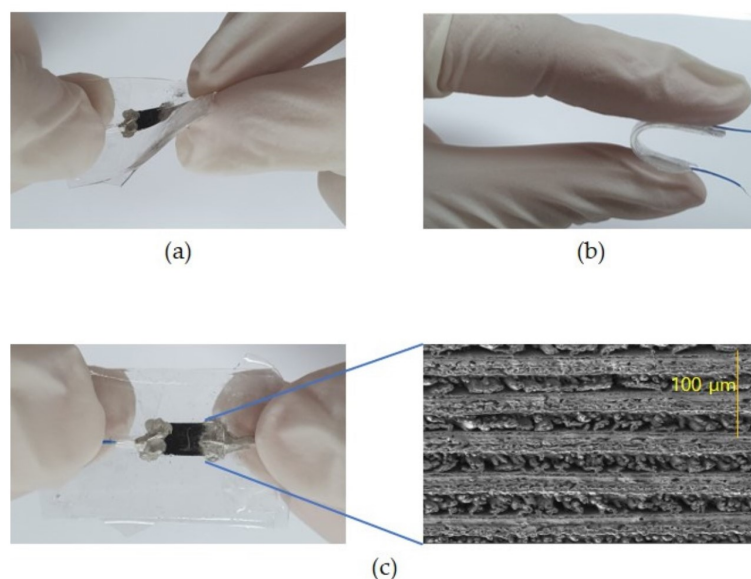


**Figure 2.19:** Photographs of the strain sensor under (a) twisting and (b) bending; (c) SEM image of carbonized pattern embedded on PDMS [15].

In 2016 **Lamberti et al.** [16] described a method to obtain a composite of LIG embedded into PDMS matrix. A porous LIG pattern was at first laser-scribed on a polyimide sheet using a nanosecond pulsed  $CO_2$  laser; afterwards the PDMS mixture (Sylgard 184, Dow Corning, mixing ratio 15:1) was poured onto the conductive graphene circuit, the air bubbles were evacuated under vacuum and the PDMS was cured for 1 h at at 80 deg  $C$ . The LIG/PDMS composite sample was thus manually peeled off from PI substrate. The composite material showed typical mechanical properties of elastomers and at the same time had good electrical conductivity and high surface area. Two layers of the composite were used to prepare symmetrical planar electrochemical double layer (ECDL) supercapacitor cells filled with a Polyvinylpyrrolidone (PVP) gel with 1 M NaCl as shown in Figure 2.20. From cyclic voltammetry (CV) curves obtained at scan rate of 50  $mV/s$  the maximum areal capacitance was calculated to be 650  $\mu F/cm^2$ .

**Lamberti et al.** [17] **group** reported another approach for LIG PDMS composite formation where polyimide powder was firstly dispersed into a liquid PDMS mixture (in different concentrations, namely: 10, 25, 50, and 100 wt% ) followed by PDMS cross-linking. The 1 mm thick composite sheets were then exposed to the  $CO_2$  IR laser treatment, which yielded formation of the typical 3D porous morphology of LIG, fully embedded into PDMS matrix.

The thickness of the porous graphene layer was several tens of micrometers, which guaranteed the integrity, the flexibility and stretchability of the entire one millimeter-thick sample. The results of mechanical tests for the PDMS composites of different PI content are represented in the Figure 2.21.

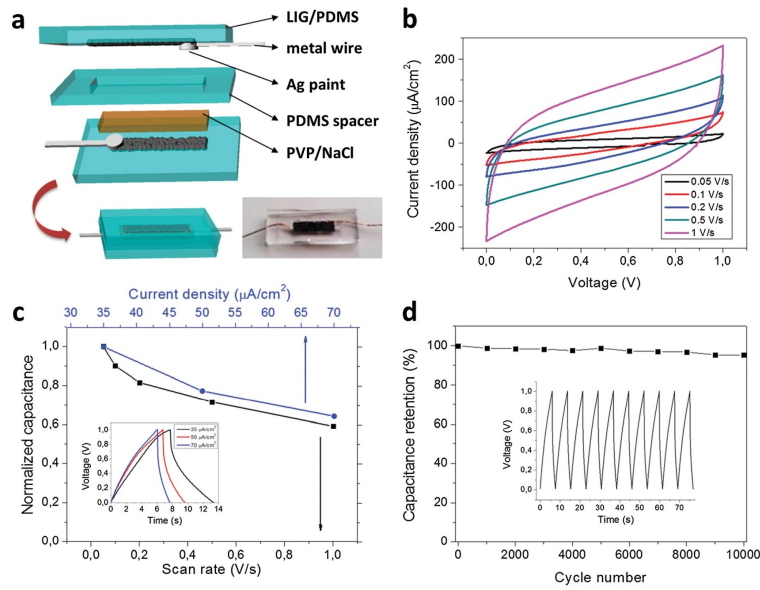


**Figure 2.20:** 3D scheme of a) the LIG/PDMS supercapacitor assembly, in the inset a digital photograph of the assembled device is reported. Electrical characterization: b) CV at different scan-rates, c) capacitance trend *vs.* scan rate and d) capacitance retention. The insets in (c) and (d) show the charge discharge profiles at different current and the cycling behavior at  $70 \mu A/cm^2$ , respectively. Image taken from [16].

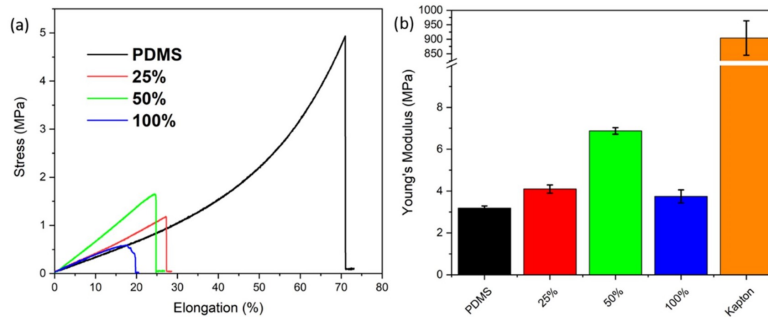


**Figure 2.21:** (a) Stress-strain curves up to the break point for the bare PDMS and the PDMS-PI composite. (b) Comparison of the Young's modulus of the bare PDMS, the PDMS-PI composite, and the Kapton. The reported values were obtained by averaging five different measurements for each type of sample. Image taken from [17].

Using the described method authors fabricated supercapacitor devices of an interdigitated architecture with five pins per electrode as depicted in the inset of Figure 2.22. The cells were filled with 1 M  $Na_2SO_4$  electrolyte solution and tested via cyclic voltammetry (CV), galvanostatic charge and discharge (CDG), and electrochemical impedance spectroscopy (EIS). The maximum resulting capacitance was estimated to be  $25 \mu F/cm^2$  for  $1 \mu A/cm^2$  current density during CDG experiment.

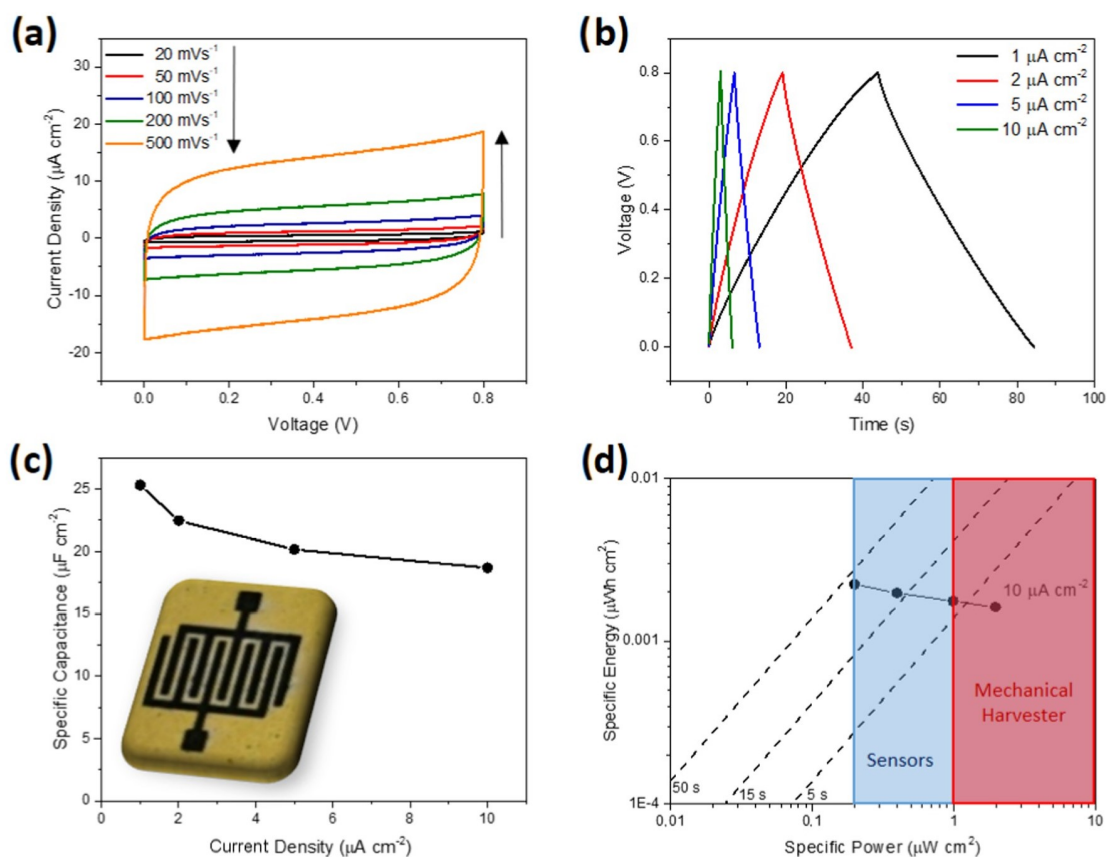


**Figure 2.22:** Two-electrode electrochemical characterization of the SC in 1 M Na<sub>2</sub>SO<sub>4</sub>. (a) CV performed at several scan rates. (b) CDG performed at several current densities. (c) Cell capacitance and (d) Ragone plot derived from CDG tests. image taken from [17].

Recently **LAMPSe group** [21] has developed stretchable and ultrathin ( $\approx 50 \mu\text{m}$ ) skin-conformable conductors based on polyurethane covered with a conductive layer of LIG. Details of the fabrication procedure for this type of composite will be discussed in the Experimental Part 3.



# 3. Experimental

## 3.1 Laser Induced Graphene

### 3.1.1 Direct Laser Scribing Carbonization

In the present work laser induced graphene materials were produced via pyrolysis process in ambient conditions by the commercially available laser cutter/engraver system VLS 2.30 from Universal Laser System. The laser system is equipped with a 30W CO<sub>2</sub> laser source at 10.6  $\mu\text{m}$  wavelength, operating with a pulse repetition frequency  $f_{rep} = 5$  kHz. Raster laser scribing was done at speeds varying from 100 to 830 mm/s. The laser scribing system was equipped with a lens system HPDFO (High Power Density Focusing Optics) which provides a focused beam spot size of 30  $\mu\text{m}$ .

Laser irradiation of polyimide (PI) films, adhesive tapes as well as of polyether ether ketone (PEEK) films enabled direct induction of the graphene formation via a carbonization process as schematically shown in Figure 3.1. As a result of laser processing the integrity of the pyrolyzed film was not completely compromised since a residual part of the initial polymer remains under the LIG allowing it to act as mechanical support.

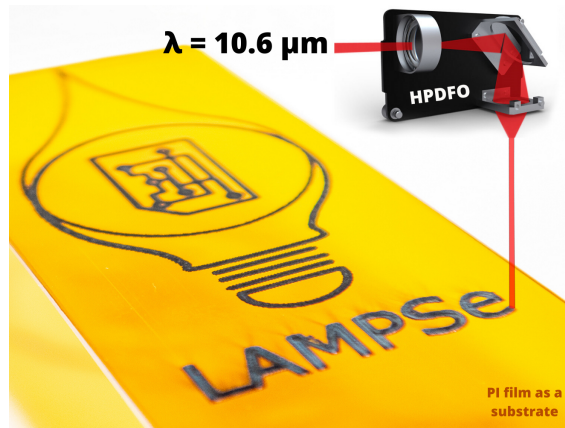


**Figure 3.1:** LIG formation by laser beam treatment

Depending on the laser settings, the laser fluence  $H$  -that is the amount of optical energy delivered per surface area  $J/m^2$ - could be varied. Settings included: laser power, speed of scanning, plane height Z-position as compared to the focal point, raster resolution and amount of scanning lines per scribed area (Image Density). Fluence values in turn affected the final photothermal processes leading to the polymer pyrolysis and LIG formation. Tuning of fluence controls the structure (i.e. amount of crystalline/amorphous carbon) and morphology of the produced LIG.

Earlier [50] it was found that by utilizing the interplay of the varied laser settings two main morphologies of LIG can be obtained on PI Kapton<sup>TM</sup> films. In order to tune the aforementioned parameters for obtaining laser fluence values  $H$  leading to a particular LIG microstructure, a separate study was conducted by Hana Hampel

in her master thesis [18]. As a result of the described work, it was possible to establish a one-to-one correspondence between the laser settings and  $H$ . In the Figure 3.2 obtained by Hana Hampel [18], it is shown how the appearance of the carbon material changes upon the laser settings. For each single Power%-Speed% configurations the laser fluence  $H$  was calculated and the results were layered on top of the mapping with a colour code as shown on the right side. The H-trend corresponded very well to the obtained morphology.

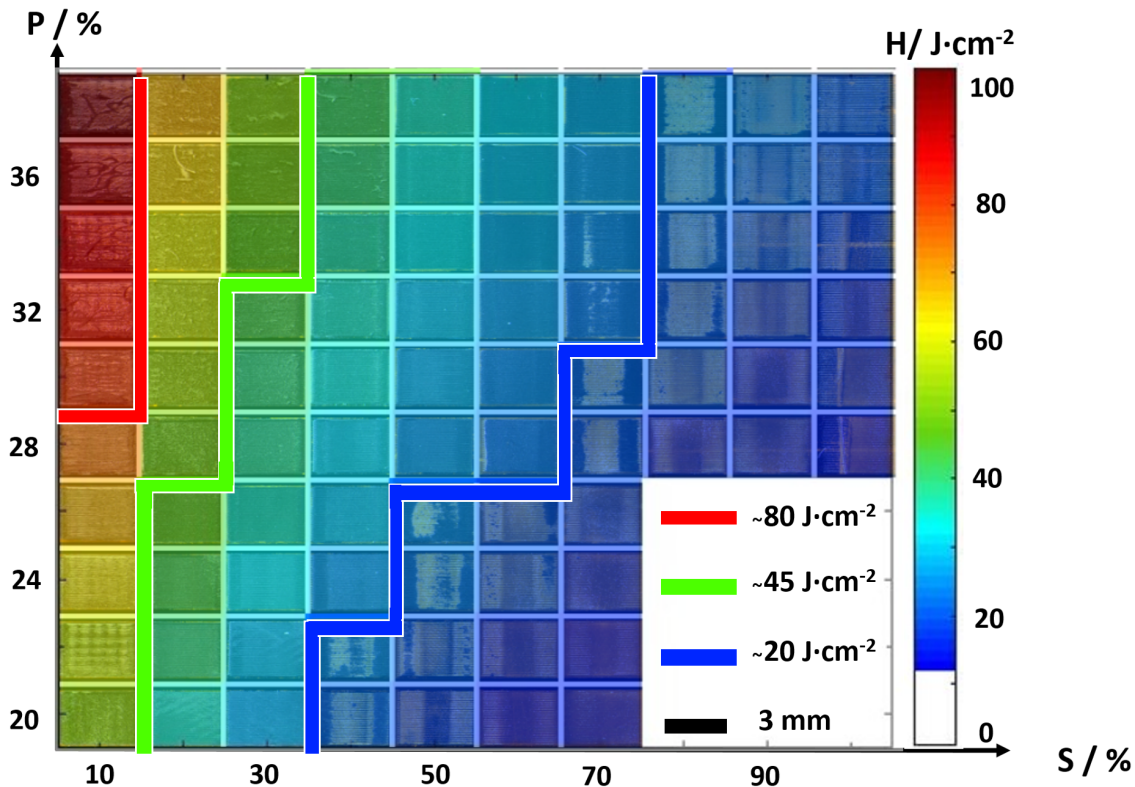


**Figure 3.2:** Map of LIG obtained on Kapton<sup>TM</sup> 50  $\mu\text{m}$  film showing variations upon the laser power within the range between 20% - 40% and speed between 10% - 100%. For laser fluence values  $H < (20 \pm 2) J \times \text{cm}^{-2}$  (blue area) no homogeneous LIG formation was found. Flat-LIG was obtained in the range  $(20 \pm 2) < H < (45 \pm 5) J \times \text{cm}^{-2}$  and LIG-fibres for  $(45 \pm 5) < H < (80 \pm 8) J \times \text{cm}^{-2}$  (green area). The red area, referred to the destroyed polymer sheet, lied in the range  $H > (80 \pm 8) J \text{ cm}^{-2}$  [18]

As LIG precursors we used two types of polyimide material which we distinguish as **Kapton<sup>TM</sup> Film**, a bare polyimide foil, and **Kapton<sup>TM</sup> Tape**, which is a polyimide foil with a polyacrylic adhesive layer on one side. Both materials are produced by DuPont. The PEEK film used is produced by RS PRO Company. Thickness of these precursors materials is provided in 3.1. Before laser scribing the non-adhesive foils were put onto an aluminum 1 mm thick plate and fixed via duct tape. The adhesive precursors were fixed onto 1 mm thick glass slabs. The top surface of the

samples was rinsed with isopropanol and dried before scribing.

In this work two sets of settings were used for LIG preparations. Different LIG types were achieved by varying laser power and Z-distance value, the latter being the offset position of the substrate relatively to the focal point of the laser. The other scribing settings were kept constant as follows: the points per inch (PPI) value was always set to 500, the image density (ID) was set to 5 a.u. (corresponding to a 280  $\mu\text{m}$  spacing between consecutively scribed horizontal lines) and the rastering speed was set to 10% which corresponds to  $100 \pm 10$  mm/s.

Firstly a highly porous conductive carbon material, in our work denoted as LIGP, which appears in the form of ultrathin black flakes stacked on the surface of the polymeric substrate, was obtained at the laser power value set to 11% for polyimide. The fluence used for LIGP was  $H \approx 25\text{J}/\text{cm}^2$ . Another LIG type, called LIGF in this thesis, was obtained at power of 20%, which corresponds to  $H \approx 50\text{J}/\text{cm}^2$ . On polyimide this yielded formation of structures having porous-like material in the bottom layers whereas the top layers consist of fibers. The images of the LIGs obtained with scanning electron microscopy (SEM) can be found in the Results Section at Figure 4.1.

Table 3.1 sums up the LIG types which were prepared.

**Table 3.1:** Polymeric LIG-sources and LIG Types used in this work.

LIG-Source Material	LIG Notation	Power [%]	Speed [%]	Z-distance [mm]
Kapton <sup>TM</sup> Film 50 $\mu\text{m}$	LIGP	11	10	2
	LIGF	20	10	1.7
Kapton <sup>TM</sup> Tape 50 $\mu\text{m}$	LIGP	11	10	2
	LIGP LIFT OFF	11	10	2
	LIGF	20	10	1.7
PEEK Film 100 $\mu\text{m}$	LIGP	11	10	2

The laser pattern design was customized to prepare conductive devices of various shapes which will be further described in the respective sections.

### 3.1.2 Conductive Elastic Biocomposites Based on LIG

#### LIG-PDMS Composite

Polydimethylsiloxane (PDMS, Sylgard 184, Dow Corning, Midland, MI, USA) was used as an elastomeric matrix material for LIG composites. After mixing prepolymer base and curing agent (8/1 w/w ratio) the mixture was degassed in vacuum for 10 minutes before to pour it onto the desired substrates for LIG encapsulation and cured. In the following this material will be denoted as PDMS-8:1. The ratio used here was chosen as it allowed an easier peeling off process of LIG from the PI precursor with respect to the most typical composition of 10:1.

The Kapton film or Kapton adhesive tape was fixed on top of a 70 x 25 mm glass slab and the desired LIG pattern was laser scribed as detailed above. One part of freshly prepared PDMS mixture was then spin coated on top of LIG pattern. The spin coating settings were set to the following parameters:

- spin speed: 600 *rpm*
- spin acceleration: 100 *rpm/s*
- spinning time: 60 *s*

Spin-coated samples were cured at 80 °C for 20 minutes, after which a second layer of PDMS was spin coated with the same parameters on top of the first one. Afterwards the samples were finally cured at 80 °C for 3 hours. Subsequently the specimen were submerged into ethyl acetate (Merck) for 5 - 10 minutes until swollen. This step enabled smooth peeling of the thin composite LIG-PDMS films from the original polyimide substrates. The workflow of the composite production process is illustrated in the Figure 3.3.

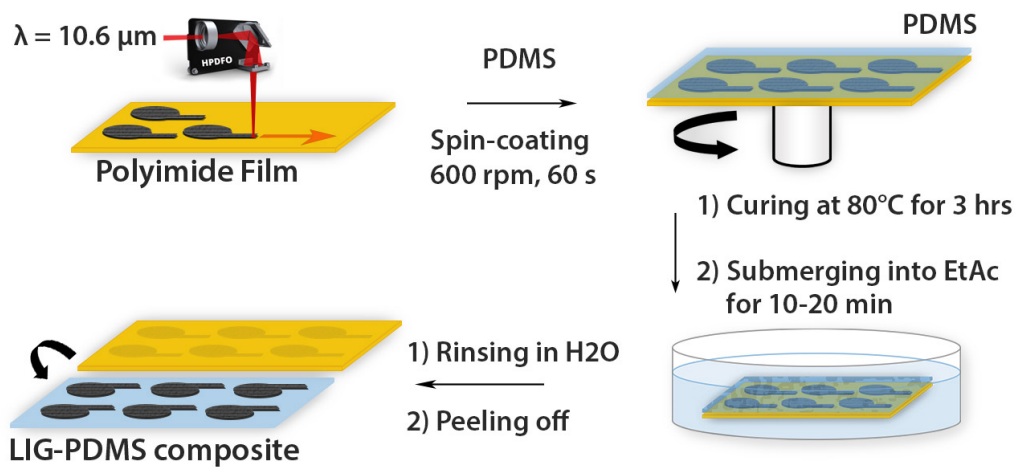


**Figure 3.3:** Preparation of LIG-PDMS Composite

### LIG-MPU Composite

Another type of stretchable LIG composite was prepared by transferring the LIG patterns onto a commercially available medical polyurethane film (MPU) (Fixomull<sup>TM</sup> transparent, BSN Medical). MPU is a thin transparent and waterproof polyurethane film coated with a skin-friendly polyacrylate adhesive.

The technical data for MPU film used in this work is presented in Table 3.2

**Table 3.2:** Medical grade Polyurethane Film [51]

Property	Typical Value
Thickness [ $\mu m$ ]	28
Weight [ $g/m^2$ ]	30
Moisture vapor transmission rate upright/ /[ $g/m^2$ per 24hrs at $37^\circ C$ ]	1400
Tensile Strength [MPa]	0.1
Elongation at break, MD (%)	650

The film has two protection liners: the polyacrylate glue side (bottom) is covered with a glassine paper and the top polyurethane side is covered with a plastic support/release liner. Before transfer the glue side was masked to match the LIG pattern. The mask was prepared via the laser cutter by cutting out the respective pattern only in the glassine paper on the adhesive side of the film. The laser cutter settings were as follows: Power = 2.2%, Speed = 9%, PPI = 500, ID = 5, z-defocus of 1 mm). After this procedure the respective parts of the liner were removed to match the shape of the LIG device. The MPU film was put onto the scribed LIG pattern and a pressure was applied with the help of a cotton tip in order to transfer the LIG material onto the MPU film as it is schematically shown in stages i-iv in Figure 3.4.

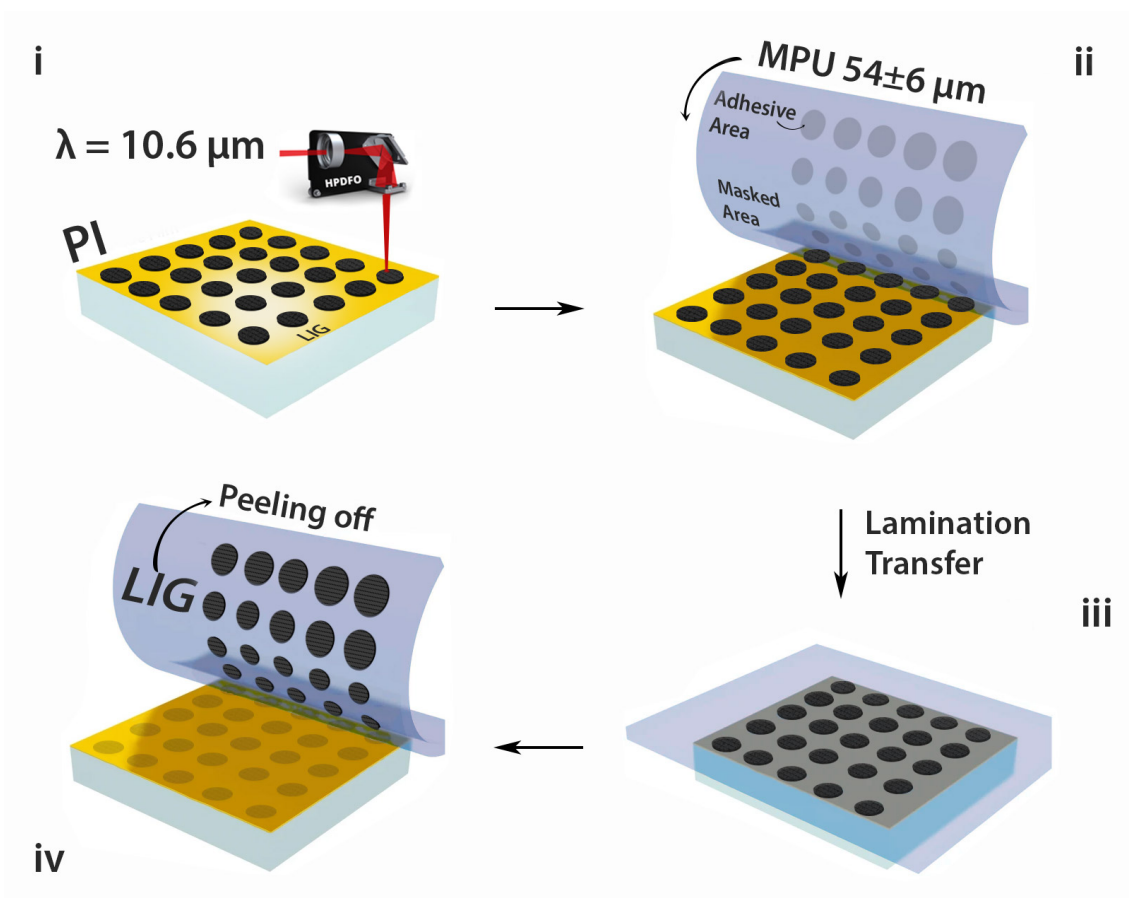


**Figure 3.4:** Preparation of LIG-MPU Composite. (i) Laser scribing on polyimide film for LIG creation; (ii-iv) schematics of LIG lamination transfer onto MPU

## 3.2 LIG Materials Characterization

### 3.2.1 Imaging Techniques

The optical imaging of LIG materials and the LIG based composites was performed with a Leica Wild M3B light microscope. SEM images were obtained with a JEOL JSM-6490LV Scanning Electron Microscope, operating at 5 - 20 kV acceleration voltage.

### 3.2.2 Areal mass loading of LIGs

Further investigations required an estimation of the LIG mass per substrate area, the value which will be further denoted as areal mass loading of an electrode. Thus the mass of LIG per surface area was evaluated for PI, PDMS and MPU substrates. LIG patterns (10 mm in diameter) were laser scribed in raster mode with the respective LIGP and LIGF settings as described earlier in Table 3.1. Afterwards circles were cut out with laser operating at in vector mode. At first each circle was weighed by using the Mettler-Toledo microbalance. To measure the mass of LIG scribed on

the PI the LIG was scraped off from the surface with the aid of a scalpel blade and the mass of the resting round shaped substrate was measured again. To estimate the mass of the LIG material transferred to the MPU adhesive band, the mass of the original LIG-PI circles was measured, after which the LIG was transferred by lamination technique to the PU and the rest mass of the LIG-PI samples was measured again. The difference between the first and the second results was taken as the LIG mass value. The balancing error was 0.0001 g. For the Kapton Film and Kapton Tape the mass densities of respective LIG types were assumed to be equal.

For each type of substrate the procedure was repeated three times and the mass per surface was calculated as the averaged mean value of these three results. For the LIG+PDMS composites it was assumed that all LIG material is transferred from the PI foil, which was in a satisfying agreement with the light microscopy investigation of the resting PI film.

The summary of the obtained values can be found in Table 4.1 in the Results Section 4.

### 3.2.3 Thickness Measurements

The thickness measurement of Kapton<sup>TM</sup> film and tape was performed with a stylus profilometer AlphaStep D-500 from KLA-Tencor operating with a scan length of 5mm, speed set to 0.1 mm/s and loading stylus force set to 1 mg. For each sample, one for Kapton<sup>TM</sup> film and another one for Kapton<sup>TM</sup> tape, at least five measurements per sample were done and the result was taken as a mean average value.

The profilometer set up did not allow to proceed with the thickness measurements for softer materials, such as PDMS. Therefore the evaluation were done by measuring the cross section of samples by means of a light microscope. The estimations were done in five different points and the final result was taken as a range of the obtained values. In order to minimize the uncertainties, which are associated with the described technique, it was made sure that the cross-sections were sliced normal to the film plane and that the slices in turn were then placed normal to the focal plane of the light microscope.

### 3.2.4 Electromechanical Characterization of Composites

**Electromechanical Stretching Setup** The change in electrical resistance of LIGs supported by various substrates to the imposed strain was measured via a custom electromechanical tensile test setup built by A. Dallinger from LAMPSe group (shown in Figure 3.5). The composite sample is mounted between two holders, with one of them fixed to a stage moved by a stepper motor, and the other fixed to a load cell Futek LRF400 with an Amplifier Futek IAA100 to measure the stress imposed on the mounted sample. During the electromechanical tensile tests the load values are read out as an analogue signal via an Arduino microcontroller. The sample holders provide at the same time an electrical contact to the sample through copper plate electrodes. The resistance across the stretched sample is measured via

a Keithley 2601B Source Meter sourcing 10 mA. Controlled strain is imposed on samples by means of a NEMA 17 stepper motor controlled by an Arduino micro-controller. A custom C# software was used to communicate with Arduino and to record the measurements.

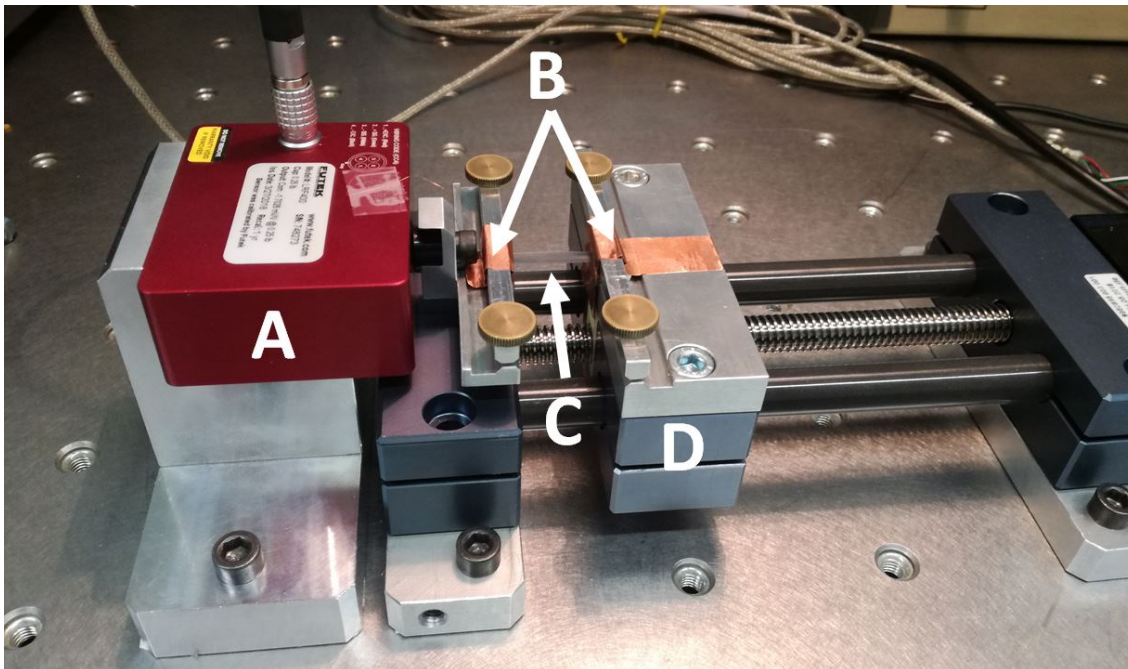


**Figure 3.5:** Electromechanical test setup consisting of load cell (A), electrical contacts (B), sample (C) and movable stage (D) [19]

### Humid Chamber Setup

One of the goals of this thesis was to investigate the electromechanical behaviour of the LIG composites in ambient conditions with varying relative humidity (RH%). This aim required building up a humid chamber around the Stretcher so that the RH of the ambient air around the electromechanically tested specimen could be dynamically regulated and controlled.

The chamber consisted of a polystyrene chamber (built by the LAMPSE bachelor student David Grafinger), a commercially available humidity source (AGPTEK 400mL/H Mini Mist Maker), an DHT22 humidity sensor, controlled by an Arduino Uno<sup>TM</sup> board and a set of fans installed into the walls of the chamber to control the moisture level. RH% values were monitored by the readings from the DHT22 sensor sent over to a PC interface by the pre-programmed Arduino setup.

### Tested Specimen

Test samples were prepared as 40mm x 5mm stripes of LIG supported by various substrates according to the Table 3.4. Since the laser rastering causes the LIG patterns to have anisotropy in their microstructure, for each combination of LIG/Substrate

two types of stripes were prepared: with the laser scribing either parallel to the main axis of the stripe (LIG $\parallel$ ) or normal to it (LIG $\perp$ ).

For the mounting setup 5 mm wide areas on the tips of the samples were left clear of LIG. Samples were mounted in the stretcher so that the freely stretchable part had a length of around  $(20\pm 2)$  mm as shown in Figure 3.6.

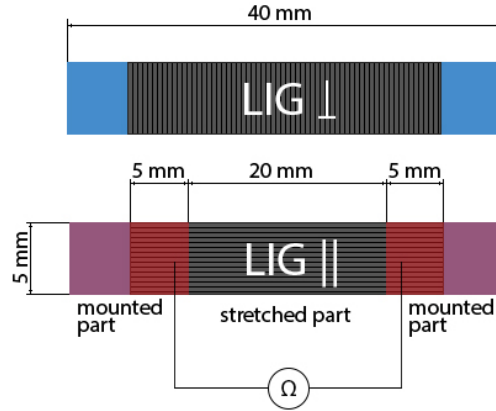


**Figure 3.6:** Schematics of samples for electromechanical measurements: LIG $\perp$  (LIG scribed lines normal to tensile strain direction) and LIG $\parallel$  (LIG scribed lines parallel to tensile strain direction)

**Table 3.3:** Settings of Electromechanical Stretching Tests

Strain $\epsilon$ [%]	Speed $v$ [mm/s]	Repetition
5	$0.53\pm 0.01$	3
10	$0.53\pm 0.01$	3
30	$0.53\pm 0.01$	3

**Table 3.4:** List of Samples for Electromechanical Tests

Sample #	LIG Type <sup>1</sup> and alignment	Substrate
1	LIGP	PDMS-8:1
2	LIGF⊥	PDMS-8:1
3	-	PDMS-8:1
4	LIGP	MPU
5	LIGF⊥	MPU
6	-	MPU

Conditions of the stretching tests were set-up as described in Table 3.3. Strain  $\epsilon$  is defined as  $100\% * l/l_0$ , where  $l$  and  $l_0$  are the stretched length and initial length in a relaxed state respectively. These settings were chosen so that consecutive cycles of stretching at different strain could be imposed, with the cycle at the highest strain up to 30% being the last in the series. Since each strain cycle was applied one after another in series, the possible effects were accumulated and this fact was used for a rough estimation of cycling fatigue behaviour of the investigated flexible devices. Each sequence of the stretching cycles was repeated in ambient conditions of 45-66% as well as at 92-95% *RH*.

Additionally the samples were tested at dynamically changing *RH* conditions. A respective sample was mounted and subjected to a fixed strain  $\epsilon$  of 30% while the humidity rate was varied from 66% to 95% and back to 66% in one continuous run.

In all experiments two types of dependencies were recorded: Strain *vs.* Time as well as Normalized Resistance  $R/R_0$  *vs.* Strain, where  $R_0$  relates to the resistance before the first stretching.

### 3.2.5 Sheet resistance of LIG Porous and LIG Fibers

The samples for this part of the project were tested in collaboration with David Graphinger and Benedikt Kraxberger, bachelor students.

Specimen presented by 10x10 mm LIGF square embedded into PDMS8:1 were brought in contact with the nodes of the four point probe. Three different alignments (parallel, perpendicular and 45°) between the laser scribing direction and nodes were tested. A stable current of 3 mA was used for all cases.

---

<sup>1</sup>Laser settings as according to the Table 3.1

### 3.2.6 Gas Adsorption Measurements (BET)

In order to characterize the surface area and the porosity of the LIG materials the volumetric gas adsorption measurements were performed with two different techniques.

#### Surface Area and Porosity Volume Determination for LIG Powders

Firstly the classical powder BET analysis, *i.e.* the volumetric physical adsorption measurements of isotherms, was performed with Micromeritics 3Flex equipment at the Institute of Physical and Theoretical Chemistry at TU Graz.

Two series of experiments, for LIGP and LIGF, were completed. The powders of LIG materials were prepared via laser scribing on Kapton<sup>TM</sup> 50  $\mu\text{m}$  films. In case of LIGP both sides of the film were lasered in a sequence and the porous material was scraped off. For the LIGF only one side of the film could be used as the pyrolysis depth of penetration was too high ( $\approx 30 \mu\text{m}$ ) to allow the usage of both sides.

**Table 3.5:** Powder BET Measurements Characteristics

LIG Sample <sup>1</sup>	mass [g]	$p/p^0$ interval	BET $p/p^0$ interval
LIGP	0.0627	0.0001 - 0.99412	0.010 - 0.095
LIGF (1)	0.0186	0.0002 - 0.3440	0.10 - 0.30
LIGF (2)	0.0235	0.0003 - 0.9923	0.10 - 0.30
LIGF (3)	0.0206	0.9966 - 0.1041	-

Altogether 0.0580 g of LIGP and 0.0627 g of LIGF were used. The samples were weighed three times and the mean value was taken as the final value. Mass balancing error was 0.0001 g for all tests and determined the related specific area error. The LIGP powder was used for one experiment and the LIGF was split in three parts of 0.0186 g, 0.0235 g and 0.0206 g for three subsequent measurements. Before adsorption experiments the samples were degassed at vacuum conditions at 140 °C for 4 hours. The characteristics of the surfaces analysis can be found in Table 3.5. The test with LIGF (3) was executed in desorption mode after the sample was exposed to the saturating relative pressure  $p/p^0$  of 0.9918.

---

<sup>1</sup>Laser settings as according to the Table 3.1

## Gemini<sup>TM</sup> Technique for Surface Area and Porosity Volume Determination

The second series of gaseous adsorption experiments was performed by Dr. Fr. Borghi at the University of Milan by applying the Gemini<sup>TM</sup> volumetric method, shortly described in Subsection 2.2.2. For this analysis a number of testing samples were prepared in a form of stripes of 55 x 5 mm supported by the various substrate materials as indexed in the Table 3.6. LIG samples were prepared from three different foil types, namely the Kapton<sup>TM</sup> Film 50  $\mu\text{m}$ , Kapton<sup>TM</sup> Tape 50  $\mu\text{m}$  and PEEK Film 100  $\mu\text{m}$ . For the Samples #4, 9 and 10 the LIG was firstly laser scribed on the corresponding Kapton<sup>TM</sup> material, after which it was embedded into PDMS-8:1 by spin coating at 600 rpm and further treated as described in the Section for LIG+PDMS 3.1.2.

**Table 3.6:** The List of Samples Prepared for Gemini BET analysis

Sample #	Number of samples	LIG Type <sup>1</sup>	Substrate Material
1	3	LIGP	Kapton <sup>TM</sup> Film 50 $\mu\text{m}$
2	3	LIGF	Kapton <sup>TM</sup> Film 50 $\mu\text{m}$
4	3	LIGF	Kapton <sup>TM</sup> Film 50 $\mu\text{m}$ //PDMS-8:1
5	3	LIGP	PEEK Film 100 $\mu\text{m}$
7	3	LIGP	Kapton <sup>TM</sup> Tape 50 $\mu\text{m}$
8	3	LIGF	Kapton <sup>TM</sup> Tape 50 $\mu\text{m}$
9	2	LIGP	Kapton <sup>TM</sup> Tape 50 $\mu\text{m}$ //PDMS-8:1
10	3	LIGF	Kapton <sup>TM</sup> Tape 50 $\mu\text{m}$ //PDMS-8:1
11 <sup>2</sup>	2	-	Kapton <sup>TM</sup> Film 50 $\mu\text{m}$
12 <sup>2</sup>	3	-	PEEK Film 100 $\mu\text{m}$
13 <sup>2</sup>	3	-	PDMS-8:1

<sup>1</sup>Laser settings according to the Table 3.1

<sup>2</sup>Blank samples of the substrate material for further comparison

Gas adsorption measurements were performed via a Gemini<sup>TM</sup> surface area analyzer (Micromeritics, model 2365). The principle of the experimental set-up is shown in Figure 3.7. Two gas reservoirs A are filled with equal volumes of the desired adsorptive, nitrogen in the case of this work. From the reservoirs, gas is induced into the sample tube ( $\approx 22 \text{ cm} \times 0.7 \text{ mm}$ ) by a servo valve (F) that reacts to the rate of adsorption. Transducer (B) detects any pressure difference between the two tubes and causes another servo valve (C) to adjust the pressure within the balance tube to negate any pressure differential. A third pressure transducer (D) monitors the pressure between the two reservoirs to determine the differential quantity of gas, the difference being the quantity that is adsorbed on the sample. Transducer E monitors pressure within the sample tube causing a fast response servo valve (F) to increase or restrict the flow of gas to the sample tube as necessary to maintain a constant equilibrium pressure within the sample tube as adsorption occurs [20].

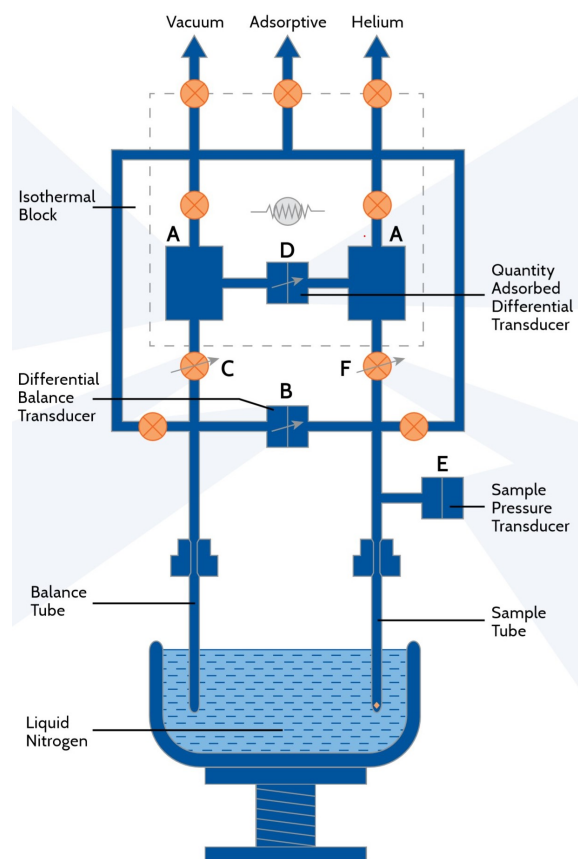


**Figure 3.7:** The Gemini technique principle for surface area and pore volume determination. Image taken from [20]

Before each measurement samples were degassed under a constant helium flux at  $140^\circ\text{C}$  over night using a dedicated unit, in order to remove any contaminants which may have been adsorbed onto the pores of the materials. During the adsorption analysis, the values of the relative pressure ( $p/p^0$ ) ranged from 0.05 to 0.99 for the acquisition of the isotherm plot, while the free space in the test tube was determined by employing a helium gas injection prior measurement. The specific surface area

( $A_{BET}$ , expressed in  $m^2/g$ ) was calculated considering the relative pressure interval between 0.05 and 0.25. The associated error was obtained by considering the microbalance uncertainty to be  $0.01 \mu g/cm^2$ .

### 3.2.7 Atomic Force Microscopy (AFM) of LIGs

For the quantitative morphological and topological characterization of LIGs supported by different substrates the AFM investigation approach as described in the Section 2.2.2 of the Theoretical part was chosen.

The round shaped, 10 mm in diameter, LIG samples were prepared on various substrates as described in Table 3.7.

**Table 3.7:** The List of Samples Prepared for AFM analysis

Sample #	LIG Type <sup>1</sup>	Substrate Material
1	LIGP	Kapton <sup>TM</sup> Film 50 $\mu m$
2	LIGF	Kapton <sup>TM</sup> Film 50 $\mu m$
3	LIGP	Kapton <sup>TM</sup> Tape 50 $\mu m$ //PDMS-8:1
4	LIGF	Kapton <sup>TM</sup> Tape 50 $\mu m$ //PDMS-8:1

The main interest was to investigate the morphological differences between the LIG (*i.e.* LIGP and LIGF) supported by the the polyimide foil *in situ* and the composite material LIG-PDMS.

According to the technique explained in [9] the morphology of LIG samples was characterized by Atomic Force Microscopy (AFM) using a Bioscope Catalyst (Bruker) operated in Peak-Force Tapping Mode in air, equipped with silicon nitride cantilevers mounting single crystal silicon tips. The nominal radius of the AFM tip is 8–12 nm, resonance frequency in the range 50–90 kHz, and force constant  $k = 0.4 N/m$ . Several images with different magnification were acquired with scan rate 0.5 Hz and sampling resolution  $2048 \times 512$  points, in order to characterize the morphology of the interface. The images were flattened by line-by-line subtraction of first and second order polynomials in order to remove artifacts due to sample tilt and scanner bow. From flattened AFM images, the interfacial specific area ( $A_{AFM}$ ) was calculated as the ratio of three-dimensional surface area scanned by AFM tip to the projected area.

---

<sup>1</sup>Laser settings as according to the Table 3.1

### 3.3 Flexible Supercapacitors based on LIG

The aim of this part of the project was to investigate the prospects of using LIG as an electrode material in thin and flexible symmetrical supercapacitor cells based on inorganic biocompatible electrolytes. It was assumed from the beginning that the LIG microstructure may have an impact on the electrochemical behaviour of the cells. Therefore various cell types based on LIGP and LIGF supported by three different flexible substrates, namely PI, PU and PDMS, were designed and prepared for the following investigations of their voltage behavior in charging/discharging experiments.

#### 3.3.1 LIG Based Electrodes. Design and Production

A supercapacitor cell can be assembled in different ways. Most commonly seen types include coin cells and Swagelok<sup>TM</sup> type cells. The latter is very popular in laboratory research as it can be cleaned and reused again for multiple times, whereas coin cells have to be dismantled after the experiments. In this work three types of cell setup were tested: Swagelok<sup>TM</sup>, Flat, Rolled.

Before describing all modifications which were probed, we reference to the Table 3.8 which lists the details about the cells. The nomenclature of cells types sticks to the following logic:

- The first letter denotes the type of the cell assembly: 'S' for Swagelok<sup>TM</sup>, 'F' for Flat and 'R' for Rolled;
- The number after the first letter stands for the type of the substrate used as the LIG carrier: '0' for Kapton<sup>TM</sup>, '1' for PDMS, '2' for MPU;
- The last letter stands for the LIG type: 'F' for fibers, 'P' for porous.

Altogether five configurations for Swagelok<sup>TM</sup> cells were tested, denoted as S0F, S0P, S1F, S2F, S2P. There were six flat configurations  $F1F_{square}$ ,  $F1P_{square}$ ,  $F1F_{round}$ ,  $F1P_{round}$ , F2F and F2P. For the rolled design the modifications R1F and R1P were prepared. In all cases  $NaNO_3$  1M solution (from Alfa-Aeser) was used as electrolyte. There were at least three cells of each type prepared to minimize the statistical errors during electrochemical tests.

**Table 3.8:** The List of LIG Based SC ionic cells based on  $NaNO_3$  1M electrolyte

Cell Type #	LIG Type <sup>1</sup>	Substrate Material	Cell Design
S0P	LIGP	Kapton <sup>TM</sup> Film 50 $\mu$ m	Swagelok <sup>TM</sup>
S0F	LIGF	Kapton <sup>TM</sup> Film 50 $\mu$ m	Swagelok <sup>TM</sup>
S1F	LIGF	PDMS-8:1	Swagelok <sup>TM</sup>
S2P	LIGP	MPU	Swagelok <sup>TM</sup>
S2F	LIGF	MPU	Swagelok <sup>TM</sup>
<i>F1F<sub>square</sub></i>	LIGF	PDMS-8:1	Flat
<i>F1P<sub>square</sub></i>	LIGP	PDMS-8:1	Flat
<i>F1F<sub>round</sub></i>	LIGF	PDMS-8:1	Flat
<i>F1P<sub>round</sub></i>	LIGP	PDMS-8:1	Flat
F2F	LIGF	MPU	Flat
F2P	LIGP	MPU	Flat
R1F	LIGF	PDMS-8:1	Rolled
R1P	LIGP	PDMS-8:1	Rolled

### 3.3.2 Swagelok<sup>TM</sup> Setup

First objective was to investigate the dependence of LIG electrostatic double-layer capacitance on its type and the substrate material in a series of cyclic voltammetry (CV) and Galvanostatic Cycling with Potential Limitation (GCPL) experiments incorporating the Swagelok<sup>TM</sup> cell type (see Figure 3.9). The specifics of this setup is that the electrical contact between the collector and the electrode needs to be in the plane of the collector on the back side of the flat electrode. Therefore virtually

<sup>1</sup>Laser settings as according to the Table 3.1

no wiring can be used. Previously, a solution was found by LAMPSe group to solve a similar problem by integrating the Vertical Interconnect Access (VIA) [21]. Descriptive schematics is shown in Figure 3.8a. In a prepared round shaped  $\varnothing 10\text{mm}$  LIG electrode a group of 24 small holes ( $\varnothing \sim 80\ \mu\text{m}$ , Figure 3.8c) was laser-cut. For the PI it was found that depending on the laser settings and the hole diameter the edges around might remelt and close the hole just after the laser impulse (Figure 3.8b). Therefore the respective settings were found (Power 28% Speed 10% PPI 500 Z-defocus 1 mm ID5) which allowed to ensure that the cavities stayed open. These holes were small enough ( $\approx 70\ \mu\text{m}$ ) so not to affect robustness and flexibility of the substrate materials. The cavities were then filled with silver ink (Leitsilber 200 from Ted Pella) and dried at  $85\ ^\circ\text{C}$  for 20 min. The porous structure of LIG as well as its satisfying wettability by the silver ink allowed the liquid to spread into the electrode bulk, forming conductive thin LIG/Ag composite wires and providing a good electrical connection to the back side of the electrode.

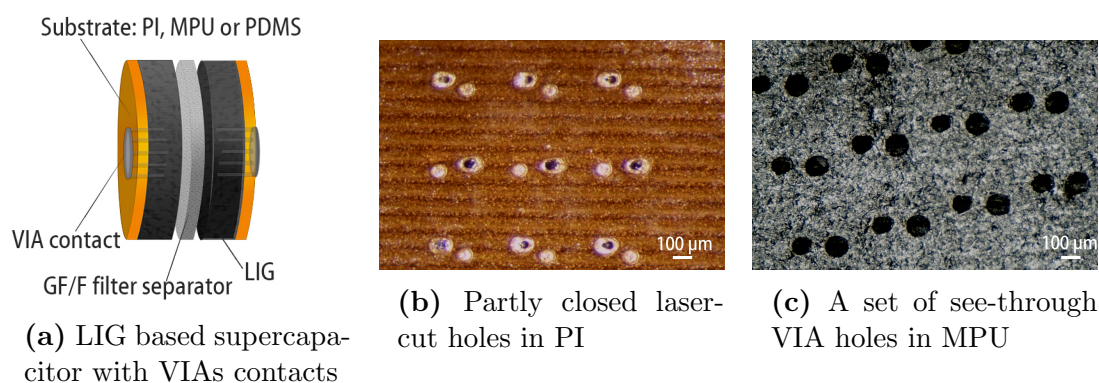


**Figure 3.8:** Light microscope pictures of VIA contact holes and schematics of a LIG based supercapacitor

The electrical contact of all prepared LIG electrodes was controlled before the Swagelok<sup>TM</sup> cells were assembled as shown in Figure 3.9. The Teflon<sup>TM</sup> housing contains two stainless steel collectors which enclose the investigated supercapacitor cell in the middle. Aqueous solution of sodium nitrate  $\text{NaNO}_3$  (Alfa-Aeser) in 1M concentration prepared from deionized  $\text{H}_2\text{O}$  was used as an electrolyte. The Whatman glass microfibre filter (GF/F) had a thickness of  $260\ \mu\text{m}$ .

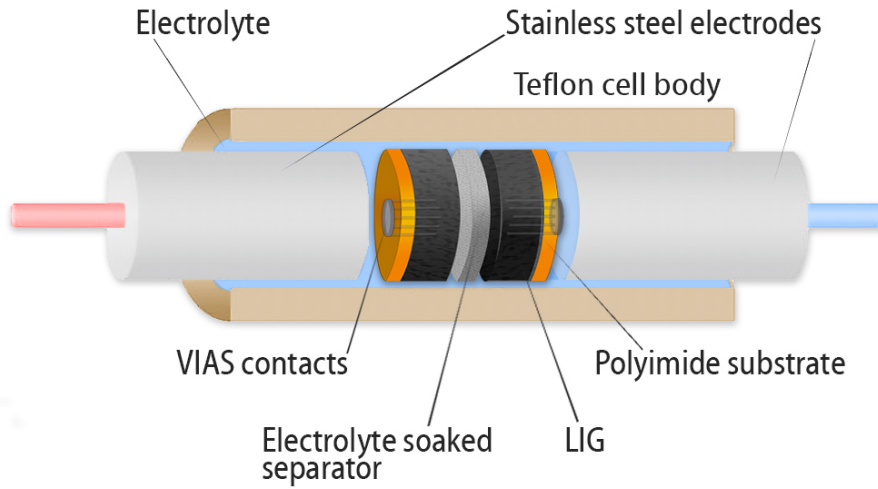


**Figure 3.9:** Swagelok<sup>TM</sup> cell setup for cyclic voltammetry experiments

### 3.3.3 Thin stretchable supercapacitor cells

Encouraged by the preliminary results with Swagelok cells (see Results Section 4), the feasibility of fabricating a biocompatible thin and stretchable LIG supercapacitor cell, applicable for skin wearable devices, was investigated.

A number of flat cell modifications were prepared and tested as described below:

**F1F<sub>square</sub>** - LIGF-PDMS-8:1 electrodes, encapsulated into MPU,  $15 \times 15 \text{ mm}^2$ , Pt terminals.

**F1P<sub>square</sub>** - LIGP-PDMS-8:1 electrodes, encapsulated into MPU,  $15 \times 15 \text{ mm}^2$ , Pt terminals.

Type *F1F<sub>square</sub>* and *F1P<sub>square</sub>* electrodes were prepared from LIG-PDMS-8:1 conductive composite in a form of a  $15 \times 15 \text{ mm}^2$  square which had a  $2 \text{ mm} \times 15 \text{ mm}$  foot (Figure 3.10). This "foot" terminal had an advantage of being as flexible as the rest of the electrode and at the same time had the same conductivity as the rest which allowed it to be used as an electrical wiring contact. To ensure proper electrical contact an additional Pt foil was applied onto each terminal. Square pieces  $15 \times 15 \text{ mm}^2$  of MPU adhesive film (as described earlier in this section) were used to support electrodes and to assemble a leak-proof cell. Each of the electrodes was placed LIG-side up onto an adhesive side of an MPU piece. The sandwich of electrodes was spaced by a  $260 \mu\text{m}$  glass fiber GF/F separator film (from Whatman) to eliminate electrical short cut, after which it was encapsulated into MPU film to form a cell.

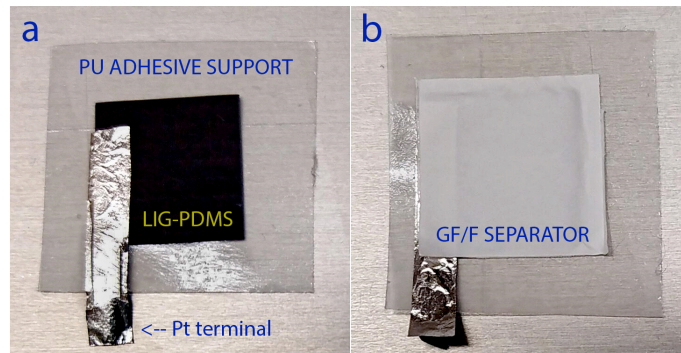


**Figure 3.10:** LIG-PDMS flexible thin supercapacitor device with composite wiring

After assembly the interfacial volume of the cells was filled with 0.01 ml of 1M  $\text{NaNO}_3$  electrolyte solution prepared with deionized  $\text{H}_2\text{O}$  by a syringe, the piercing hole was then sealed by PDMS.

**F1F<sub>round</sub>** - LIGF-PDMS-8:1 encapsulated into MPU/PDMS,  $d$  10 mm, Ag paste + Amphenol FCI clincher connectors.

**F1P<sub>round</sub>** - LIGP-PDMS-8:1 encapsulated into MPU/PDMS,  $d$  10 mm, Ag paste + Amphenol FCI clincher connectors.

This type of cells was similar to Types  $F1F_{square}$  and  $F1P_{square}$  with a difference that the electrodes had a shape of a 10 mm circle with a 1.5 mm wide and 15 mm long foot as shown in Figure 3.11. At the end of the feet VIAS contacts were made to ensure better contact to Amphenol FCI Clincher Connectors (2 Position, Male).

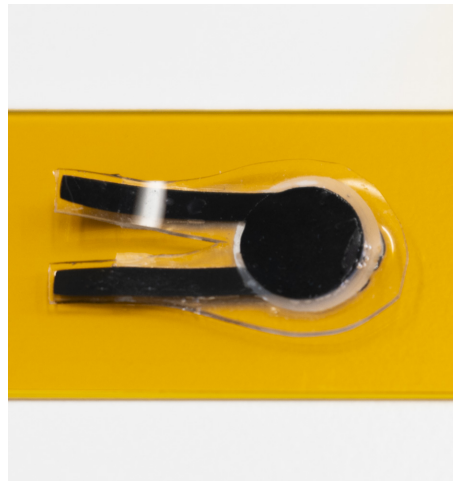


**Figure 3.11:** LIG-PDMS flexible thin supercapacitor device of a round shape

**F2F** - LIGF-MPU, encapsulated into MPU,  $d$  10 mm, Ag paste + Amphenol FCI clincher connectors.

**F2P** - LIGP-MPU, encapsulated into MPU,  $d$  10 mm, Ag paste + Amphenol FCI clincher connectors.

The electrodes of the Type F2, identical in shape to the round Type F1, were prepared by transferring the LIG onto a pre-cut MPU carrier, as described in the previous section "LIG-MPU Composite", and encapsulating the device into MPU film as well.

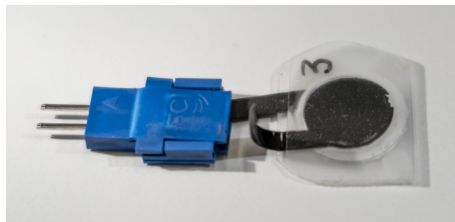


**Figure 3.12:** LIG-MPU flexible thin supercapacitor device of a round shape with Amphenol FCI Clincher Connector

The cross-section thickness of assembled flat devices was  $\approx 0.5 - 1$  mm.

### 3.3.4 Rolled flexible supercapacitor cells

**R1F** - LIGF-PDMS-8:1,  $d$  10 mm, rolled in thermo-shrink, aluminum tube terminals.

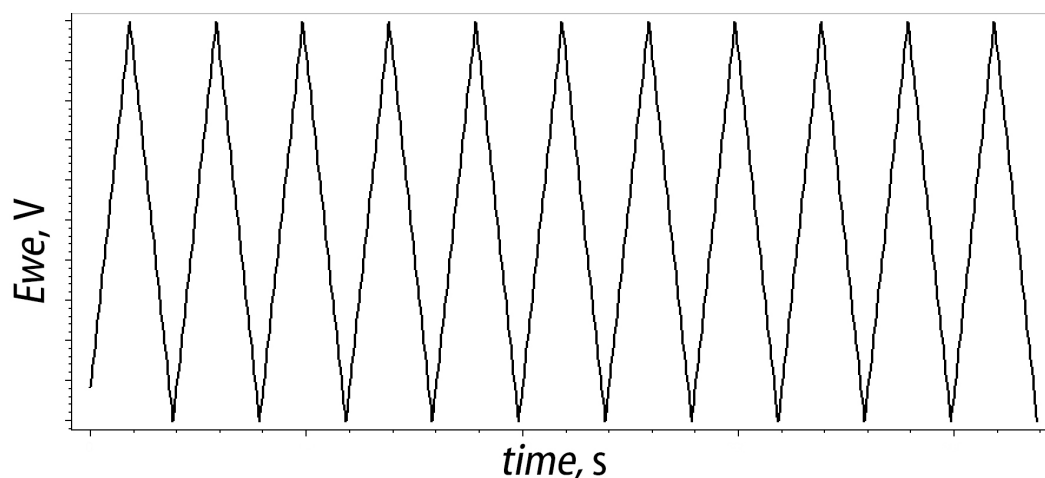
**R1P** - LIGP-PDMS-8:1,  $d$  10 mm, rolled in thermo-shrink, aluminum tube terminals.

Type R1 electrodes were of the same shape as the Type F2. They were made out of LIG-PDMS-8:1 composite. The two electrodes were first assembled into a flat sandwich configuration with a glass fiber separator in-between, after which the sandwich was tightly rolled and put into an heat shrink tubing from TE<sup>TM</sup> (Single Wall, 4.75 mm, Medical Grade Crosslinked Polyolefin) in a way so the terminal feet would be outside of the tube. The roll was then put over a heating source to let the tube shrink and tighten the device. The device was filled with the electrolyte via syringe and the LIG feet were further clinched with thin aluminum terminals for a better electrical contact as shown in Figure 3.13.

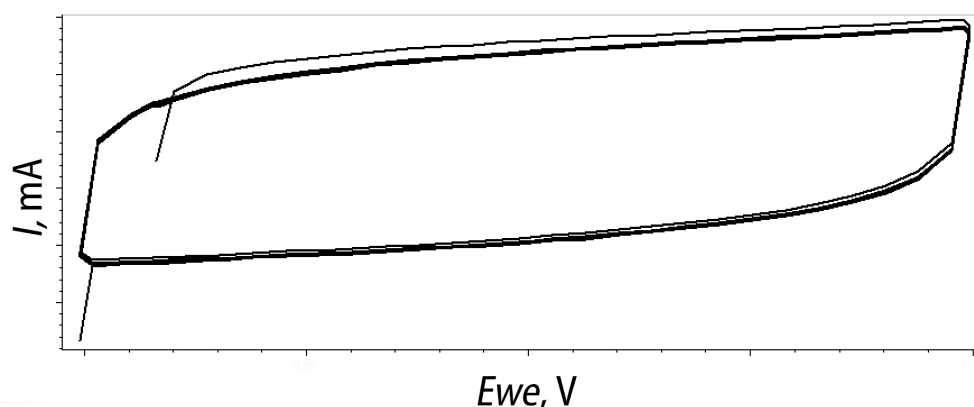


**Figure 3.13:** LIG-PDMS rolled supercapacitor device with one terminal covered with Al contact

### 3.3.5 Electrochemical Characterization



(a) Takes from EC-Lab<sup>TM</sup> potential versus time program for CV showing the forward and reversed linear potential ramp



(b) Cyclic Voltammogram of measured current versus applied potential

**Figure 3.14:** Experimental data recorded during a CV test

Electrical performance of the assembled cells was investigated in cooperation with Dr. Qamar Abbas by the means of Cyclic Voltammetry (CV), Galvanostatic Cycling with Potential Limitation (GCPL) as well as with Impedance Spectroscopy for a part of the cells. The measurements were performed by Dr. Qamar Abbas at the Institute of Chemistry and Technology of Materials at TU Graz via potentiostat MPG-2 Device operated by EC-Lab<sup>TM</sup> software.

The CV method involves linearly varying, *i.e.* sweeping, an electrode potential between two limits at a specific scanning rate while recording the current that flows through the electrochemical cell. After the voltage reaches a certain maximum value, the potential is reversed and so is the current as well. The test involves a certain amount of cycles repeated one after another. The variation of the voltage in time can be seen

in 3.14a. The change in the potential causes a respective current response, which in case of the two-electrode setup is recorded as a function of the voltage difference between the two leads as shown in Figure 3.14b. CV provides information about the electrochemical response of the system, which can be chemical reactions happening during the measurement as the potential changes or/and charge storage. For the supercapacitors the final curve shape helps to evaluate which of the two known charge storage mechanisms (electric double layer (EDL) or the faradaic charge transfer) is involved into the operation of the device. For the EDL cells, in which no redox reactions taking place, the ideal cycle has a rectangular shape, as this corresponds to the situation of a maximum charge storage in absence of a non-linear  $I(V)$  behaviour. Undesired chemical reactions on electrode can be avoided kinetically by choosing high enough scanning rates, or thermodynamically by selecting the right potential window where the materials stay chemically inactive. The latter is preferable for the materials with high inner resistance as the higher scanning rates may hinder the diffusion of the charges to the micro- and mesopores of the electrodes, which is necessary for the storage to happen.

Together with the CV measurements the method of Galvanostatic Cycling with Potential Limitation (GCPL) was employed. In these tests one cycle consists of two stages. At first the device is charged at a constant current until the pre-defined potential difference between the two electrodes is achieved. After that the cell is discharged with the opposite current down to the zero potential. The method is widely utilized in supercapacitor characterization as not only it allows to estimate the principal electrical characteristics of the cells but also their cycling stability and performance over time. Similar to CV, the characteristic shapes of  $V(t)$  GCPL curves (shown in Figure 3.15) and their deviations allow to make estimations regarding the storage mechanisms taking place in the device. EDL cells with low inner resistance have triangular appearance and no potential drop at the beginning of the discharging stage. Potential scanning  $dE/dt$  rates which are defined as the slope of the charging and discharging branches of the graph, together with the chosen value of the applied current have a great impact on the shapes of the curves and therefore have to be accurately selected.

In order for the electrical properties evaluated by cyclic voltammetry to be comparable to the data obtained in galvanostatic experiments, the measurements with each cell were performed in series and as good as it was achievable for the common voltage potential ranges.

Each device was cycled at ambient temperature ( $\sim 19^\circ\text{C}$ ). The settings of the measurements for the Swagelok cells can be found in Table 3.9.

**Table 3.9:** CV and GCPL experiment settings for Swagelok Cells

Electrode Type	Cyclic Voltammetry		GCPL	
	Sweeps [V]	$dV/dt$ [mV/s]	$V_{max}$ [V]	$I$ [mA]
S0P, S0F	0 - 0.2	5/10/20/50/100/200	0.2	0.04 - 1
	0 - 0.2/0.3/0.4/0.5	5	0.2 - 0.5	0.1
	0 - 0.6/0.7/0.8/0.9/1.0/1.1/1.2	5	0.6 - 1.2	0.1
S1F	0 - 0.2	5/10/20/50/100/200	0.2	0.08 - 1.6
	0 - 0.2/0.3/0.4/0.5	5	0.2 - 0.5	0.2
S2P, S2F	0 - 0.1	2	0.1	0.018
	0.1 - 0.2	2	0.2	0.018
	0 - 0.3	2	0.3	0.018
	0 - 0.4	2	0.4	0.018
	0 - 0.2 <sup>1</sup>	5/10/20/50/100/200	-	-

The next series of CV and GCPL experiments was performed with the thin cells at the identical to Swagelok cells conditions. The retrieved data allowed to calculate the electrical characteristics which are relevant for the supercapacitor devices. Capacitance of a cell was calculated from the CV curves by employing Equation 3.1:

$$C_{(CV)} = \frac{1}{2 \times (dV/dt)_{CV} \times (V_2 - V_1)} \times \int_{V_1}^{V_2} I(V) dV \quad (3.1)$$

and from the GCPL data with Equation 3.2:

$$C_{(GCPL)} = \frac{I_{discharge}}{(dV/dt)_{GCPL}} \quad (3.2)$$

---

<sup>1</sup>This device could not be identified as the type of LIG was not put in the protocol. However the CV curves showed very good behaviour

Where  $(dV/dt)_{CV}$  [V/s] is the CV scan rate;  $V_2, V_1$  [V] - the limits of the CV potential sweep;  $I(V)$  [A] - CV current curve;  $I_{discharge}$  - GCPL current at discharge;  $(dV/dt)_{GCPL}$  - slope of the discharge part of a GCPL curve.

Specific gravimetric capacitance  $C_g$  [F/g] and specific areal capacitance  $C_A$  [ $\mu$ F/cm<sup>2</sup>] were calculated with Equations 3.3 and 3.4 respectively:

$$C_g = \frac{C}{m} \quad (3.3)$$

$$C_A = \frac{C}{s} \quad (3.4)$$

Where  $m$  [g] is the total mass of an active material on both electrodes;  $s$  [cm<sup>2</sup>] - total area of the active positive and negative electrodes.

Specific energy gravimetric and areal densities -  $E_g$  [Wh/g] and  $E_A$  [ $\mu$ Wh/cm<sup>2</sup>]:

$$E_g = \frac{1}{2} \times C_g \times \frac{\Delta V^2}{3600} \quad (3.5)$$

$$E_A = \frac{1}{2} \times C_A \times \frac{\Delta V^2}{3600} \quad (3.6)$$

With the knowledge about  $\Delta t$  [s] discharge time in a respective GCPL experiment specific gravimetric and areal power densities,  $P_g$  [W/g] and  $P_A$  [ $\mu$ mW/cm<sup>2</sup>], were calculated as follows:

$$P_g = \frac{E_g}{\Delta t} \times 3600 \quad (3.7)$$

$$P_A = \frac{E_A}{\Delta t} \times 3600 \quad (3.8)$$

Equations 3.2 - 3.8 were adapted from Peng *et al.* [52].

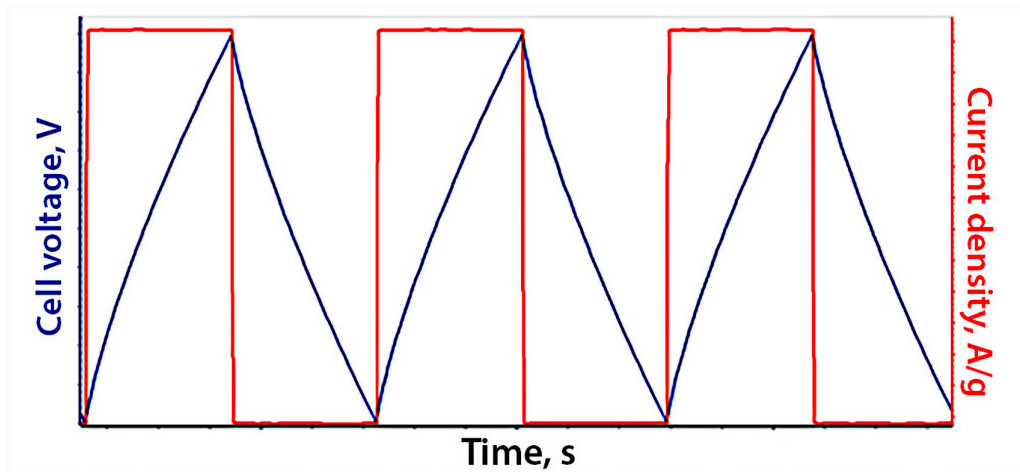


**Figure 3.15:** Experimental data recorded during Galvanostatic charge-discharge cycling with potential limitation



## 4. Results and Discussion

### 4.1 LIG Materials Characterization

#### 4.1.1 Morphology of LIG

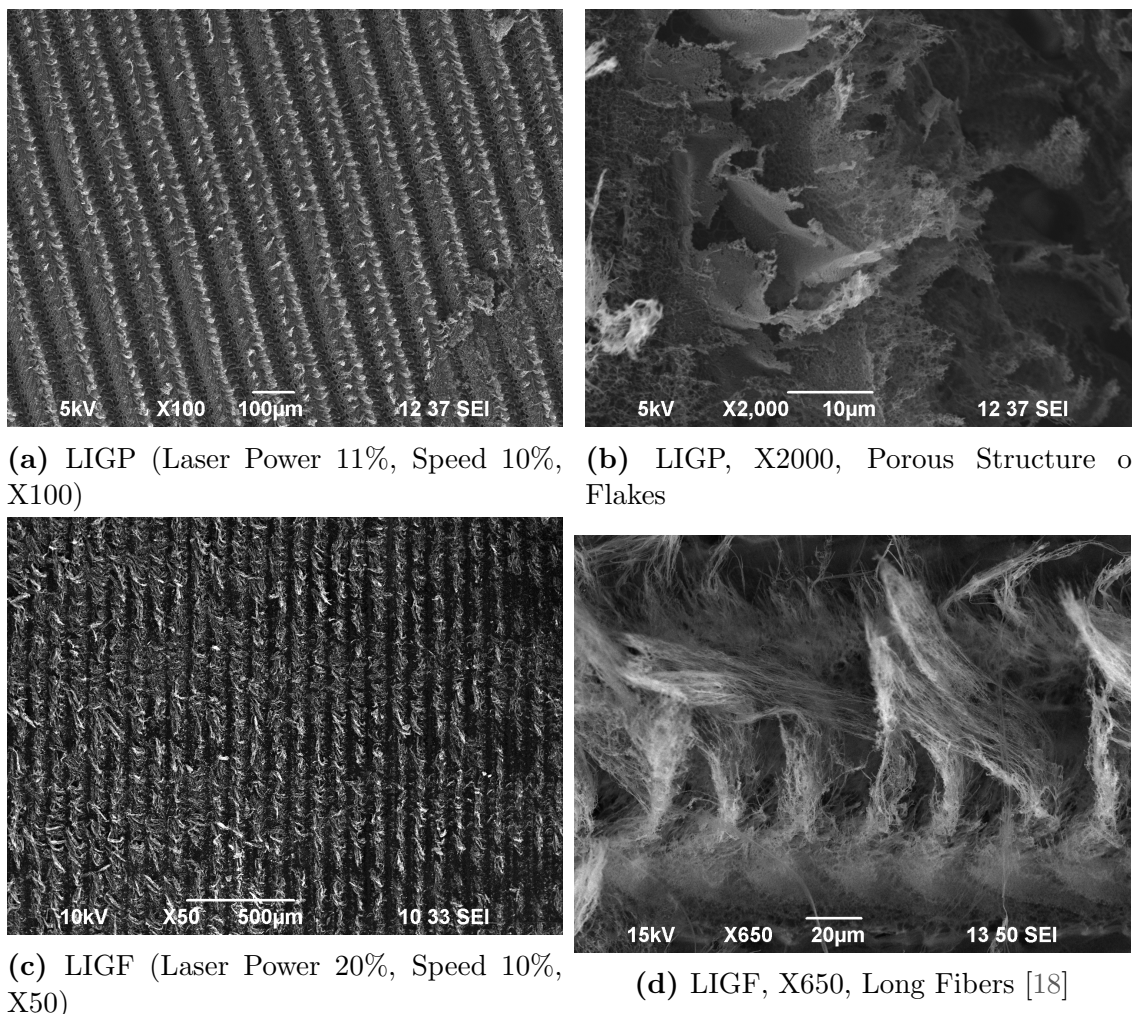


**Figure 4.1:** SEM images of LIG scribed on polyimide

As it was expected the two sets of laser scribing settings (see Table 3.1) yielded two types of LIG morphologies which can be described as porous (LIGP) and fibrous (LIGF). The SEM pictures reveal a two dimensional morphological anisotropy of airy networks formed by LIG. Figure 4.1a shows well defined lines of the newly formed material, which are parallel to the original laser scanning direction.

The SEM images of LIGP, which were obtained with the laser power of 20%, and the rastering speed of 10%, can be seen in Figures 4.1a and 4.1b. The flake rich lines alternate with the ditches where less of the flakes can be seen. In particularly Figure 4.1b allows to observe the highly porous webbing of the obtained material.

Higher fluence settings (Power 20%, Speed 10%) of laser scribing yields the LIGF

which consists of a porous part at the bottom and a fibrous region at the top of the treated area as in Figure 4.1d. It can be seen that the fibers have an approximate length of a few hundred  $\mu\text{m}$  and are laid along the scribed lines (Figure 4.1d was kindly provided by Hana Hampel from LAMPSe group [18]).

#### 4.1.2 Morphology of Conductive Elastic Biocomposites Based on LIG

The LIG-PDMS-8:1 composite was obtained by spin coating as described in the Experimental Section 3. The LIG patterns were embedded into PDMS and subsequently peeled off of the original polyimide substrate, which means the originally unseen bottom part of the LIG became the new interface of the composite device. It is worth mentioning that the peeling off process was drastically improved if beforehand the specimen were submerged into ethylacetate for 5-10 minutes. In some cases the films would then come off themselves without additional pulling force needed. This fact helped to keep the interface area undamaged. It also helped to ensure that virtually all the LIG was transferred to the LIG-PDMS composite. The interface on the peeled off side was investigated with a help of a light microscope to see if the LIG was fully merged into the PDMS matrix. It was found that the alternating line pattern of LIGF and LIGP stays preserved after the transfer and that the surface can sustain light scratching without any LIG particles being detached from the surface.

For the SEM some of the previously mentioned supercapacitor electrodes with VIAs contacts were used, as they came in very useful for avoiding the overcharging effects while imaging. As one sees it in Figure 4.2 the composite is mainly conductive with solitary islands of non-conductive PDMS (bright spots), evidenced by charging during imaging with the electron beam. Although the specimen in this picture was produced from LIGF, no fibers can be seen as all of them are embedded into the bulk of the composite leaving the macroporous interface areas at the top surface.

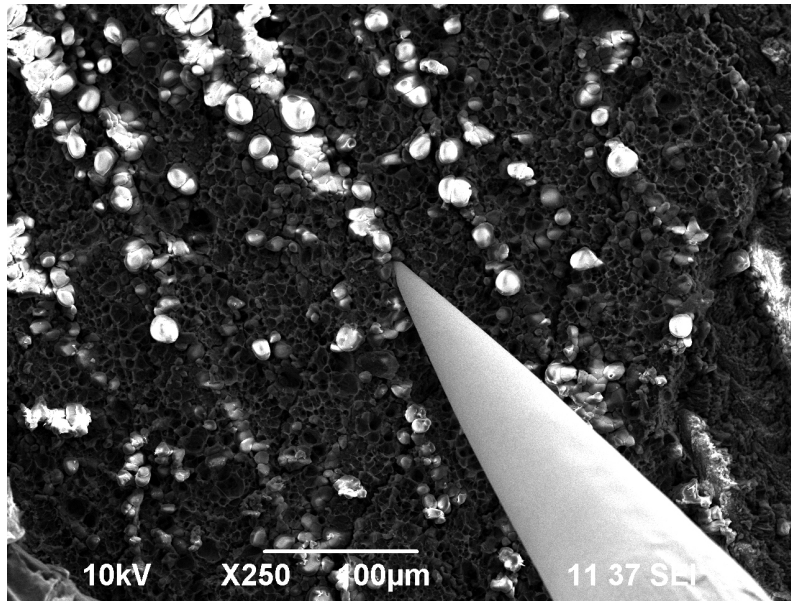


**Figure 4.2:** SEM image of LIGF layer embedded into PDMS and peeled off from the original PI substrate. The metal tip seen in the picture was used to discharge the surface

Morphology of LIGP and LIGF transferred to MPU was investigated earlier in LAMPSe group by A. Dallinger [21]. We present these results in this section to round off the picture of morphological investigations for the relevant conductive elastic bio-composites. Figures 4.3 (a) and (b) show LIGP and LIGF on PI before the transfer to MPU. LIGF has cone bundles of fibers with an average diameter of 50-70 nm and a length of 100-200  $\mu m$ . When the LIG is transferred to MPU, the morphology of the surface changes because the layers which initially used to be the bottom part of the LIG become exposed at the top of the laminated MPU. As it can be seen in Figure 4.3(d) the new top-surface of LIGP on MPU features large pores; the fiber cones of LIGF in turn are not completely destroyed preserving an interconnected network of fiber bundles (Figures 4.3(f), (g)). Figures 4.3(e), (h) were taken at the edge of the LIG pattern transferred onto MPU to see the depth of LIG penetration into the adhesive layer. As it can be seen LIGP and LIGF is not completely submerged, which leaves a part of the LIG surface available *e.g.* for future electric-storage applications.

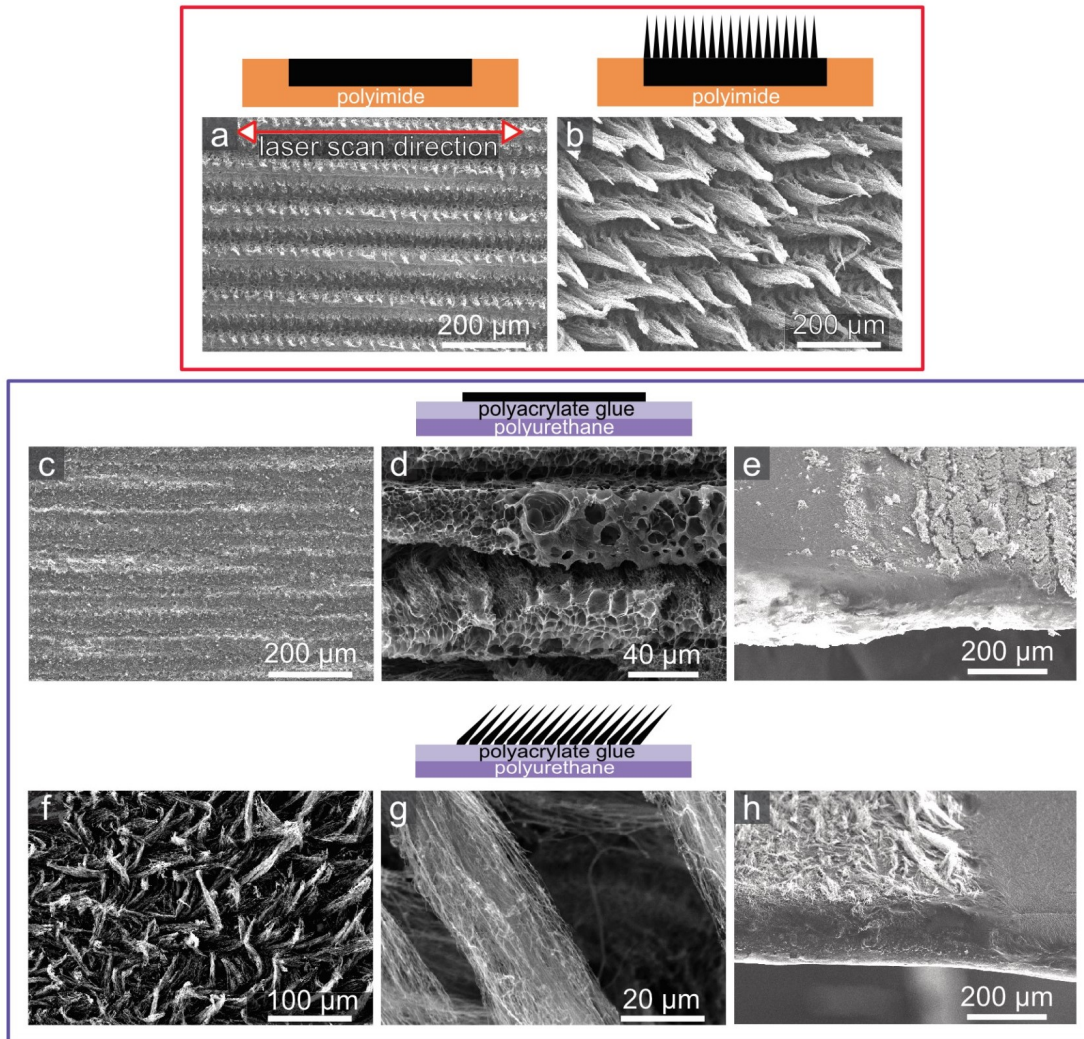


**Figure 4.3:** Schematics of the LIG-MPU samples and SEM images of LIG on PI (top panel) and LIG-MPU (bottom panel): (a) LIGP and (b) LIGF on PI; (c, d) morphology and (e) cross-section of LIGP-MPU; (f, g) morphology and (h) cross-section of LIGF-MPU. All SEM images are top view (sample tilt angle  $\Theta = 0^\circ$ ), except for e, h which are tilted views ( $\Theta = 50^\circ$ ) [21]

### 4.1.3 Areal mass loading of LIGs

The summary of the obtained mass density values of LIGs supported by various substrates can be seen in the following Table 4.1.

**Table 4.1:** Mass per Surface Area of LIGs on Various Substrates

LIG Type	Substrate Material	Areal mass loading [ $mg/cm^2$ ]
LIGP	Kapton <sup>TM</sup> Film/Tape 50 $\mu m$	$0.20 \pm 0.01$
LIGF	Kapton <sup>TM</sup> Film/Tape 50 $\mu m$	$0.51 \pm 0.04$
LIGP	PDMS-8:1	$0.20 \pm 0.01$
LIGF	PDMS-8:1	$0.51 \pm 0.04$
LIGP	MPU	$0.11 \pm 0.01$
LIGF	MPU	$0.28 \pm 0.06$

### 4.1.4 Thickness Measurements

The thickness of commercially available Kapton<sup>TM</sup> film and tape was measured by profilometry and was estimated to be  $50 \pm 0.5 \mu m$ , which was in compliance with the tolerance values claimed by the manufacturer.

The thickness of LIG-PDMS-8:1 composites was estimated by observation of cross section with optical microscope, as described in Experimental Section 3. As one can see in the following Figure 4.4a the thickness of the blank double-layered PDMS-8:1 was found to be  $\approx 70 - 80 \mu m$ . Bare PDMS layer was sufficiently thinner than the LIGP/LIGF-composite part which varied from  $180 \pm 35$  for PDMS-LIGP to  $400 \pm 35$  for PDMS-LIGF. In Figure 4.4b the fully embedded long fibers of LIGF can be seen.

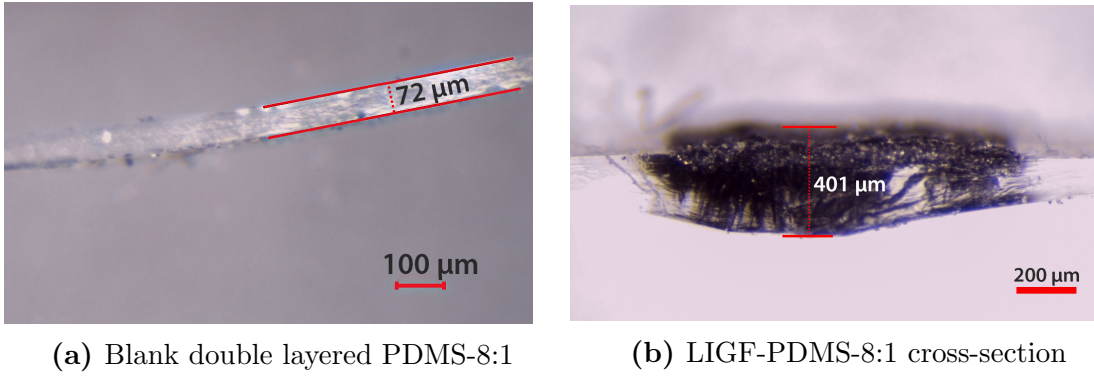


**Figure 4.4:** Thickness evaluation of LIGF-PDMS-8:1 composite

The results of the thickness measurements are given in Table 4.2.

**Table 4.2:** Thickness of LIG-PDMS composites

Material	Thickness [ $\mu m$ ]
PDMS-8:1-one layer	$45 \pm 10$
PDMS-8:1-double layer	$75 \pm 5$
LIGP-PDMS-8:1-one layer	$180 \pm 35$
LIGP-PDMS-8:1-double layer	$210 \pm 30$
LIGF-PDMS-8:1-one layer	$365 \pm 40$
LIGF-PDMS-8:1-double layer	$400 \pm 35$

#### 4.1.5 Sheet Resistance of LIG and LIG-PDMS composites

The sheet resistance was calculated via Equation 2.16 with the correction factor  $C_f = 0.9$ . The results calculated by David Graphinger, are presented in the following Table 4.3. As was previously described in the Experimental Section 3 the four probes sheet resistance tests were performed in three variants. Namely, the probe was put in contact with the sample either parallel to the original lasering direction, or perpendicular, or by  $45^\circ$  angle to it. It was found that the best conductivity is achieved for the probe being parallel to the LIG stripes.

**Table 4.3:** Sheet resistance of LIGF in PDMS depending on the probe and the lasering direction alignment [22]

Alignment	$R_{sq}$ [ $\Omega/sq$ ]
90 °	119 ± 36
parallel °	91 ± 31
45 °	96 ± 23

## 4.1.6 Electromechanical Characterization of Composites

### LIG-PDMS composites

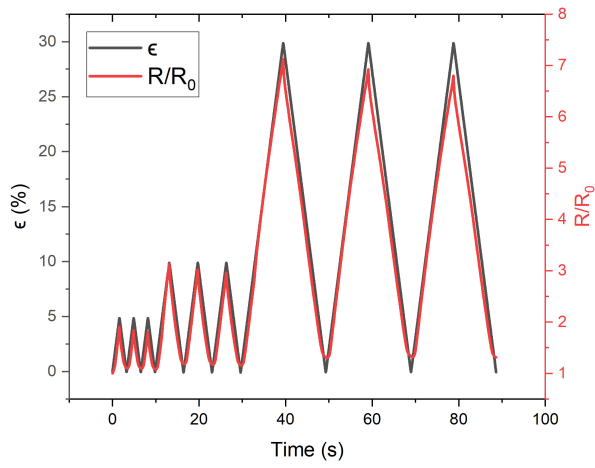
The samples of LIG-PDMS composites as listed in the Table 3.4 have undergone the electromechanical tests under varying humidity.

At first mechanical behaviour of these samples was analysed for ambient humidity. The stress to strain and resistance to strain dependencies of LIGP-||-PDMS, representative for all other samples of this family, are shown in Figure 4.5. It can be seen that all types of the LIG-PDMS composites retain the elastic behaviour typical to the blank PDMS material at least up to 30% of strain. The resistance linearly increases upon the strain; it was found that the samples stay conductive also at the larger strains showing normalized  $R/R_0$  values of 8-15 at 30% of strain.

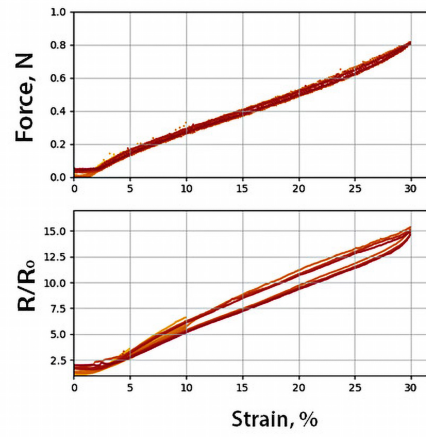
Further the effect of humidity in respect to resistance of the samples was analysed.

As was mentioned in the Section 3 the specimen with the parallel (denoted LIGP|| and LIGF||) and perpendicular (LIGP⊥ and LIGF⊥) direction of scribed LIG lines in respect to the stretching direction were investigated. Figure 4.6a demonstrates the that the resistance of the LIGP|| and LIGF|| patterns increases in more humid environment. On the other hand neither blank PDMS nor the LIGP⊥ or LIGF⊥ have shown noticeable change in resistance upon the changes in ambient humidity.

For each type of samples the Young's Modulus  $E$  [MPa] was calculated at 45%, 65% and 92% RH. The results can be found in the Table 4.4. The Figure 4.6b demonstrates the negative trend for Young's Modulus of LIGP-composites with the raise of humidity rate. The latter effect could be attributed to the hydrophilic properties of LIGP which was earlier demonstrated in the Bachelor Thesis of Matthias Gritzner [53]. However, better understanding both effects needs a deeper investigation in the future to address material properties to the structure of the composites.



(a) Tensile Test Procedure

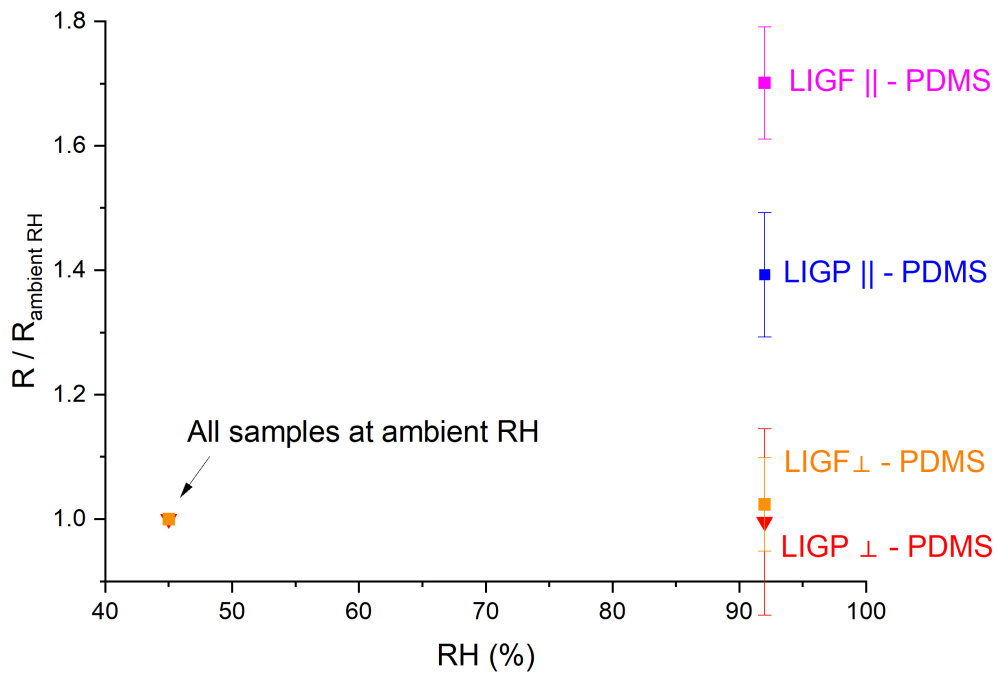


(b) Stress and resistance to strain behavior up to 30% of strain

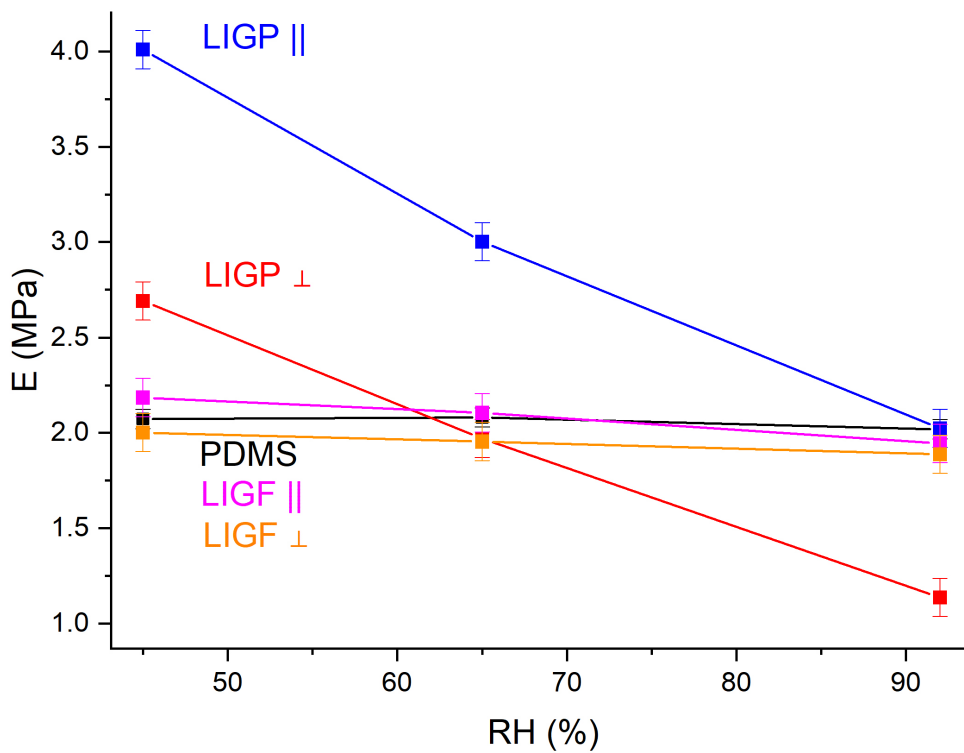
**Figure 4.5:** Tensile test of LIGP||-PDMS

**Table 4.4:** Young's Modulus for LIG-PDMS samples at various %RH

Sample	E [MPa] at 45%	E [MPa] at 65%	E [MPa] at 95%
PDMS	$2.0 \pm 0.1$	$2.1 \pm 0.1$	$2.0 \pm 0.1$
LIGP-  -PDMS	$4.1 \pm 0.15$	$3.0 \pm 0.1$	$2.0 \pm 0.1$
LIGP-⊥-PDMS	$2.7 \pm 0.1$	$1.9 \pm 0.15$	$1.1 \pm 0.1$
LIGF-  -PDMS	$2.0 \pm 0.1$	$1.9 \pm 0.1$	$1.9 \pm 0.1$
LIGF-⊥-PDMS	$2.2 \pm 0.1$	$2.1 \pm 0.1$	$1.9 \pm 0.1$



(a) Normalized R vs RH



(b) Young's Modulus vs RH

**Figure 4.6:** Dependencies of resistance and Young's Modulus of LIG-PDMS samples on humidity

### LIG-MPU composites

In the same way as for LIG-PDMS composites the laminates of LIG on MPU were tested under tensile strain up to 30%. The stress to strain and resistance to strain dependencies of LIGP-||-MPU, representative for all other samples of this family, are shown in Figure 4.7. Regardless of whether or not MPU was laminated with LIG, all samples demonstrated viscoelastic behavior, which can be attributed to the overall known viscoelasticity of the utilized MPU [51]. In contrast to linear electromechanical behaviour of LIG-PDMS composites, the LIG-MPU laminates show significant hysteresis in R vs. strain diagrams and rather non-linear dependency of resistance *vs.* strain which can be attributed to the viscoelastic properties of the MPU as well as to the low density of LIG on the adhesive surface, which leads to rearrangement of the percolation pattern during the tensile tests.

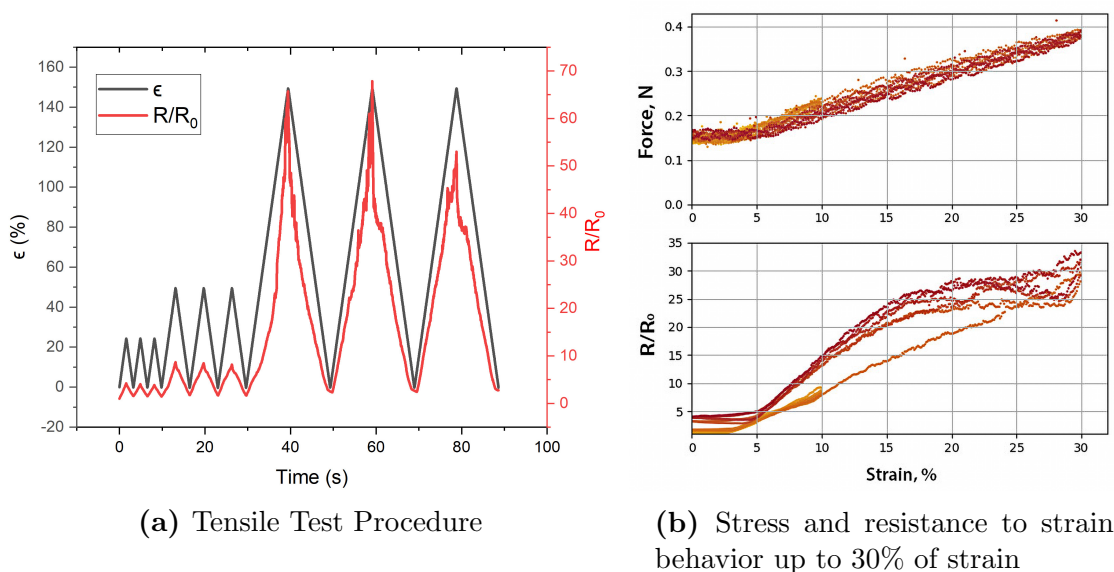


**Figure 4.7:** Tensile test of LIGP-||-MPU

By means of an optical microscope it could be seen that the MPU material swells in the humid conditions which could be the reason for the change its mechanical properties. Further the Young’s Modulus was calculated from the stress to strain data (for  $\epsilon$  of 10%); the E was estimated to be  $\approx 8.3$  MPa at the RH of 45% and  $\approx 5.8$  MPa at the RH of 92% for all laminates and the blank MPU film. In conjunction to the change in mechanical properties the dependency of resistance *vs.* humidity was investigated. The samples were pre-strained to 30% at the ambient RH of 45% and left for a few seconds, during this time the relaxation of R and stress could be observed (Figures 4.8 and 4.9). Then, humidity was increased up to 92%. At this stage resistance of LIGP-MPU has shown much more noticeable increase as compared to the LIGF-MPU. After some time the humidity was decreased to the original value: it could be observed that the resistance of LIGP-MPU had decreased accordingly. The described effects could be again attributed to the hydrophilic properties of LIGs, however more tests are needed to get a better understanding of the dependencies.

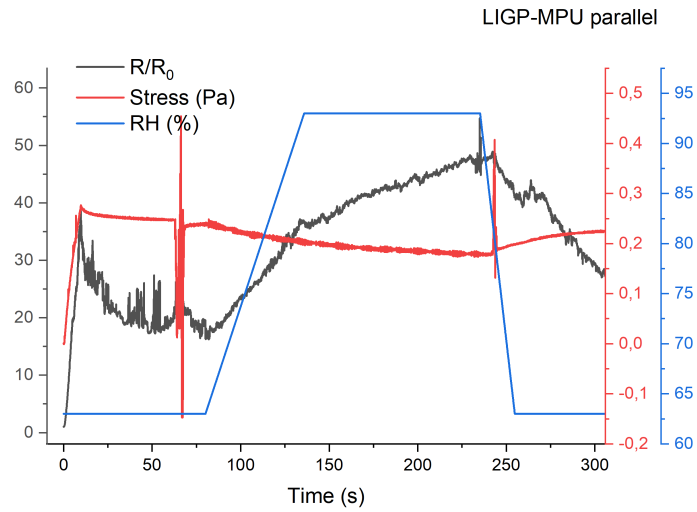


**Figure 4.8:** LIGP-MPU: Normalized resistance, relative humidity, stress at constant strain of 30%

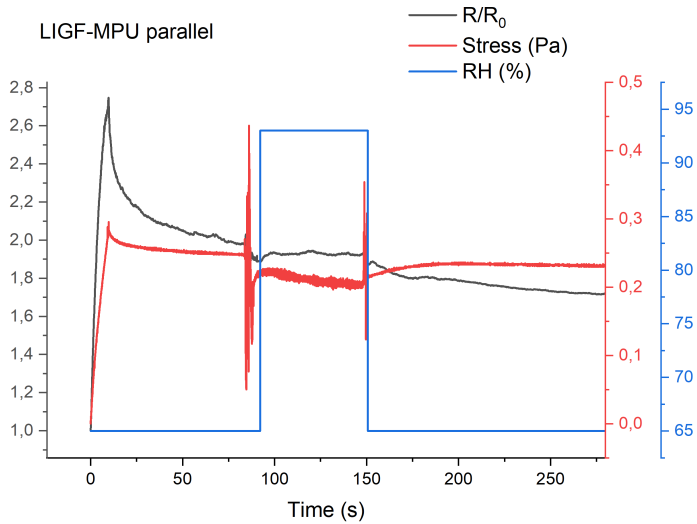


**Figure 4.9:** LIGF-MPU: Normalized resistance, relative humidity, stress at constant strain of 30%

The main conclusion relevant to this work is that the LIG laminates on the MPU do not demonstrate linear electrical behaviour upon strain regardless of a humidity change.

## 4.2 Surface Area and Porosity Characterization

### 4.2.1 Gas Adsorption Measurements (BET) for Powder LIGs

The surface area and porosity values obtained for LIGP and LIGF powders via adsorption isotherms are shown in the Table 4.5. For the LIGF material the results of the sample LIGF (2) were taken as the final value because its adsorption isotherm was obtained for the full range of relative pressure, as will be described later in this subsection.

**Table 4.5:** Powder BET Measurements Results

LIG Sample	$C_{BET}$ [a.u.]	$n_m$ [ $cm^3/g$ ]	$A_{BET}$ [ $m^2/g$ ]	TPV [ $cm^3/g$ ]	TPSA <sup>1</sup> [ $m^2/g$ ]
LIGP	488.9	44.01	192	0.26215	98.9
LIGF (2)	15.8	62.15	270	0.38820	146.4

Figures 4.10 and 4.12 represent the adsorption and desorption isotherms for LIGP and LIGF. The isotherms correspond to the Type II by the IUPAC classification. No significant hysteresis can be seen for the both types of LIG, which indicates an absence of mesoporosity in the bulk. As it can be seen in the Figures 4.11 and 4.13 the slope value of the linear part of the isotherm  $s$  is lower for the LIGF material which leads to a significantly lower value of  $C_{BET}$  in BET analysis.

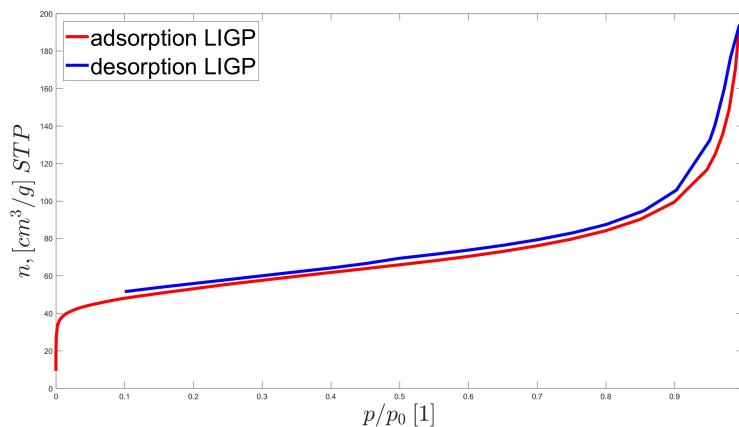


**Figure 4.10:** LIGP adsorption/desorption Isotherm

---

<sup>1</sup>TPSA - Total pore surface area

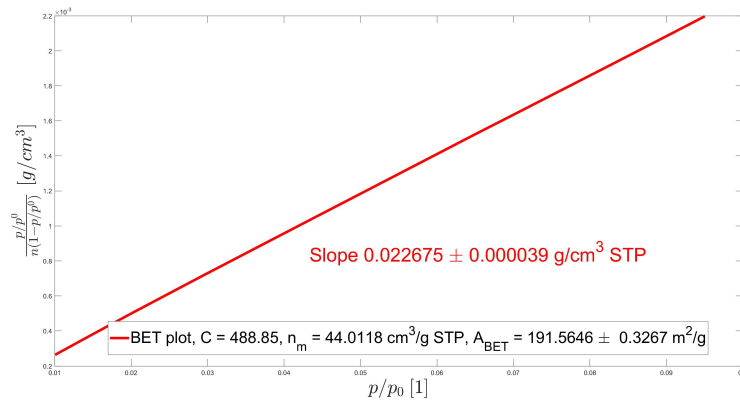


**Figure 4.11:** Linear BET plot for  $p/p_0$  0.01 to 0.1 for LIGP

As mentioned in Section 2, the BET method can be applied to Type II and Type IV isotherms, but extreme caution is needed in the presence of micropores (i.e. with Type I isotherms and combinations of Types I and II or Types I and IV isotherms) [54]. The pore size and pore volume evaluations were performed via  $N_2$  at 77K on Carbon Slit Pores by NLDFT model [55] and have shown the investigated LIG materials were strictly microporous as presented by the differential pore volume distributions in Figure 4.14. As can be seen from the graphs, the porosity of the LIGP can be accounted to the micropores ranging from 7 to 15 Å in size, while the bulk of the LIGF is mostly occupied by the pores from 13 to 31 Å in diameter.

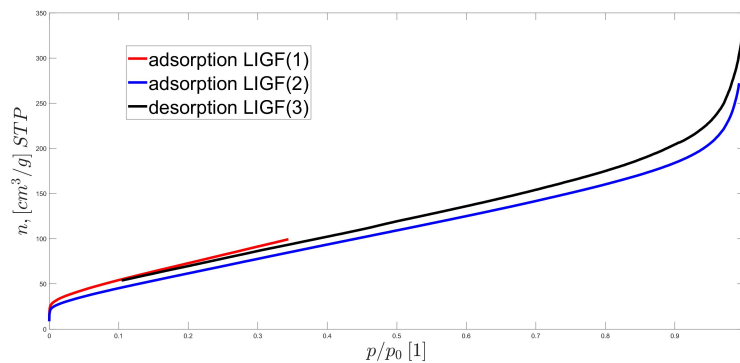


**Figure 4.12:** LIGF adsorption/desorption Isotherm

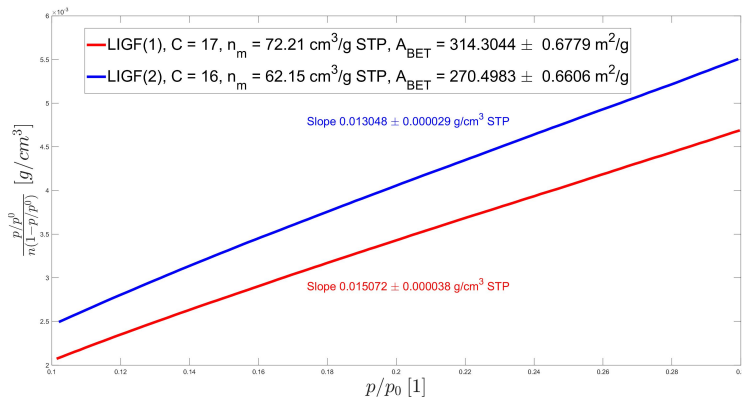


**Figure 4.13:** Linear BET plot for  $p/p^0$  0.1 to 0.3 for LIGF

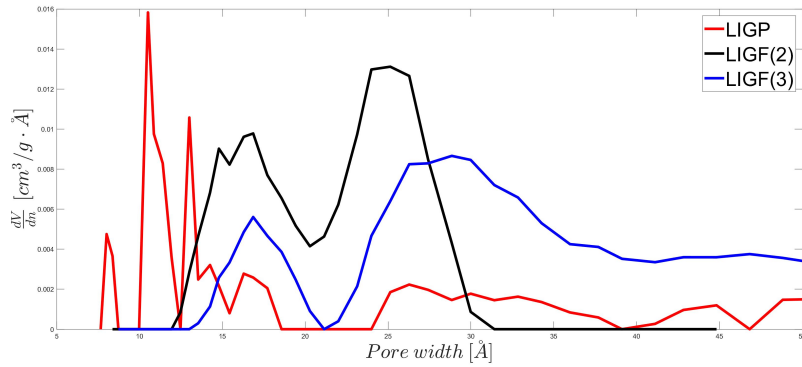


**Figure 4.14:** Differential pore size distributions for LIGP and LIGF

Further as visually shown in Figure 4.15, the total pore volume (TPV), as well as the total pore surface area (TPSA), per unit mass is 48% larger in the LIGF than in the LIGP.

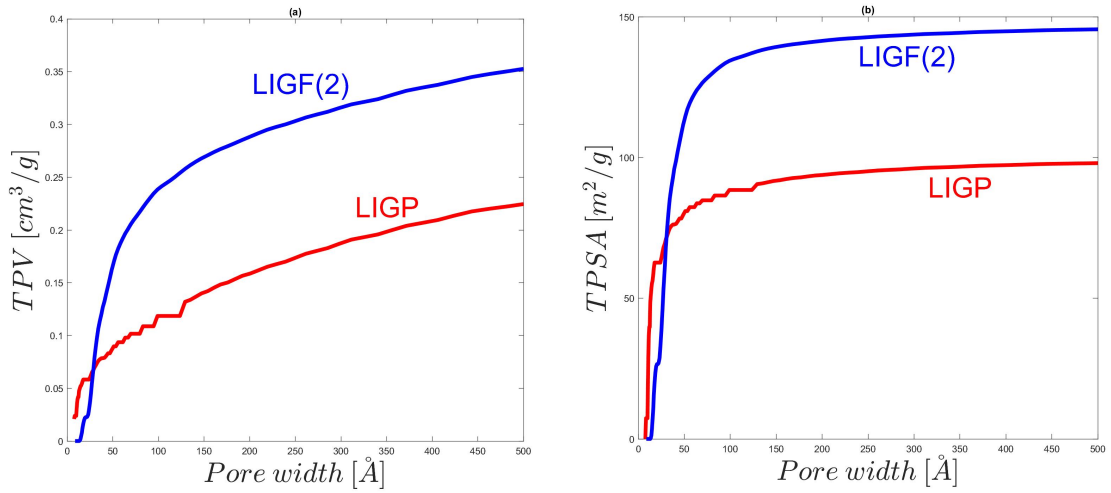


**Figure 4.15:** Cumulative Pore volume (a) and Surface area (b) vs. Pore width for LIGP and LIGF(2)

Comparing our results to the results of Lin *et al.* [1] described in Section 2 allows a conclusion that the LIG materials investigated here belong to microporous bulk type, with much smaller pores than in [1]. The values of the BET specific surface area obtained in this study are lower than those provided by Lin *et al.* ( $\sim 342 \text{m}^2/\text{g}$ ), but belong to the range of  $200 \sim 350 \text{m}^2/\text{g}$ .

## 4.2.2 Morphology of LIG via Gemini<sup>TM</sup> Technique and AFM

Surface area of LIG samples formed on the different substrates was investigated also with Gemini and AFM measurements by Dr. Francesca Borghi at the University of Milano. The values of specific surface area  $A_{Gemini}$ ,  $A_{AFM}$  are reported in Table 4.6. The porous structures formed on Kapton<sup>TM</sup> Film and on Kapton<sup>TM</sup> Tape were characterized by the highest surface area, while fiber structures exhibit the lowest surface area. Here a note concerning the LIGF results has to be made. Fibrous LIG structures have a weak attachment to the PI substrate. When these samples were put into Gemini chamber, the chamber was degassed, which lead to a certain unmeasured loss of materials from fiber structures formed on Kapton<sup>TM</sup> Film. This circumstance could have decreased the real quantity of fiber mass during measurements, and thus the specific surface area estimated value.

**Table 4.6:** Morphological properties of LIG samples

Sample	$A_{Gemini} [m^2/g]$	$A_{AFM} [m^2/g]$
LIGF KAPTON FILM	$61 \pm 9$	$2.03 \pm 0.24$
LIGF KAPTON TAPE	$50 \pm 5$	-
LIGF (KAPTON FILM) PDMS	$14 \pm 2$	-
LIGF (KAPTON TAPE) PDMS	$32 \pm 4$	$1.45 \pm 0.46$
LIGP KAPTON FILM	$126 \pm 11$	$1.72 \pm 0.28$
LIGP KAPTON TAPE	$113 \pm 18$	-
LIGP (KAPTON FILM) PDMS	$15 \pm 3$	$1.42 \pm 0.31$
LIGP PEEK	$71 \pm 20$	-

Table 4.6 presents the results obtain via Gemini and AFM techniques. It can be seen that AFM results suggests LIGF-PI having the largest specific area among all tested samples. This fact can be attributed to high roughness values of LIGF as compared to LIGP surfaces.

In Figure 4.16 the corresponding nitrogen adsorption isotherms are shown. The structural properties of both LIGP and LIGF samples are determined by the substrate from which they form. The specific surface area, as also the maximum amount

of gas adsorbed (which refers to the quantity of nitrogen adsorbed at relative pressure 0.99), depend on the substrate and cannot be attributed only to the porous or fibrous character of the LIG; amount of the material available for the adsorption varies depending on level of LIG penetration into the substrate. The results show that LIG-PDMS composite has significantly lower than LIG-PI specific surface area which can be attributed to the fact that part of the LIG embedded into the matrix is not available for the adsorption.

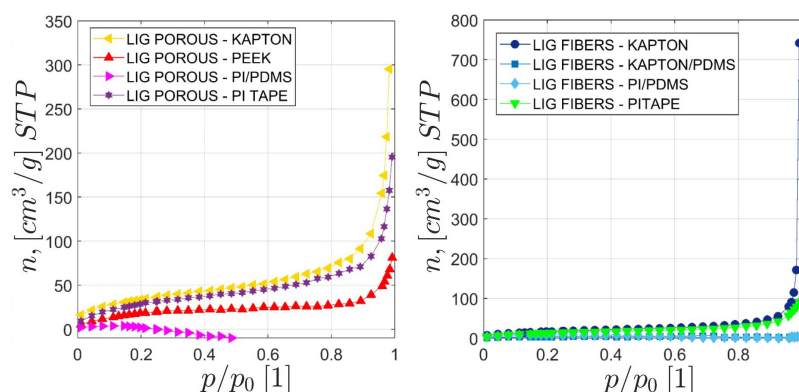


**Figure 4.16:** Gemini Nitrogen adsorption isotherms of LIGP samples (left) and LIGF samples (right).

This consideration is evidenced also by the AFM images shown in Figure 4.17: the shape of porous and fiber LIG samples is very similar if they are formed on the same substrate. The morphology at different scales of the LIG formed on Kapton Film and PDMS is shown in the AFM morphological map Figure 4.18.

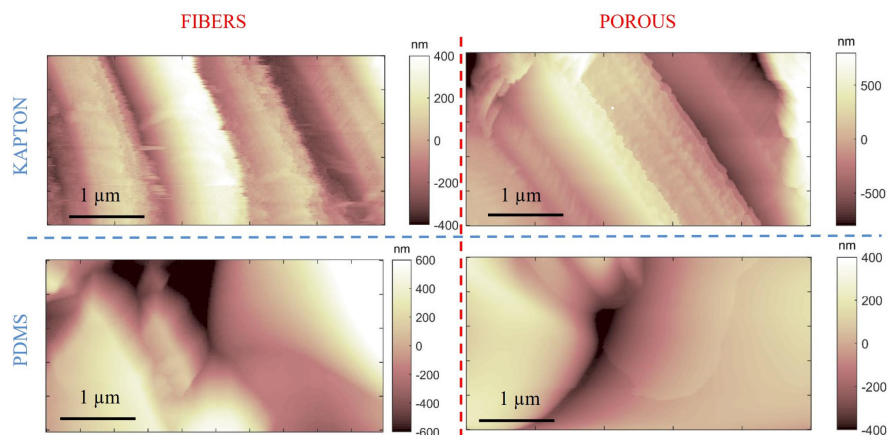


**Figure 4.17:** AFM topographical images of LIGF and LIGP on Kapton and on PDMS.

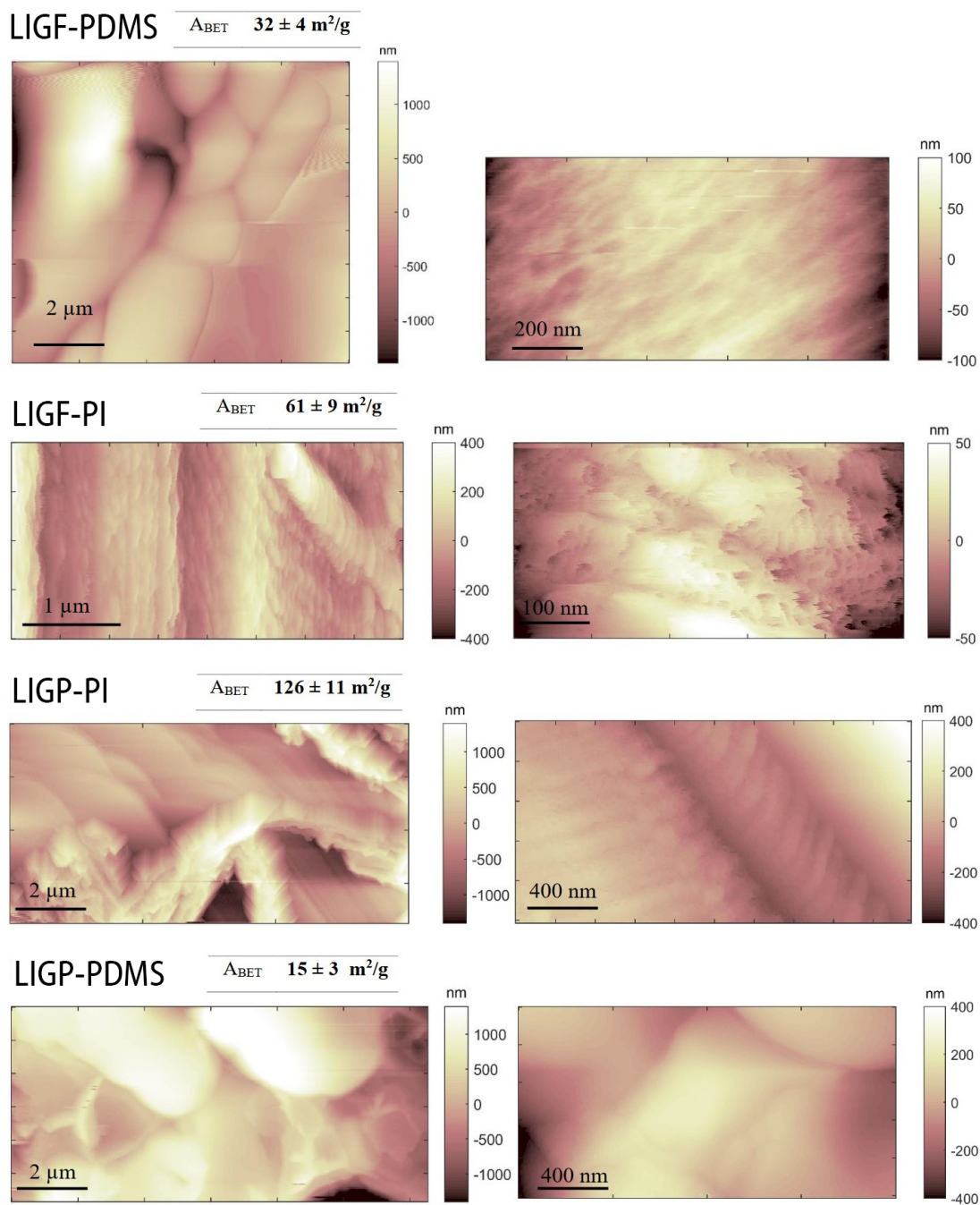


**Figure 4.18:** Morphology at different scales of LIGF and LIGP on Kapton and PDMS

The difference in specific surface area of LIGP and LIGF formed on the same substrate could be due to the fine morphology which characterized the samples. A comparison between nitrogen adsorption isotherms acquired on porous and fiber formed on Kapton film is shown in Figure 4.19.

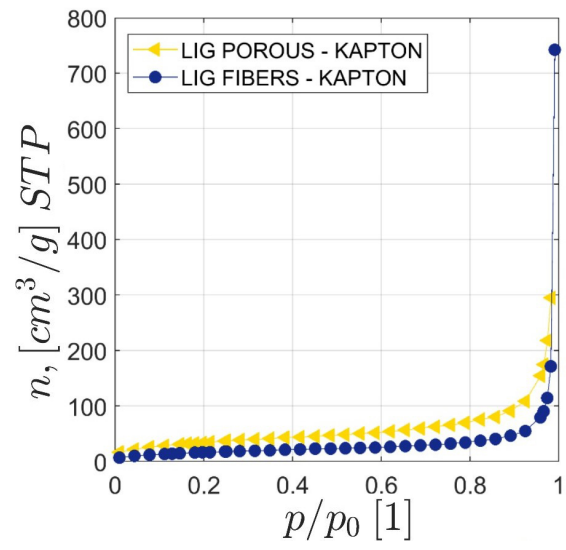


**Figure 4.19:** Nitrogen adsorption isotherms of LIGF and LIGP on Kapton Film.

### 4.3 LIG Based Supercapacitors

The Table 3.8 in 3 summarizes the list of the LIG based electrodes prepared for the subsequent electrochemical analysis.

### 4.4 Electrochemical Characterization of Swagelok Supercapacitor Cells

#### S0P: LIGP on Kapton Electrodes in a Swagelok Cell

The CV and GCPL tests were conducted with the round electrodes supplied by VIAs contacts, which were prepared according to the description provided in the Experimental Setup Section.

Two Swagelok cells of type S0P (See Table 3.8 above) were tested one after another. At first the CV run was initiated for 0 - 0.2 V window. It was pre-programmed to consist of 10 cycles per each of the consequently increasing scan rates of 5, 10, 20, 50, 100 and 200 mV/s. The resulting CV diagrams of current density vs potential are shown in the Figure 4.20.

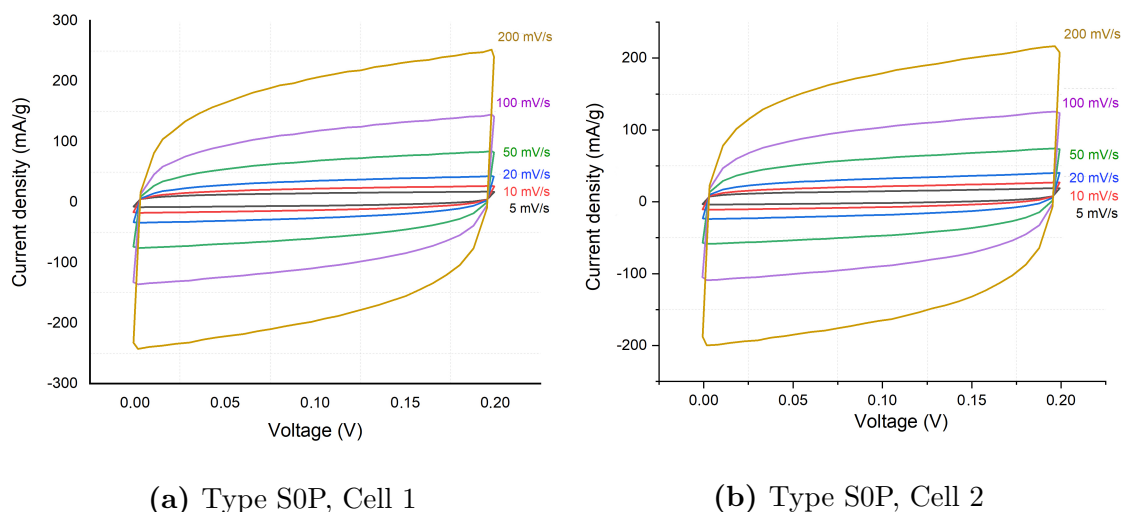


**Figure 4.20:** CV diagrams of S0P cells performed at 0 - 0.2 V potential window at different scan rates

After the CV sweeping the GCPL measurements were performed for the same voltage window, that is the  $V_{max}$  was set to 0.2 V for charging-discharging sets of 10 cycles at the currents of 0.04, 0.1, 0.2, 0.4 and 1 mA for each cycle type. Galvanostatic charge-discharge curves at different current densities as shown in the Figure 4.21 present nearly triangular shapes with minuscule voltage drop indicating negligible internal and contact resistances. For the future comparison with literature data current densities were calculated as  $I(V)/m$  [mA/g] and  $I(V)/s$  [ $\mu/cm^2$ ] and are given for the reference.

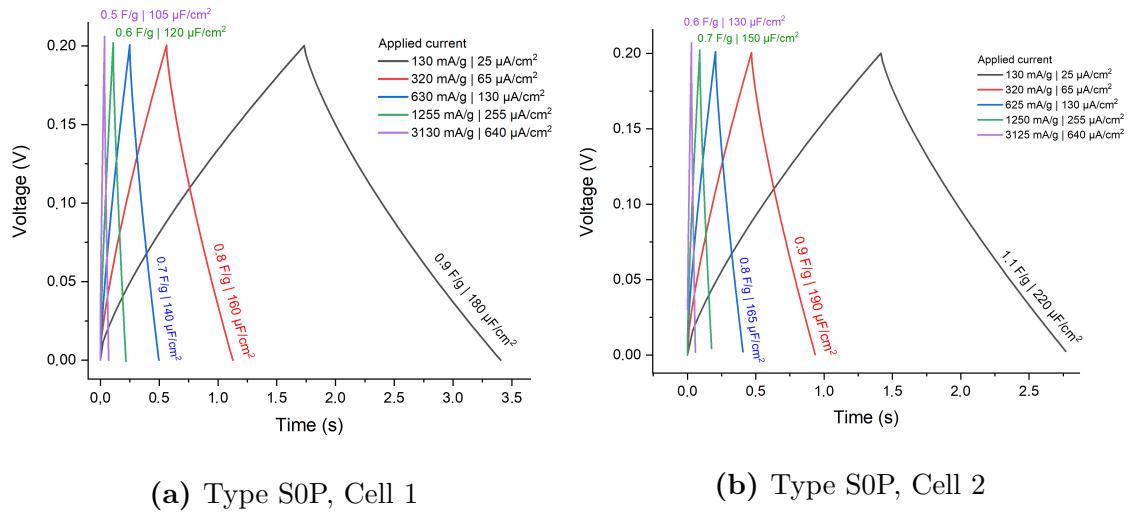


**Figure 4.21:** GCPL diagrams of S0P cells for  $V_{max}=0.2$  V at various current densities

Comparison of the GCPL curves at low vs. high applied currents showed a slightly increasing  $iR$  drop as a result of an increasing contact resistance of the electrodes. As can be seen from Figure 4.22  $iR$  changes from 6 mV at 130 mA/g to 35 mV at 3130 mA/g.

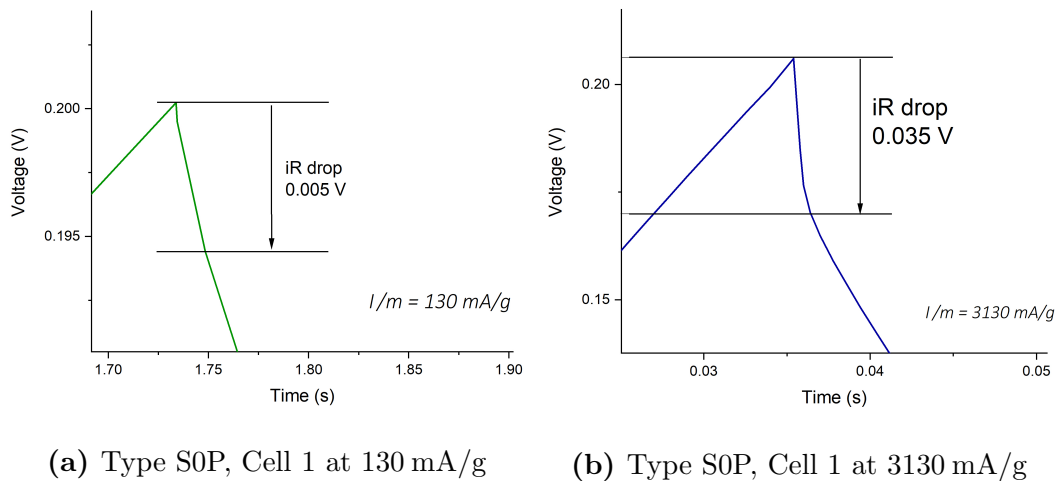
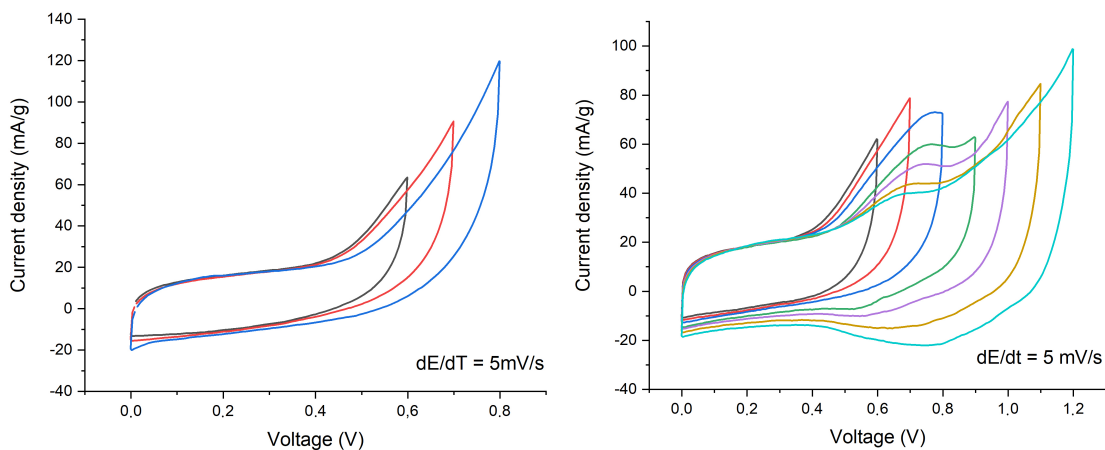


**Figure 4.22:** GCPL diagrams of S0P cells for  $V_{max}=0.2$  V at 130 mA/g and 3130 mA/g demonstrating the rise of  $iR$  drop with an increase of applied current

Further experiments included cyclic voltammetry for larger voltage windows at a constant scan rate of 5mV/s. The cell 1 could be tested for the ranges 0 - 0.6 V, 0 - 0.7 V and 0 - 0.8 V after which the experiment was stopped. The cell 2 was tested for the same potentials as well for the further 0 - 0.9, 0 - 1.0, 0 - 1.1 and 0 - 1.2 V sweeps. For both cells the shape of the CV curve increasingly deteriorated from the originally

seen rectangular shape as the voltage window had become wider. The respective cycling diagrams are shown in Figure 4.23. It can be observed that larger potential windows lead for the devices to undergo reversible chemical processes taking place in the cell.

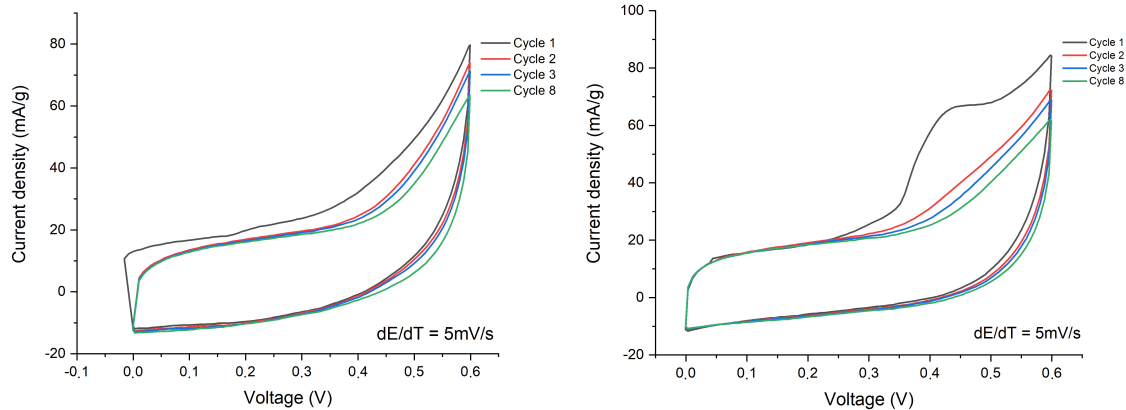


(a) LIGP-Kapton Electrodes, Cell 1

(b) Type S0P, Cell 2

**Figure 4.23:** CV diagrams of S0P cells for larger  $\Delta V$  windows at constant scan rate of 5 mV/s

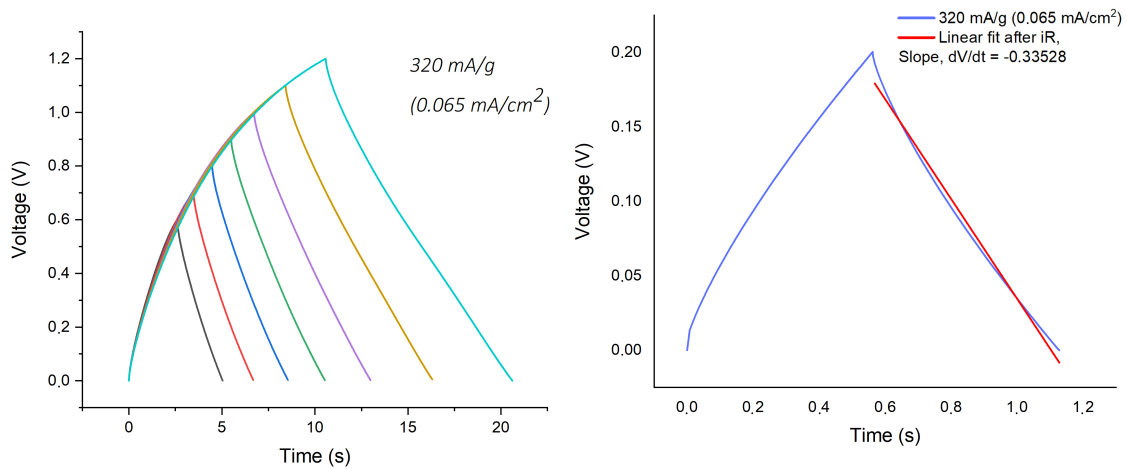
Additionally, for the cell 2 the very first CV cycle performed at the  $\Delta V = 0.6$  V showed a characteristic reduction peak on the positive sweep, which did not occur in the following cycles. This peculiarity can be attributed to a non-reversible chemical reaction quickly taking place on an electrode. The cell 1 in turn did not show this peculiarity as can be seen by comparing Figure 4.24a to Figure 4.24b:



(a) Type S0P, Cell 1. No peculiar peaks observed

(b) Type S0P, Cell 2. Characteristic Peak on the positive sweep at first cycle

**Figure 4.24:** CV diagrams of S0P cells for  $\Delta V = 0.6$  V at a constant scan rate of 5 mV/s



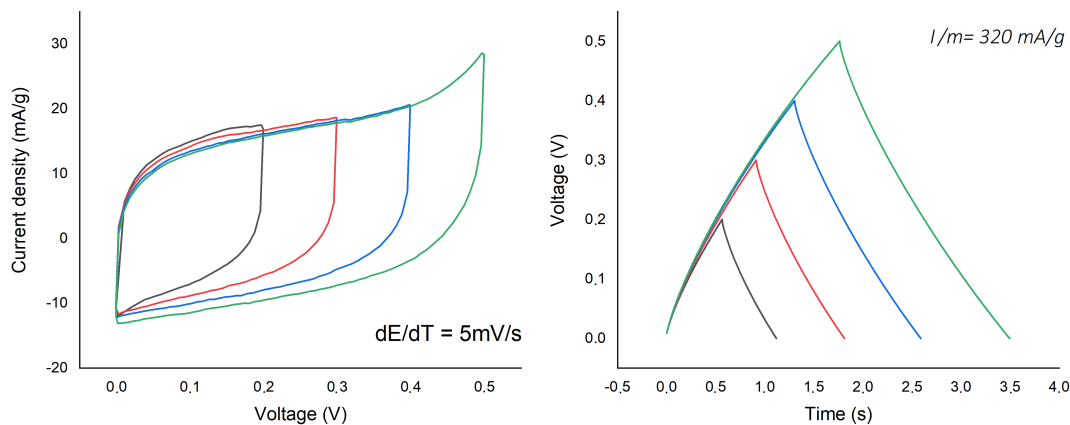
(a) Type S0P, Cell 2. GCPL runs at 320 mA/g for  $V_{max}$  up to 1.2 V

(b) Towards determination of the slope of a discharge branch of a GCPL curve for capacitance evaluation

**Figure 4.25:** CC diagrams of S0P cells

After each series of voltammetry cycles a set of galvanostatic cycles at repeatedly the same applied current of 320 mA/g was put into run. At higher voltages the triangular shape of the GCPL curves stayed satisfyingly similar to the lower voltages, showing the same slope of the discharge branches. This fact is consistent with Equation 3.2 and serves as an indication that the capacitance performance of the devices stayed constant independently of the  $V_{max}$  rise.

For the Cell 1 after tests with higher voltages, the next series of the CV measurements was performed at constant scan rate of 5 mV/s for lower potentials  $\Delta V$  set to 0.2, 0.3, 0.4 and 0.5 V. These cycles alternated with galvanostatic charge-discharge cycles taking place at 320 mA/g for  $V_{max}$  of 0.2, 0.3, 0.4 and 0.5 V.



(a) Type S0P, Cell 1. CV runs at 5 mV/s for  $\Delta V = 0.2 \div 0.5$  V

(b) Type S0P, Cell 1. CV runs at 320 mA/g for  $V_{max}$  up to 0.6 V

**Figure 4.26:** Constant rate CV and constant current GCPL middle range measurements

### Capacitance Evaluations for S0P Electrodes

In order to estimate the supercapacitor performance capacitance values were estimated as the main characteristic expressing the ability of a device to store electrical energy.

Since higher values showed an increasing level of distortion of the rectangular shape of the CV lines, so desirable for supercapacitors, the calculation of the capacitance values  $C_g$  and  $C_A$  was carried out for the results obtained with smaller voltage ranges up to  $\Delta V = 0.5$  V. The same approach was applied to the GCPL data. The slope value of a discharge GCPL branch was obtained by a linear fit to the respective curve part straight after the iR drop as shown in Figure 4.25b.

The capacitance values calculated with the CV data obtained in the constant voltage window 0 - 0.2 V at stepwise raised  $dV/dt$  (Figure 4.20) have shown a decrease with increasing scan rates. This effect can be attributed to diffusion effects taking place for the electrolyte ions, which have more time to penetrate the pores of the electrode material at the lower scan rates, while at higher scan rates the charges only manage to accumulate on the outer surface. Figure 4.27 shows the comparison of the calculated  $C_g$  [F/g] values for both tested S0P cells:

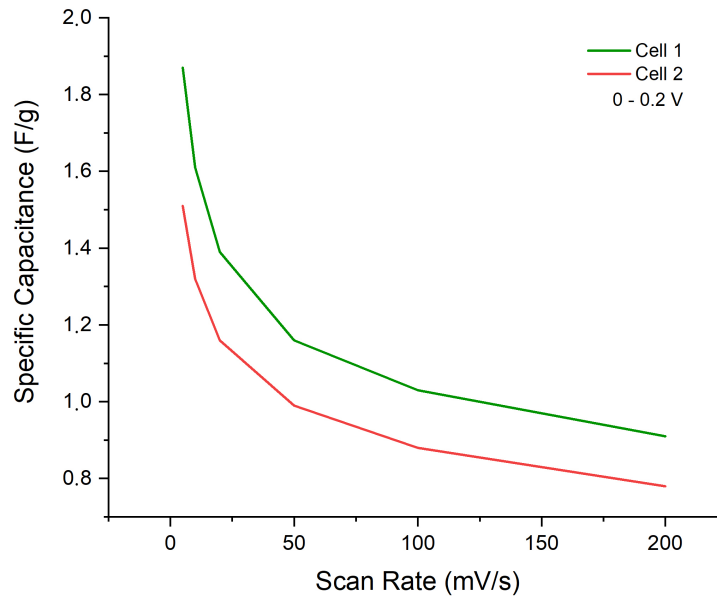
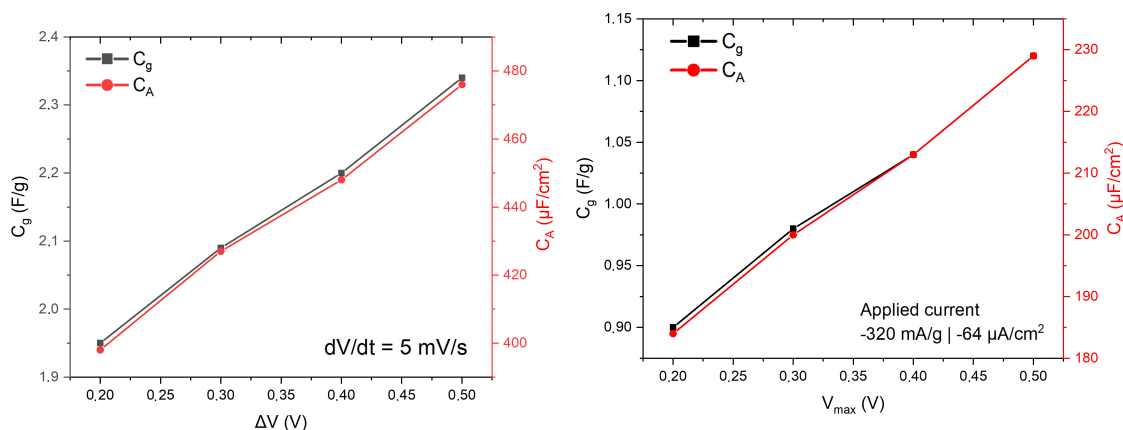


**Figure 4.27:** S0P specific gravimetric capacitance of Cell 1 and Cell 2 evaluated at CV voltage window of 0 - 0.2 V for increasing scan rates  $dV/dt$

Specific capacitance calculated from GCPL curves (Figure 4.21 ) as a function of current density have shown similar tendency, namely the estimated values decreased with an increase of the applied current for  $V_{max}$  staying constant at 0.2 V. In this case higher current density values mean faster charge-discharge cycle, which logically leads to the same effect hindering the charges to penetrate the bulk of the porous electrode to be stored at the deeper interface areas.

Capacitance evaluation for the CV experiments with constant scan rate but an increasing voltage sweep revealed that the  $C_g$  and  $C_A$  values rise proportionally to the rise of  $\Delta V$ . Similarly for GCPL data obtained for the applied current staying at 320 mA/g but with  $V_{max}$  increasing stepwise from 0.2 to 0.5 V it was found that the capacitance increases proportionally to  $V_{max}$  and therefore to the total time of a charge-discharge cycle:



(a) Type S0P, Cell 1. Increase of specific capacitance proportional to  $\Delta V$  increase at constant scan rate of 5 mV/s

(b) Type S0P, Cell 1. Increase of specific capacitance proportional to  $V_{max}$  increase at constant current of 320 mA/s

**Figure 4.28:** Specific Capacitance of LIGP-Kapton electrode evaluated with CV and GCPL data

## S0F: LIGF on Kapton Electrodes in a Swagelok Cell

The next variation of electrode to be tested was LIGF on Kapton (Type S0F in the Table 3.8 above). Two Swagelok cells with 1M  $\text{NaNO}_3$  as an electrolyte were prepared. However the Cell 1 had shown poor performance already in the preliminary CV runs which indicated too high inner resistance, probably due to a failure of the VIA contacts, and so it was not tested in the following electrochemical experiments.

For Cell 2, the first stage of measurements was carried out according to protocols similar to those used for the S0P described earlier. Figure 4.29a presents nearly perfect rectangular shape of the resulting CV curves at a constant voltage window at 0 - 0.2 for stepwise increased scan rate. However as it can be seen from this Figure the current densities that were achieved were about an order of magnitude smaller than for S0P. After the cyclic voltammetry the GCPL runs for different charge-discharge currents from 100 to 2000 mA/g were performed for the  $V_{max}$  fixed at 0.2 V, as shown in Figure 4.29b:

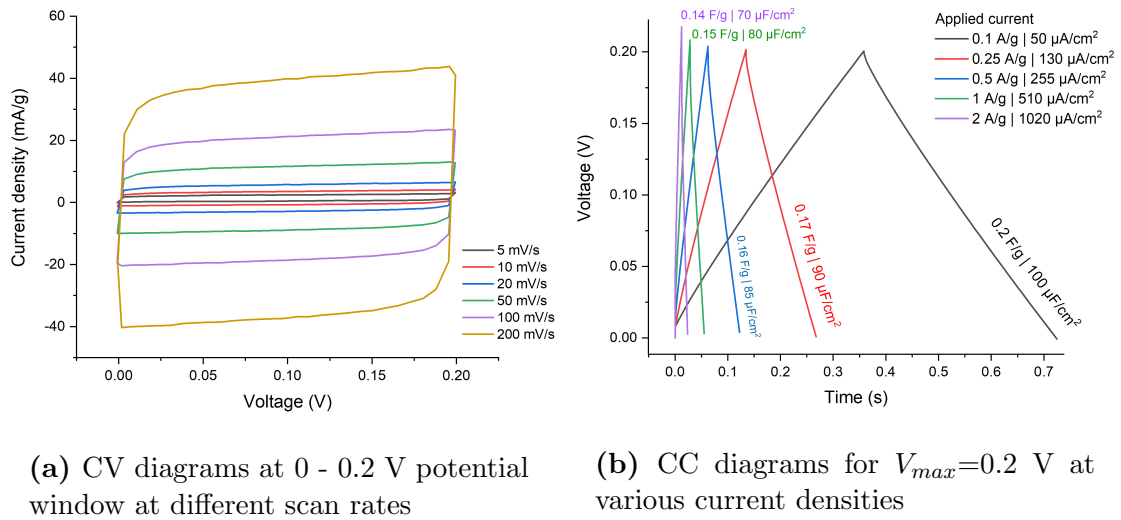


**Figure 4.29:** Type S0F, Cell 2. CV and GCPL data in the low voltage range 0 - 0.2 V

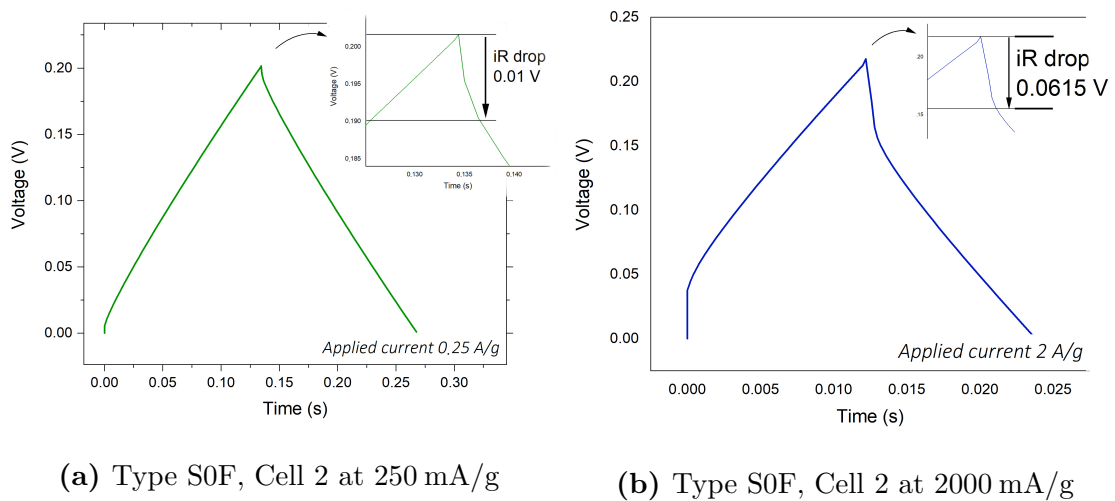
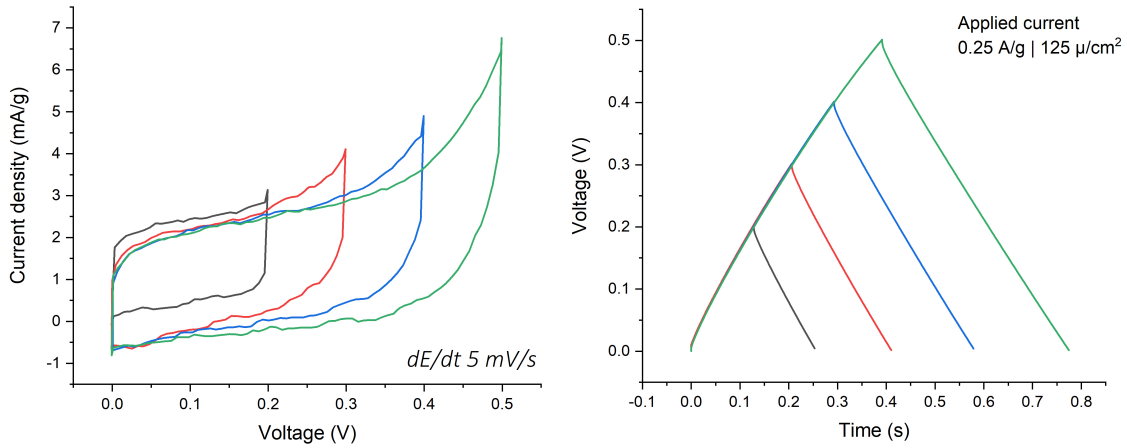


**Figure 4.30:** CC diagrams of Type S0F Cell 2 for  $V_{max}=0.2$  V at 250 mA/g and 2000 mA/g demonstrating the rise of the iR drop with an increase of applied current

The shape of the galvanostatic charge-discharge curve for the LIGF-Kapton Cell 2 was similar to the LIGP-Kapton cells with an increasing iR drop for the higher current densities. However the absolute value of the iR drop was about twice as large as in the LIGP-Kapton devices, moreover it could be also observed for the lower currents, see Figure 4.30.



(a) CV diagrams at  $\Delta V = 0.2 \div 0.5$  V for 5 mV/s scan rate

(b) CC diagrams for  $V_{max} = 0.2 \div 0.5$  V at various current densities

**Figure 4.31:** Type S0F, Cell 2. CV and GCPL data in the wider voltage range 0 - 0.5 V

Further series of CV experiments at larger voltage sweeps at fixed to 5mV/s scan rate could not show satisfactory behaviour of the Cell 2 as the rectangular shape quickly deteriorated with the rise of  $\Delta V$  as shown in Figure 4.31a. The GCPL curves in turn have shown very good performance, their triangular shape kept staying the same for all tested  $V_{max}$  of 0.2, 0.3, 0.4 and 0.5 V.

## Capacitance Evaluations for S0F Electrodes

Similarly to S0P Electrodes specific capacitance values were calculated for the data obtained by both CV and GCPL for S0F.

The trend of increasing capacitance with increasing maximum charge potential at constant current, was preserved for this S0F type of electrode and was similar to the type S0P (*i.e.* LIGP-Kapton):

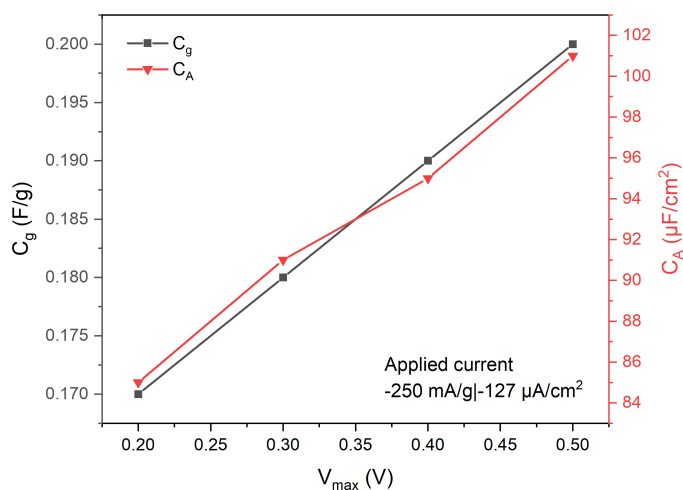


**Figure 4.32:** Type S0F Electrode - increasing trend in specific capacitance values evaluated from GCPL for increasing charge-discharge current densities at fixed  $V_{max} = 0.2$  V

However, in case of S0F the values of the capacitance did not show any significant decrease with increasing CV scanning rate. For the galvanostatic experiments with increasing charging-discharging current flowing through the cell for  $V_{max}$  set to 0.2 V a drop of  $\approx 27\%$  could be observed for the currents increasing from 100 to 2000 mA/g. Described trends can be seen in Figure 4.33

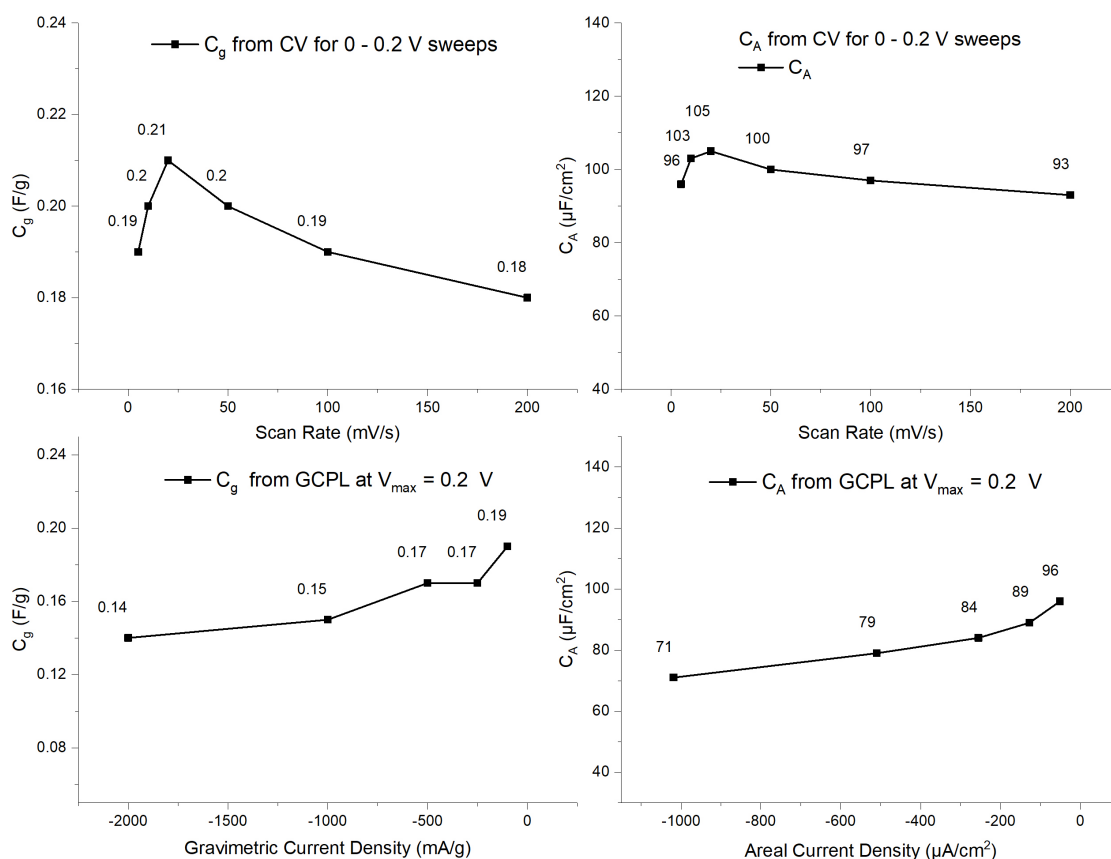


**Figure 4.33:** Type S0F Electrode - specific capacitance values evaluated from CV data at voltage window of 0 - 0.2 V for increasing scan rates  $dV/dt$  (top) and from GCPL data for increasing charge-discharge current densities at fixed  $V_{max} = 0.2$  V (bottom)

Observed effects could be ascribed to the pore size distribution. BET results have indeed shown that the LIGF can be seen as a mesoporous material whereas LIGP is microporous. As mentioned in the literature review, the pore size directly affects the storage capacity of an electrode; materials having micropores matching the ions size have better performance.

## S1F: LIGF-PDMS Composite Electrodes in a Swagelok Cell

The third type of electrode tested was LIGF-PDMS composite (S1F in the Table 3.8 above). Akin to previous setups two Swagelok cells with 1M NaNO<sub>3</sub> as an electrolyte were assembled. However, again the Cell 1 was discarded in the very beginning as it had shown indications of too high inner resistance, probably due to a failure of the VIA contacts, already during preliminary CV sweeps.

As for the Cell 2 the tests at lower potentials were performed in the identical manner as before by employing the same protocols for the CV (increasing scan rates at a fixed voltage window of 0 - 0.2 V) as well as for the GCPL measurements (increasing charge-discharge current at a fixed  $V_{max} = 0.2$  V). As one can see in Figure 4.34b, CV curves preserved the rectangular shape, however the galvanostatic curves at all currents were showing obvious distortions from the triangular shape, desirable for supercapacitors.

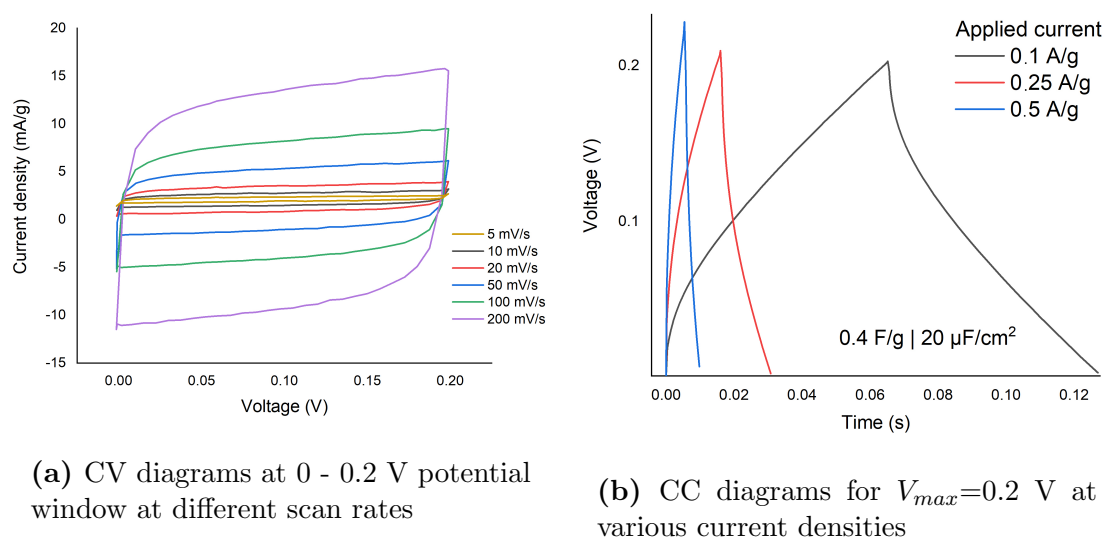
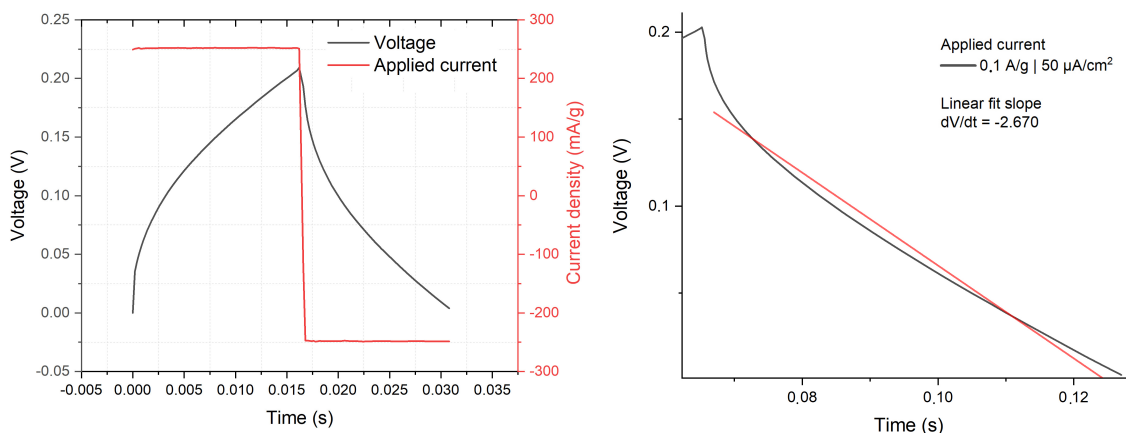


**Figure 4.34:** Type S1F Electrodes, Cell 2. CV and GCPL data in the low voltage range 0 - 0.2 V

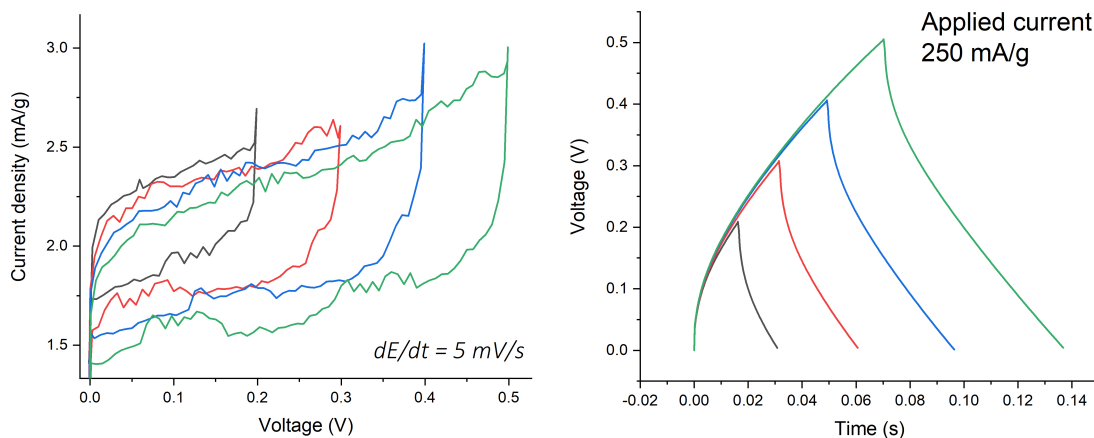
The distortions in GCPL curves could be a sign for Faradaic reactions taking place on the electrodes as well as of high inner resistance, which is undesirable for supercapacitor cells. On the other hand the value of  $iR$  had further increased, as compared to S0F electrodes. The discharging branch of the curves did not show the characteristic kink at the bottom of an  $iR$  drop, observed for the previous cases. This made more difficult and less accurate the estimation of a linear fit, as needed for capacitance assessment.



(a) Type S1F, Cell 2. Galvanostatic charge-discharge cycle up to  $V_{max} = 0.2$  V at 250 mA/g

(b) Towards determination of the slope of a discharge branch of a GCPL curve for capacitance evaluation

**Figure 4.35:** Type S1F Electrodes, Cell 2. Distorted CC curves



(a) CV diagrams at  $\Delta V = 0.2 \div 0.5$  V for 5 mV/s scan rate

(b) CC diagrams for  $V_{max} = 0.2 \div 0.5$  V at constant current densities

**Figure 4.36:** Type S1F Electrodes, Cell 2. CV and GCPL data in the voltage range 0 - 0.5 V

Further cyclic voltammetry attempts for larger voltage windows have delivered rather distorted CV curves which could not be used for capacitance evaluations. However, the CC  $V(t)$  graphs did not deteriorate more than they were and showed the same shape for all cycles measured at  $V_{max}$  from 0.2 to 0.5 V, see Figure 4.36.

## Capacitance Evaluations for S1F Electrodes

The data obtained in the experiments was collected to estimate the capacitance performance of the LIGF-PDMS composite, S1F. As can be seen in the Figure 4.37, the  $C_g$  and  $C_A$  of the S1F were about fivefold lower than the values for S0F, that is: same LIGF still supported on Kapton.

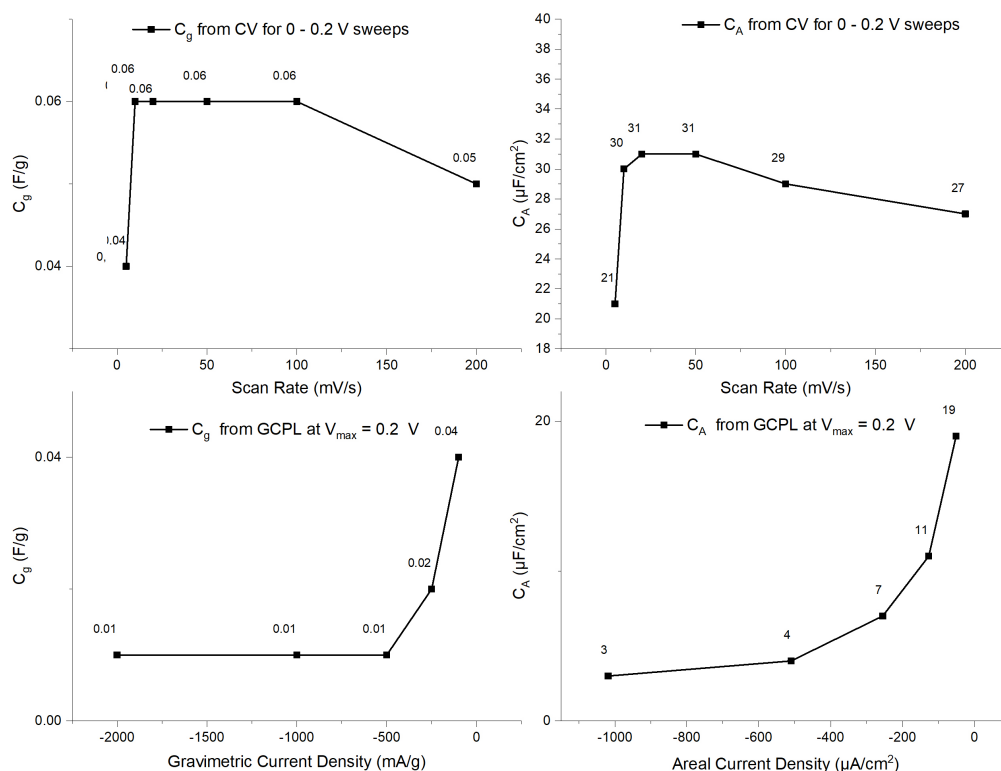


**Figure 4.37:** LIGF-PDMS Electrode - specific capacitance values evaluated from CV data at voltage window of 0 - 0.2 V for increasing scan rates  $dV/dt$  (top) and from GCPL data for increasing charge-discharge current densities at fixed  $V_{max} = 0.2$  V (bottom)

Although the calculations for  $C_g$  were made with the estimation that all the LIGF formed during lasering was translated into the composite, it is in fact obvious that a substantial part of it became unavailable for the electrode function after being embedded into the dielectric PDMS matrix, which in turn could aggravate the fact of the lower capacitance.

## S2P and S2F: LIGP-MPU and LIGF-MPU Composite Electrodes in a Swagelok Cell

As the fourth step in the electrochemical investigations of LIG-based SCs the thin LIG-MPU electrodes were tested for both types of graphene material: LIGP and LIGF, Type S2P and Type S2F, respectively, in the reference Table 3.8.

One Swagelok cell filled with 1M NaNO<sub>3</sub> electrolyte was assembled for each electrode variation. CV tests were performed at constant scan rate of 2 mV/s for four sweep windows of 0 - 0.1 V, 0.1 - 0.2 V, 0 - 0.3 V and 0 - 0.4 V. Galvanostatic charge-discharge cycles were performed at constant current density of 100 mA/g for four  $V_{max}$  values increasing with a step of 0.1 V from 0.1 to 0.4 V. CV diagrams obtained for both cell Types S2P and S2F are provided in Figure 4.38.

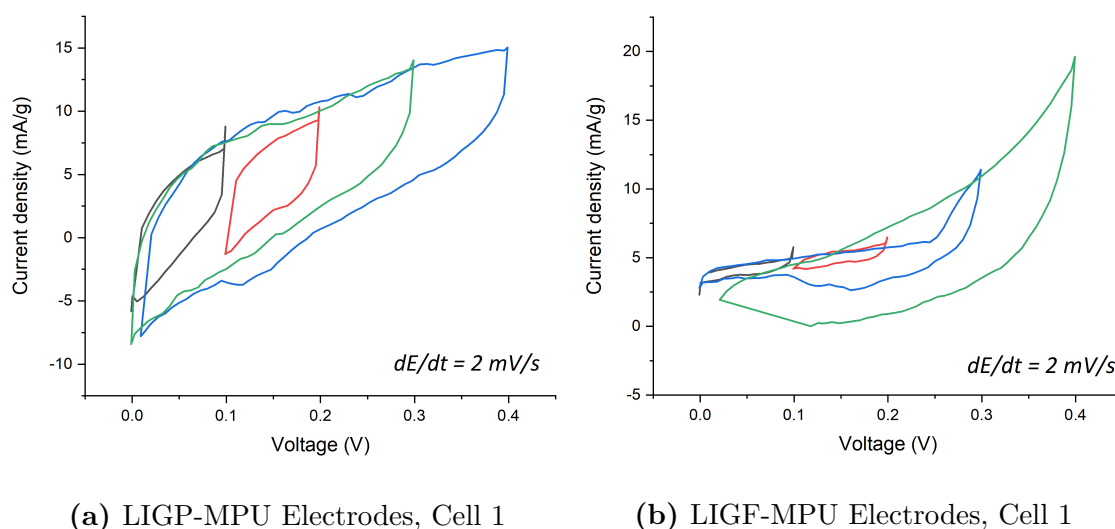


**Figure 4.38:** CV diagrams of S2P and S2F electrodes in Swagelok cells at various potential windows at a constant scan rate of 2 mV/s

As can be seen from the figures above, neither of the cells show ideal rectangular shape in their CV curves. However the LIGP-MPU electrodes show somewhat better performance than the LIGF-MPU device. The inner area of the curves is larger for the LIGP which is directly proportional to the stored charge  $Q [C]$ , meaning LIGP is capable to store more charge.

GCPL measurements have further confirmed a better, more stable, behaviour of the Type S2P LIGP-MPU electrodes. CC curves of these electrodes (Figure 4.39) had well defined triangular shape with a minor iR drop.

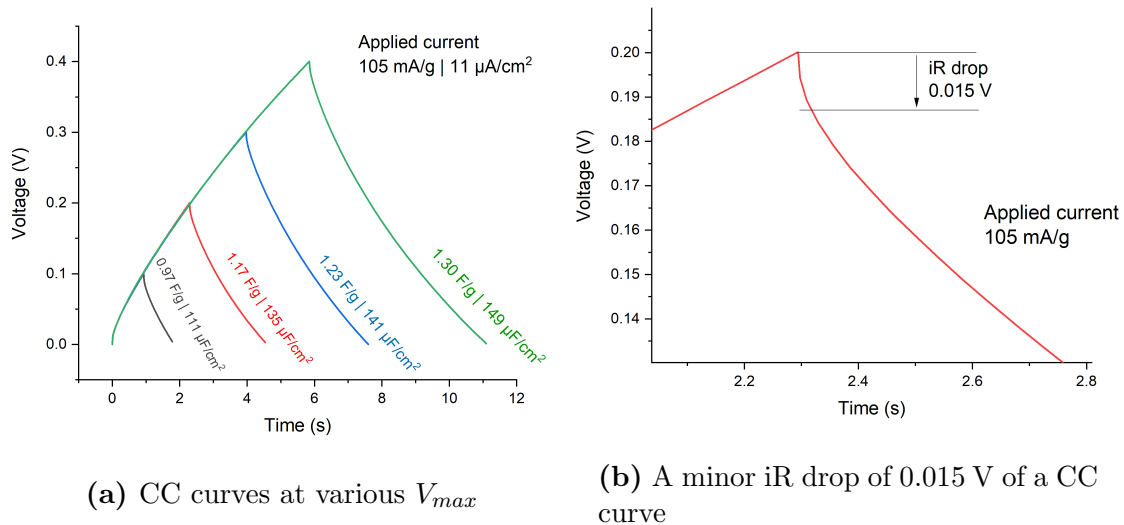


**Figure 4.39:** CC diagrams of S2P electrodes in a Swagelok cell

The LIGF-MPU electrodes have produced rather distorted charge-discharge  $V(t)$  curves so that only the runs with  $V_{max}$  of 0.1 V and 0.2 V had triangular appearance with relatively smaller iR drop than it was for the  $V_{max}$  of 0.3 V and 0.4 V:

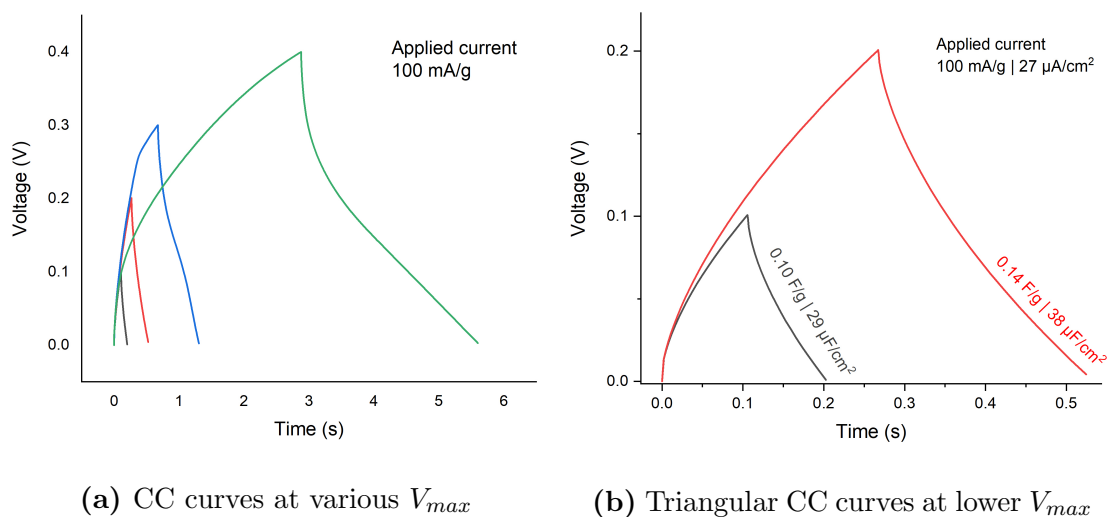
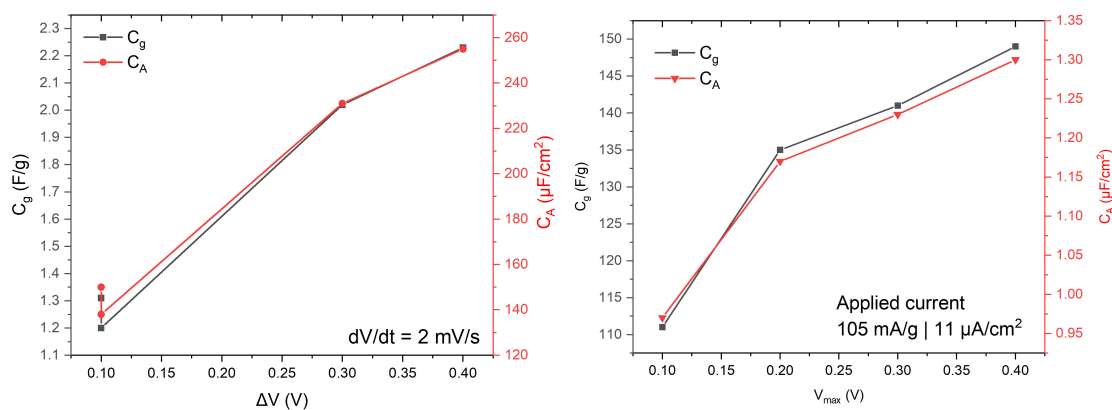


**Figure 4.40:** CC diagrams of S2F electrodes in a Swagelok cell

## Capacitance Evaluations for S2P and S2F Electrodes

Capacitance evaluations for S2P have shown relatively high capacitance values of around  $1.2 \div 2 \text{ F/g}$  which was comparable to the S0P. Also there was a good consistency in values calculated from both types of electrochemical experiments. The trend of increase in capacitance proportionally to broadening of the CV weep window (with scan rate staying constant), already observed in S0P, was found in S2P too. Similarly the capacitance values rose proportionally to  $V_{max}$  for the CC data obtained with a non changing charge-discharge current. Figures 4.41a and 4.41b provide comparison of the evaluated  $C_g$  and  $C_A$ .



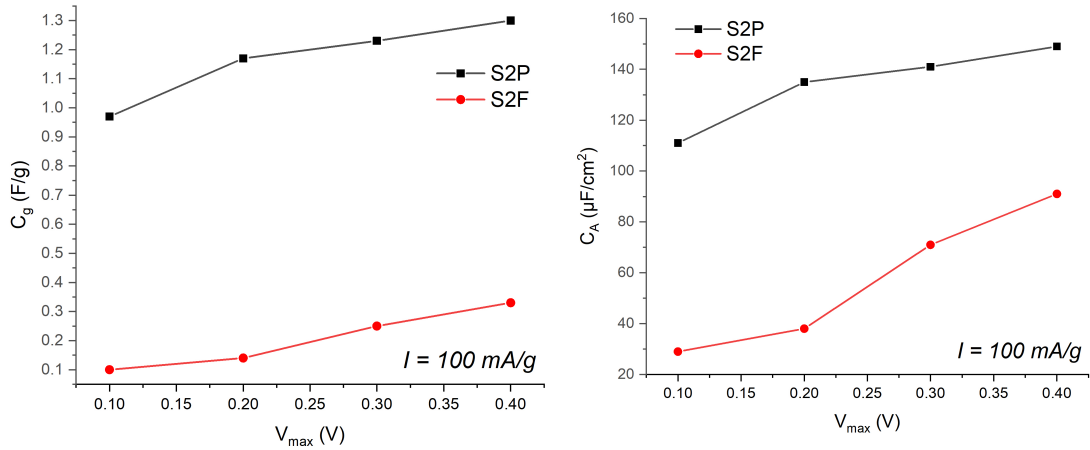
(a) Increase of specific capacitance with a  $\Delta V$  increase at constant scan rate of 2 mV/s

(b) Increase of specific capacitance with a rise of  $V_{max}$  at a constant current of 105 mA/s

**Figure 4.41:** Specific Capacitance of S2P electrode evaluated with CV and GCPL data

$C_g$  of S2F were about one order of magnitude lower than those for the S2P (see Figure 4.42a).

The difference between  $C_A$  of S2P and S2F is not dramatic; nonetheless S2P had a better supercapacitor performance. However, it is important to remark, that for  $C_A$  its evaluation does not take into account the actual mass of the active material. Rather the apparent surface area of the electrodes is considered, which is the same for S2F and S2P. Thus any comparison among the calculated  $C_A$  values should be considered with care.



(a) Comparison of  $C_g$  values for LIGP and LIGF on MPU electrodes

(b) Comparison of  $C_A$  values for S2P and S2F electrodes

**Figure 4.42:** Specific Capacitance of S2P and S2F electrodes evaluated with GCPL data

## Performance Comparison of LIG-based Electrodes in Swagelok Cells

Electrochemical characterization of the SCs was performed for varied voltage ranges, however for all of the cells there was a common region of 0-0.2 V where CV was performed at different scan rates. To be able to compare the results obtained for the lowest scan rates of 5 mV/s were chosen to be a benchmark. Identically for the GCPL the capacitance values obtained for  $V_{max}$  of 0.2 V at lowest charging-discharging current density of 0.1 A/g were picked to be compared. The data was condensed into Table 4.7. As a remark, we would like to mention that these numbers were taken as the reference when making the further decisions concerning the combination of LIG/Substrate, which would be the most suitable for flexible soft applications. However, for the in-depth overview of the capacitance values and how they were derived, the reader is suggested to go through the data presented in the previous pages.

**Table 4.7:** Summary for Capacitance Values for Swagelok LIG (NaNO<sub>3</sub>, 1M) Cells

Electrode Type	Composition	Cyclic Voltammetry		GCPL	
		$C_g$ [F/g]	$C_A$ [ $\mu$ F/cm <sup>2</sup> ]	$C_g$ [F/g]	$C_A$ [ $\mu$ F/cm <sup>2</sup> ]
S0P	LIGP-Kapton <sup>TM</sup>	1.87	381	1.08	220
S0F	LIGF-Kapton <sup>TM</sup>	0.19	96	0.19	96
S1F	LIGF-PDMS-8:1	0.04	21	0.04	19
S2P	LIGP-MPU	1.20	138	1.17	135
S2F	LIGF-MPU	0.19	51	0.14	38

The cross comparison of data obtained for different cells provided in Table 4.7 allowed to make a few generalizations about the performance of LIGs on various substrates.

Firstly, it was found that all cells based on LIGP (S0P, S2P) had significantly higher charge storage capability than LIGF-based electrodes (S0F, S1F, S2F). LIGP-cells have also shown better charge-discharge stability and less problems related to internal resistance. Secondly, it can be also seen that the S0F *i.e.* LIGF-PDMS composite have shown the worst performance among all, which could be addressed to an overall poor capacitance of LIGF aggravated by the fact it was to a big part embedded into the dielectric matrix of PDMS. Figure 4.43 provides the visual comparison chart underlining these two observations.

Further it is important to make a point concerning the two approaches which were used to evaluate the values of specific capacitance. The common way to assess the supercapacitor performance by comparing  $C_A$  values of the electrodes makes it difficult to estimate a real change in performance when talking about very light materials used as an active layer. Indeed, in our case the mass of LIGP on Kapton was 0.16 mg. whereas its mass on MPU was only 0.09 mg. This inevitably introduces a difference by the factor of 0.16/0.09 into  $C_g$ , all other parameters being equal. On the contrary, the specific areal capacitance would not change in these circumstances. Graph in Figure 4.44 demonstrates discrepancy in  $C_g$  *vs.*  $C_A$  trends. Indeed all electrodes in Swagelok cells had the same surface area  $s$  of  $0.5\pi$  cm<sup>2</sup>, however the mass of the capacitive LIG material was different for PI, PDMS and MPU, therefore the areal mass loading [ $mg/cm^2$ ] also varied.

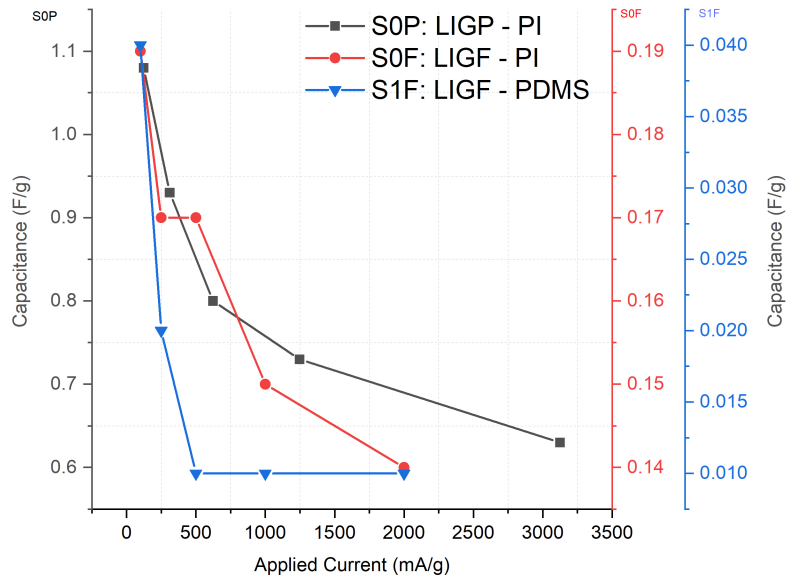


**Figure 4.43:** Comparison of  $C_g$  values of LIGF and LIGP based cells

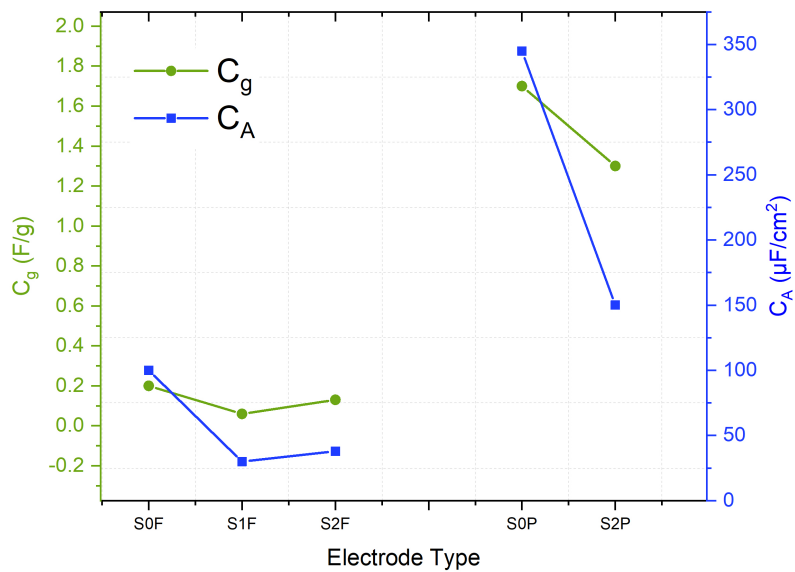


**Figure 4.44:** Comparison of  $C_g$  and  $C_A$  trends (obtained from CV data) for cells with varying mass  $m$  of an active material when electrode surface area  $s$  stays constant

When comparing S2P (LIGP-MPU) and S0P (LIGP-PI) cells from Figure 4.44 one can see the 230% change in specific areal capacitance, whereas the specific gravimetric capacitance changes only by 130%.

One more point which needs to be brought to discussion is the consistency between the CV and GCPL data. In Figure 4.45 it can be seen that, except from the values obtained for S2P cells, the values and trends estimated with the two techniques lay in a qualitative agreement.

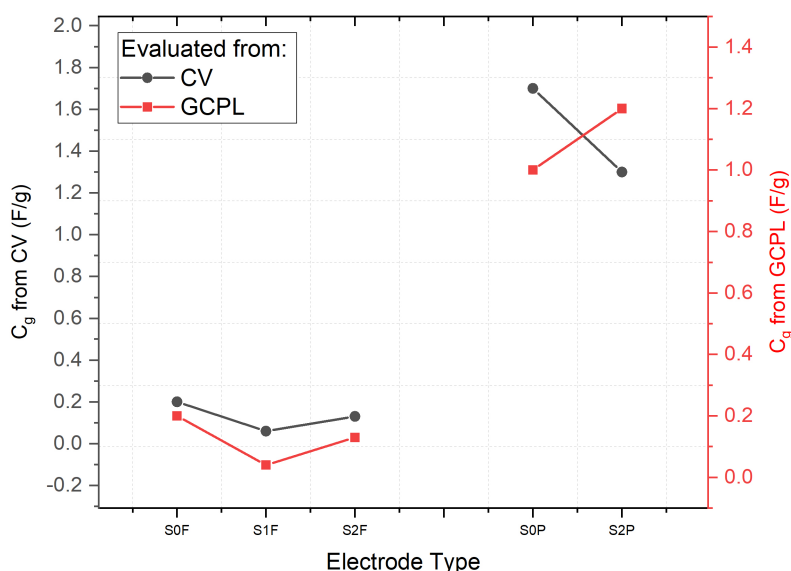


**Figure 4.45:** Comparison of  $C_g$  values and trends obtained from CV and from GCPL data

## 4.5 Electrochemical Characterization of Flat and Rolled SCs

In the same manner as the Swagelok cells all flat and rolled cells were subject to electrochemical analysis via CV and GCPL methods. Unfortunately the flat cells as well as the rolled cells based on PDMS and MPU LIG composites did not show satisfying storage behaviour. Therefore all the attempted characterizations failed. This fact could be attributed to the high internal sheet resistance for the devices since the electrodes were not pressed to each other to reduce the internal gap between the electrodes. For the PDMS-based LIG electrodes morphological investigations showed that the pore volume accessible for ions is drastically reduced by the polymeric matrix of PDMS. In the case of MPU substrates a plausible explanation is that the surface density of LIG material transferred from the PI is not sufficient enough to form satisfactory working Helmholtz layers. These possible reasons for failure should be investigated further. Moreover, novel strategies should be taken into consideration for LIG embedding into soft/stretchable matrices before to attempt new characterization of Flat and Rolled SCs.

## 4.6 Discussion on Biocompatibility

Apart from improving electrochemical performance of supercapacitors, additional requirements are put on the materials, which are meant for wearable applications. First of all these materials should be biocompatible. Therefore we bring a short discussion on that topic in this section.

According to the technical data available [56], [51], [34], Kapton sheets used as the LIG source in this thesis, together with PDMS and MPU, belong to the group of biocompatible materials. Sodium nitrate is a known food additive approved for use in the EU [57].

Another important point to be addressed regards the graphene materials. According to S. Syama *et. al* [58], research on toxicity of graphene materials is still in the developing stage, which makes it difficult to assess the potential health hazards which might be associated with its use on skin. Specifically for the LIGs further investigations are needed. Is it important however to remark that in the proposed use the LIG material will not stand in direct contact with Epidermis. Rather the LIG electrode as well as the electrolyte will be encapsulated in a biocompatible polymer matrix. Assessing the barrier properties of this encapsulating layer is therefore important.



## 5. Summary

Summarizing Results and Discussion section following final conclusions can be drawn.

Recently developed process [26] of obtaining laser induced graphene by scribing electrically conductive circuits directly on a polyimide films was utilized to obtain two types of LIG: LIGP and LIGF. A part of the obtained patterns was further successfully transferred from PI onto two model polymeric carriers, PDMS and MPU, which allowed obtaining stretchable LIG based electrodes for SCs.

SEM and LM investigations demonstrated that LIGP has porous flake-like microstructure while LIGF consists of a porous layer at the bottom which evolves into fibrous bundled cones on the top surface. These cone bundles of fibers have an average diameter of 50-70 nm and a length of 100-200  $\mu m$ . It was further shown that LIGs retain their original morphology also after transferring onto PDMS and MPU substrates. The LIG electrodes based on PDMS and MPU were subjected to electro-mechanical tests. Within the tested range of strains up to 30% LIG-PDMS electrodes show linear behaviour of stress to strain and resistance to strain lines, whereas the MPU-based electrodes show viscoelastic behaviour with a hysteresis in the R to Strain line.

Electromechanical properties of the samples was tested at varying humidity rates between 45% and 92%. It was found that LIGP-PDMS demonstrates a noticeable response to an increase in RH: when increasing RH from 45% to 92% the drop of Young's modulus in samples LIGP-PDMS from 2.5-4 MPa to 1.2-2 MPa is observed. LIGF-PDMS samples did not show any noticeable change in Young modulus upon varying RH. The effect was attributed to the earlier found hydrophobicity of LIGP. Young's modulus of LIGP-MPU and LIGF-MPU samples was found to be the same -  $\approx 8.3$  MPa at the RH of 45% and  $\approx 5.8$  MPa at the RH of 92%.

Surface area and porosity of the LIGP and LIGF materials were characterized via the volumetric gas adsorption measurements performed with classical powder BET analysis of LIG powders as well as via the Gemini<sup>TM</sup> volumetric method performed on polymeric stripes (PI, PDMS) covered with LIG.  $A_{BET}$  of LIGP powder was estimated to be 192  $m^2/g$ ,  $A_{BET}$  of LIGF powder - 270  $m^2/g$ . These values were consistent with known reports [1].

Gemini tests have shown, the specific surface area of LIG flat electrodes available to adsorption is lower than this of LIG powders.  $A_{Gemini}$  of LIGP-PI electrodes was estimated to be about 120  $m^2/g$ ;  $A_{Gemini}$  of LIGF-PI electrodes was estimated to be about 55  $m^2/g$ . Latter result for PI-LIGF samples was inconclusive due to the loss of some LIGF material in the Gemini chamber during degassing procedure. Gemini analysis of LIGP-PDMS and LIGF-PDMS have shown that the specific surface area of these composites was about 15-30  $m^2/g$ . The lower values for these samples were attributed to the fact that part of the LIG, which gets embedded into PDMS during transfer, becomes unavailable for adsorption processes.

Three modifications of supercapacitor devices (Swagelok<sup>TM</sup>, Flat and Rolles geometries with 1M  $NaNO_3$  as electrolyte) were designed, fabricated and tested via CV and GCPL.

The results for Swagelok<sup>TM</sup> cells assembled with electrodes based on three different LIG substrates, namely PI, PU and PDMS were as follows.  $C_g$  of cells based on LIGP - S0P and S2P reached the values of 1.87 and 1.20  $F/g$  respectively, which were significantly higher than those for LIGF-based electrodes (S0F - 96  $F/g$  , S2F - 51  $F/g$ ). LIGP-cells have also shown better charge-discharge stability and less problems related to internal resistance. S2F based on MPU have shown interestingly promising performance, however for some cells the inner sheet resistance was too high which negatively affected the capacitive properties of respective devices. S1F cells did not show satisfying capacitive behaviour, which was addressed to an overall poor capacitance of LIGF aggravated by the fact it was to a big part embedded into the dielectric matrix of PDMS.

Capacitive behaviour of flat cells as well as the rolled cells based on PDMS and PU LIG composites was not satisfying. The main reason for it could be too high resistance of the devices because the electrodes were not pressed to each other and therefore the gap between the electrodes was probably too large to allow proper Helmholtz layer to be formed. Further improvements of the flat cells design are therefore needed.

# Bibliography

- [1] Jian Lin, Zhiwei Peng, Yuanyue Liu, Francisco Ruiz-Zepeda, Ruquan Ye, Errol L. G. Samuel, Miguel Jose Yacaman, Boris I. Yakobson, and James M. Tour. Laser-induced porous graphene films from commercial polymers. *Nature Communications*, 5(1):5714, December 2014. iii, vii, vii, vii, 3, 4, 5, 6, 7, 67, 95
- [2] Graphene. Accessed at <https://de.wikipedia.org/wiki/Polyurethane/media/Datei:Polyurethane-allg.svg>, on 2020-07-08. vii, 5, 6
- [3] PDMS chemical formula. Available at <https://www.sigmaaldrich.com/>, on 2020-06-11. vii, 7
- [4] G Camino, S. M Lomakin, and M Lazzari. Polydimethylsiloxane thermal degradation Part 1. Kinetic aspects. *Polymer*, 42(6):2395–2402, March 2001. vii, 8
- [5] S.J Metz. WATER VAPOR AND GAS TRANSPORT THROUGH POLY-MERIC MEMBRANES, PhD Thesis. *Enschede, The Netherlands*, 2003. vii, 8, 9
- [6] Zhixin Wang, Alex A. Volinsky, and Nathan D. Gallant. Crosslinking effect on polydimethylsiloxane elastic modulus measured by custom-built compression instrument. *Journal of Applied Polymer Science*, 131(22):n/a–n/a, November 2014. vii, 8, 9, 10
- [7] Polyurethane structure. Accessed at <https://oer.physics.manchester.ac.uk/AQM2/Notes/Notes-6.4.html>, on 2020-07-08. vii, 11
- [8] Vasanth Kumar, Gadipelli Srinivas, Barbara Wood, Kiran Ramisetty, Andrew Stewart, Christopher Howard, D.J.L. Brett, and Francisco Rodriguez-Reinoso. Characterization of adsorption site energies and heterogeneous surfaces of porous materials. *Journal of Materials Chemistry A*, 7, 02 2019. vii, 12, 13
- [9] Francesca Borghi, Matteo Milani, Luca Giacomo Bettini, Alessandro Podestà, and Paolo Milani. Quantitative characterization of the interfacial morphology and bulk porosity of nanoporous cluster-assembled carbon thin films. *Applied Surface Science*, 479:395–402, June 2019. viii, 14, 15, 40
- [10] Stress–strain curve. Accessed at [https://en.wikipedia.org/wiki/Stress-strain\\_curve](https://en.wikipedia.org/wiki/Stress-strain_curve), on 2020-08-21. viii, 16
- [11] Sheet resistance measurements of thin films. Accessed at <https://www.ossila.com/pages/sheet-resistance-measurements-thin-films>, on 2020-08-21. viii, 18
- [12] Chiara Ballin. Laser induced graphene as electrode for wearable electronic devices. *Politecnico di Torino*, 2018. viii, 19

- [13] Chuizhou Meng, Oren Gall, and Pedro Irazoqui. A flexible super-capacitive solid-state power supply for miniature implantable medical devices. *Biomedical microdevices*, 15:973–983, 07 2013. viii, 20
- [14] Cheng Zhong, Yida Deng, Wenbin Hu, Jinli Qiao, Lei Zhang, and JiuJun Zhang. A review of electrolyte materials and compositions for electrochemical supercapacitors. *Chem. Soc. Rev.*, 44:7484–7539, 2015. viii, 21
- [15] Sung-Yeob Jeong, Yong-Won Ma, Jun-Uk Lee, Gyeong-Ju Je, and Bo-sung Shin. Flexible and Highly Sensitive Strain Sensor Based on Laser-Induced Graphene Pattern Fabricated by 355 nm Pulsed Laser. *Sensors*, 19(22):4867, November 2019. viii, viii, 22, 23
- [16] Andrea Lamberti, Francesca Clerici, Marco Fontana, and Luciano Scaltrito. A Highly Stretchable Supercapacitor Using Laser-Induced Graphene Electrodes onto Elastomeric Substrate. *Advanced Energy Materials*, 6(10):1600050, 2016. \_eprint: <https://onlinelibrary.wiley.com/doi/pdf/10.1002/aenm.201600050>. viii, 22, 23, 24
- [17] Matteo Parmeggiani, Pietro Zaccagnini, Stefano Stassi, Marco Fontana, Stefano Bianco, Carmelo Nicosia, Candido F. Pirri, and Andrea Lamberti. PDMS/Polyimide Composite as an Elastomeric Substrate for Multifunctional Laser-Induced Graphene Electrodes. *ACS Applied Materials & Interfaces*, 11(36):33221–33230, September 2019. Publisher: American Chemical Society. viii, viii, 22, 23, 24, 25
- [18] H. Hampel. LIG, Master Thesis. *TU Graz*, 2020. ix, 28, 53, 54
- [19] A. Dallinger. Custom Stretcher Setup, Master Thesis. *TU Graz*, 2018. ix, 34
- [20] Gemini VII Series Surface Area Analyzer Brochure. *Micromeritics Instrument Corporation*, 2016. ix, 39
- [21] Alexander Dallinger, Kirill Keller, Harald Fitzek, and Francesco Greco. Stretchable and Skin-Conformable Conductors Based on Polyurethane/Laser-Induced Graphene. *ACS Applied Materials & Interfaces*, page acsami.0c03148, April 2020. x, 22, 25, 43, 55, 56
- [22] D. Grafinger. LIG, Bachelor Thesis. *TU Graz*, 2020. xiii, 6, 59
- [23] Sanliang Zhang and Ning Pan. Supercapacitors performance evaluation. *Advanced Energy Materials*, 5(6):1401401, 2015. 1
- [24] R. Srinivasan, R. R. Hall, W. D. Wilson, W. D. Loehle, and D. C. Allbee. Formation of a porous, patternable, electrically conducting carbon network by the ultraviolet laser irradiation of the polyimide pmda-oda (kapton). *Chemistry of Materials*, 6(7):888–889, 1994. 3
- [25] Mikhail I. Katsnelson. *Graphene: Carbon in Two Dimensions*. Cambridge University Press, 2012. 5

- [26] Luong Xuan Duy, Zhiwei Peng, Yilun Li, Jibo Zhang, Yongsung Ji, and James M. Tour. Laser-induced graphene fibers. *Carbon*, 126:472 – 479, 2018. 6, 95
- [27] R. Gross and A. Marx. *Festkörperphysik*. 2012. 6
- [28] Bernardo Marinho, Marcos Ghislandi, Evgeniy Tkalya, Cor E. Koning, and Gijbertus de With. Electrical conductivity of compacts of graphene, multi-wall carbon nanotubes, carbon black, and graphite powder. *Powder Technology*, 221:351–358, May 2012. 6
- [29] Ruquan Ye, Dustin K. James, and James M. Tour. Laser-induced graphene: From discovery to translation. *Advanced Materials*, 31(1):1803621, 2019. 6
- [30] Michel Vert, Yoshiharu Doi, Karl-Heinz Hellwich, Michael Hess, Philip Hodge, Przemyslaw Kubisa, Marguerite Rinaudo, and François Schué. Terminology for biorelated polymers and applications (iupac recommendations 2012). *Pure and Applied Chemistry*, 84(2):377 – 410, 2012. 7
- [31] Pierre-Jean Wipff, Hicham Majd, Chitragada Acharya, Lara Buscemi, Jean-Jacques Meister, and Boris Hinz. The covalent attachment of adhesion molecules to silicone membranes for cell stretching applications. *Biomaterials*, 30(9):1781–1789, March 2009. 7
- [32] Mohamad Riduwan Ramli, Muhammad Bisyrul Hafi Othman, Azlan Arifin, and Zulkifli Ahmad. Cross-link network of polydimethylsiloxane via addition and condensation (RTV) mechanisms. Part I: Synthesis and thermal properties. *Polymer Degradation and Stability*, 96(12):2064–2070, December 2011. 8
- [33] L. A. S. A. Prado, Maurício L. Sforça, Adriana G. de Oliveira, and Inez V. P. Yoshida. Poly(dimethylsiloxane) networks modified with poly(phenylsilsesquioxane)s: Synthesis, structural characterisation and evaluation of the thermal stability and gas permeability. *European Polymer Journal*, 44(10):3080–3086, October 2008. 8, 9
- [34] Alvaro Mata, Aaron J. Fleischman, and Shuvo Roy. Characterization of Polydimethylsiloxane (PDMS) Properties for Biomedical Micro/Nanosystems. *Biomedical Microdevices*, 7(4):281–293, December 2005. 10, 93
- [35] Vinny R. Sastri. 7 - engineering thermoplastics: Acrylics, polycarbonates, polyurethanes, polyacetals, polyesters, and polyamides. In *Plastics in Medical Devices (Second Edition)*, pages 121 – 172. William Andrew Publishing, Oxford, second edition edition, 2014. 10
- [36] Nupur Kohli, Vaibhav Sharma, Stuart J. Brown, and Elena García-Gareta. 5 - synthetic polymers for skin biomaterials. In *Biomaterials for Skin Repair and Regeneration*, pages 125 – 149. Woodhead Publishing, 2019. 10

- [37] Fixomull films technical sheet. Accessed at <https://www.bsnmedical.com/products/wound-care-vascular/category-product-search/acute-wound-care/fixation/fixomullr-transparent.html>, on 2020-07-11. 11
- [38] Pure and Applied Chemistry Volume 46 Issue 1 (1976), January 1976. Section: Pure and Applied Chemistry. 11
- [39] Kenneth S.W. Sing. Characterization of porous solids: An introductory survey. In *Characterization of Porous Solids II*, volume 62 of *Studies in Surface Science and Catalysis*, pages 1 – 9. Elsevier, 1991. 11
- [40] Stephen Brunauer, Jan Skalny, and E.E Bodor. Adsorption on nonporous solids. *Journal of Colloid and Interface Science*, 30(4):546 – 552, 1969. 13
- [41] Françoise Rouquerol, Jean Rouquerol, and Kenneth Sing. Chapter 6 - assessment of surface area. In *Adsorption by Powders and Porous Solids*, pages 165 – 189. Academic Press, London, 1999. 13, 14
- [42] Françoise Rouquerol, Jean Rouquerol, and Kenneth Sing. Chapter 9 - adsorption by active carbons. In *Adsorption by Powders and Porous Solids*, pages 237 – 285. Academic Press, London, 1999. 14
- [43] Françoise Rouquerol, Jean Rouquerol, and Kenneth Sing. Chapter 7 - assessment of mesoporosity. In *Adsorption by Powders and Porous Solids*, pages 191 – 217. Academic Press, London, 1999. 14
- [44] Shinn-Tyan Wu. A Rigorous Justification of the Point B Method for Determination of mono-layer Capacity from a Type II Adsorption Isotherm. page 20. 14
- [45] M.A. Meyers and K.K. Chawla. *Mechanical Behavior of Materials*. Cambridge University Press, 2008. 17
- [46] Serdar Yilmaz. The geometric resistivity correction factor for several geometrical samples. *Journal of Semiconductors*, 36:082001–1, 03 2015. 18
- [47] Haldor Topsoe. Geometric factors in four point resistivity measurement. *Bulletin*, 472-13, 05 1968. 18
- [48] C. F. Pirri G. C. Stefano Stassi, Valentina Cauda. Flexible tactile sensing based on piezoresistive composites: A review. *Sensors*, 2014. 18
- [49] A. Yu, V. Chabot, and J. Zhang. *Electrochemical Supercapacitors for Energy Storage and Delivery: Fundamentals and Applications*. Electrochemical Energy Storage and Conversion. Taylor & Francis, 2013. 20
- [50] Luong Xuan Duy, Zhiwei Peng, Yilun Li, Jibo Zhang, Yongsung Ji, and James M. Tour. Laser-induced graphene fibers. *Carbon*, 126:472 – 479, 2018. 27

- [51] Fixomull medical films technical data. Accessed at <https://www.bsnmedical.com/products/wound-care-vascular/category-product-search/acute-wound-care/fixation/fixomullr-transparent.html>, on 2020-07-31. 31, 62, 93
- [52] Zhiwei Peng, Jian Lin, Ruquan Ye, Errol L. G. Samuel, and James M. Tour. Flexible and Stackable Laser-Induced Graphene Supercapacitors. *ACS Applied Materials & Interfaces*, 7(5):3414–3419, February 2015. Publisher: American Chemical Society. 50
- [53] M. Gritzner. Wettability of LIG, Bachelor Thesis. *TU Graz*, 2020. 59
- [54] Matthias Thommes, Katsumi Kaneko, Alexander V. Neimark, James P. Olivier, Francisco Rodriguez-Reinoso, Jean Rouquerol, and Kenneth S.W. Sing. Physisorption of gases, with special reference to the evaluation of surface area and pore size distribution (IUPAC Technical Report). *Pure and Applied Chemistry*, 87(9-10):1051–1069, October 2015. 65
- [55] NLDFIT - DFT Models. Available at <https://www.micromeritics.com/library/DFT-NLDFIT-Density-Functional-Theory/NLDFIT-DFT-Models.aspx>, on 2020-04-21. 65
- [56] D. P. Pivin Jr. J. C. Williams R. J. Vetter P. J. Rousche, D. S. Pellinen and D. R. Kirke. Flexible polyimide-based intracortical electrode arrays with bioactive capability. *IEEE Trans. Biomed. Eng.*, 48:361, 03 2001. 93
- [57] Approved additives and e numbers. Available at <https://www.food.gov.uk/business-guidance/approved-additives-and-e-numbers>, on 2020-04-21. 93
- [58] S. Syama and P. V. Mohanan. Safety and biocompatibility of graphene: A new generation nanomaterial for biomedical application. *International Journal of Biological Macromolecules*, 86:546–555, May 2016. 93